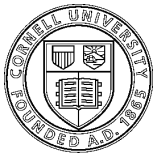

IgE-FcεRI-MEDIATED REDISTRIBUTION OF SIGNALING PROTEINS MEASURED WITH NANOMETER RESOLUTION USING SCANNING ELECTRON MICROSCOPY

by Ethan N. Chiang

This thesis/dissertation document has been electronically approved by the following individuals:

Baird,Barbara Ann (Chairperson)

Ober,Christopher Kemper (Co-Chair)

Frederick R. Maxfield (Minor Member)

IgE-FcεRI-MEDIATED REDISTRIBUTION OF SIGNALING PROTEINS MEASURED WITH NANOMETER RESOLUTION USING SCANNING ELECTRON MICROSCOPY

A Dissertation

Presented to the Faculty of the Graduate School

of Cornell University

In Partial Fulfillment of the Requirements for the Degree of

Doctor of Philosophy

by

Ethan N. Chiang

August 2010

IgE-FcεRI-MEDIATED REDISTRIBUTION OF SIGNALING PROTEINS MEASURED WITH NANOMETER RESOLUTION USING SCANNING ELECTRON MICROSCOPY

Ethan N. Chiang, Ph.D.

Cornell University 2010

In this work, we use fluorescence and electron microscopy techniques to probe the microscopic and nanoscopic functional heterogeneity of the plasma membrane in RBL-2H3 cells. Using patterned poly (acrylic acid) (PAA) polymer brush surfaces, we explored the effects of surface chemistry and topography on cell-surface interactions. While PAA is reportedly cell-repellent, we find that micro-patterned PAA arrays promote cell adhesion and initiate robust cellular responses, including protein reorganization and cytoskeletal remodeling. We then demonstrate that these properties can be 'tuned' by increasing the size of brush regions (surface becomes more cell-repellent) or reducing brush thickness (prevents cytoskeletal remodeling). By modifying the arrayed PAA brushes with ligands that bind specifically to IgE-bound FcεRI, we were able to stimulate cells with micron-scale spatial resolution and monitor specific protein localization at the stimulated cell-surface interface.

We also use pair correlation function analysis and high resolution scanning electron microscopy (SEM) to investigate nano-scale plasma membrane heterogeneity of immuno-gold labeled proteins in intact, resting

cells. Consistent with previous reports, we find that gold particles labeling cell surface proteins, as well as proteins randomly immobilized onto silicon surfaces, have clustered distributions. In contrast to previous reports, we demonstrate that this apparent clustering can be accounted for by multiple gold particles binding to individual target proteins. We provide further evidence of this artifact by measuring cross-correlations between two functionally identical, but distinguishable pools, of IgE-FcεRI or GM_1. After correcting this artifact, we find that each of the six membrane proteins examined are distributed randomly at scales > ~15-20 nm but that IgE-FcεRI and Lyn show a slight tendency to co-associate.

However, in cells stimulated with multivalent antigen, we find that IgE-FcεRI, Lyn, Syk, and LAT undergo rapid and dramatic reorganization (after accounting for clustering artifacts) and redistribute into large, stable clusters that may represent signaling platforms. At longer stimulation times, these clusters reduce in size as protein densities within clusters increases. In contrast to previous studies, our double label experiments show that Lyn rapidly associates with crosslinked IgE-FcεRI and remains co-clustered at long stimulation times. Additionally, we demonstrate that the stimulation dependent clustering of IgE-FcεRI and Lyn is sensitive to both cholesterol depletion and to Src family kinase activity, indicating that both lipid raft-mediated and protein-protein interactions contribute to early signaling events.

BIOGRAPHICAL SKETCH

Ethan Nicholas Chiang was born on March 18, 1982 in Honolulu, Hawaii to parents, Peter and Karen Chiang. As a child, he spent much of his time playing volleyball, swimming at the beach, reading, drawing, singing and wondering what the mainland was like. After winning a long, hard fought battle for Class President in the 6th grade, Ethan developed a penchant for shaking hands, passing out lollipops, and making ambiguous campaign promises, which ultimately culminated in his election as high school Student Body President.

After graduating as class valedictorian, Ethan attended Whitman College in Walla Walla, WA (Go Fighting Missionaries!) as a Paul Garrett Scholar. In addition to playing the viola with the Whitman College orchestra and Walla Walla Symphony, he was a founding member of Whitman's first co-ed a cappella group, Schwa. After switching majors five times (Biochemistry, Biophysics, and Molecular Biology to Music to French to Economics), he aptly picked Chemistry due to a completely unexpected fascination with Quantum Mechanics. His early interest in research resulted from undergraduate research in the polymer chemistry laboratory of Professor Allison Calhoun, where he studied the surface energetics of chemically modified mineral particles.

Ethan began his graduate studies in 2004 at Cornell University in the Department of Chemistry and Chemical Biology with Professor Barbara Baird and David Holowka and in the Department of Materials Science and

Engineering with Professor Christopher Ober. Throughout graduate school, he also participated in the Cornell University-Weill Medical College-Rockefeller University-Memorial Sloan Kettering Cancer Institute Tri-Institutional Training Program in Chemical Biology. As a result, much of his research interests were highly collaborative and focused at the interface of materials science, chemistry, and biology. In 2005, he worked on a collaborative research project as a visiting graduate student in Professor Fred Maxfield's laboratory in the Department of Biochemistry at Weill Medical College in New York City.

After completing his dissertation defense, Ethan received a Christine Mirzayan Science and Technology Policy Fellowship at The National Academies in Washington, D.C., where he worked with the Committee on Scientific Communication and National Security. He is currently a Program Officer with the Board on Global Science and Technology in the Policy and Global Affairs Division of The National Academy of Sciences.

….to Mom & Dad

ACKNOWLEDGEMENTS

This work would not have been possible without the support of many people. I am extremely grateful to my research advisor Professor Barbara Baird, who allowed me the flexibility and freedom, as well as encouragement, to pursue interesting, challenging, and exciting projects. I am also indebted to Dr. David Holowka for his invaluable advice and kind willingness to share all of his general science know-how. I am also thankful for the enthusiasm, optimism, and insight of my co-advisor Professor Christopher Ober. I would also like to thank my committee member, Professor Frederick Maxfield, who not only provided valuable feedback throughout the years, but also welcomed me into his laboratory as a research collaborator.

I am sincerely grateful to the many friends who have made my time here so memorable. To Jason, Sean, Drew, Ryan, Mike, Sung-Soo, Amelia, Mandy, Brad, Claire, Showey, Brittany, Steve, Andy, Katie, Krystal, Jerrel, Chris, Chad, Jenn, Jamie, Jeff, Eric, Annie and Adina for the poker nights, trips to The Woods, dinner parties, dancing, Quantum Mechanics homework parties, sleepovers, wine tours, movie nights, Cornell Iron Chef competitions, bowling nights, dodgeball tournaments, karaoke, road trips, late night talks, hockey games, *clears throat* miscellaneous nights out, and other general mayhem that occurred under their watch. To Sarah and Erin for becoming the big sisters I never had. To my TPCB-ers: Disan, Nick, Sourabh, Paul, Amy, Nen, Inish, Julia, Poulami, and Vidhya for making Chemical Biology Retreats feel like vacation. To Norah, Stephanie, and Jinmin for their encouragement, smiles and keeping me well-fed. To Alexis for putting up with my

non-stop singing, political rants, constant chattering, and other distractions. To my faithful collaborators, Rong and Andrew, for helping me realize that 'wrong' results only exist if you don't know the right question to ask. To Ober Group lab mates, especially JK, Katie, Jing, Marvin, Priscilla, Michelle, and Evan. To Baird-Holowka lab mates past and present, especially Prabs, Wageesha, Lavannya, Alice, Nat, Roy, Deepti, Kirsten, Kari, and Amit. To everyone – Thank You.

While my graduate studies culminate with this dissertation, the long road to all of my successes has been paved by the support and love of my family. Thanks to my brother Jordan for never letting me get away with anything – I'm much cleverer because of you. Thanks to my parents, who always helped me accomplish my dreams, no matter how transient, near-, or far-sighted they appeared. For driving me to swimming lessons, Boy Scout meetings, and orchestra rehearsals – for making library trips an adventure and helping with science fair projects – for Halloween costumes and trips to the beach – for teaching me the values of hard work, patience, and appreciation – for being Mom and Dad – Thank You.

Lastly, I would also like to acknowledge research support from Cornell's Nanobiotechnology Center (NSF ECS9876771), NIH Grant R01-A108306, NIH T32-GM08210, and Cornell's Tri-Institutional Training Program in Chemical Biology.

TABLE OF CONTENTS

LIST OF FIGURES

LIST OF TABLES

LIST OF ABBREVIATIONS

Ag:	antigen
APC:	antigen presenting cell
A488:	Alexa Fluor 488
A555:	Alexa Fluor 555
BSS:	buffered-saline solution
BCR:	B cell receptor
BLNK:	B cell linker protein
BSD:	backscattered electron detection
COOH:	carboxylic acid
C(r):	cross-correlation function
ξ:	correlation length
ξ_c:	cross-correlation length
CTxB:	cholera toxin subunit B
CytoD:	cytochalasin D
DAG:	diacyl glycerol
ρ_{cl}:	average protein density within clusters
ρ_{avg}:	average surface density or target proteins
ρ_{gold}:	average surface density of gold particles
$DiIC_{16}$:	1,1'-dihexadecyl-3,3,3,',3'-tetramethylindocarbocyanine perchlorate
DIPC:	diisopropylcarbodiimide
DNP:	2,4-dinitrophenyl

DOPC:	1,2-Dioleoyl-sn-Glycero-3-phosphocholine
DOPG:	1,2-dioleoyl-sn-glycero-3-[phospho-rac-(1-glycerol)]
DPPE:	dipalmitoyl-phosphatidylethanolamine
DPTS:	4-(dimethylamino)pyridium-4-toluenesulfonate
DRM:	detergent resistant membrane
ECM:	extracellular matrix
ESR:	electron spin resonance
FCCS:	fluorescence cross-correlation spectroscopy
FITC:	fluorescein isothiocyanate
FFT:	Fast Fourier Transform
FRET:	fluorescence resonance energy transfer
GFP:	green fluorescent protein
GM_1:	monosialotetrahexosylganglioside
GPI:	glycophosphatidylinositol
GPMV:	giant plasma membrane vesicles
G(r):	pair correlation function
GUV:	giant unilamellar vesicle
IP3:	inositol trisphosphate
ITAM:	immunoreceptor tyrosine-based activation motif
ITIM:	immunoreceptor tyrosine-based inhibitory motif
K(r):	Ripley's K Function
L(r)-r:	modified Ripley's K Function
LAT:	linker for activation of T cells

l_d: liquid disordered phase

LE: labeling efficiency

l_o: liquid ordered phase

LOR: lift off resist

mAb: monoclonal antibody

MβCD: methyl-beta-cyclodextrin

MDCK: Madin-Darby canine kidney

MHC: major histocompatibility complex

MIRR: multichain immune recognition receptor

MMP: matrix metalloprotease

N_{gold}: number of gold particles

N_{cl}: number of proteins per cluster

PAA: poly (acrylic acid)

PALM: photo-activated localization microscopy

pAb: polyclonal antibody

PEG: poly (ethylene glycol)

PI3K: phosphoinositide 3-kinase

PIP2: phosphatidylinositol 4,5-bisphosphate

PKC protein kinase C

PLAP: placental alkaline phosphatase

PLCγ: phospholipase C gamma

PP1: Protein Phosphatase 1

PTPα: protein tyrosine phosphatase alpha

RBL-2H3: rat basophilic leukemia 2H3 cell line

RGD: arginine-glycine-aspartate

SAM: self assembled monolayer

SDG: sucrose density gradient

SED: secondary electron detection

SEM: scanning electron microscopy

SH2: src homology 2 domain

σ: half-width of Guassian shaped clusters

SLE: systemic lupus erythematosus

s_o: gel phase

SPT: single particle tracking

Src : sarcoma

STED : stimulated emission depletion microscopy

STORM : stochastic optical reconstruction microscopy

Syk : spleen tyrosine kinase

TCR: T cell receptor

TCZ: transient confinement zone

TEM : transmission électron microscopy

TR: Texas Red

TX-100: Triton X-100

XPS: X-ray Photoelectron Spectroscopy

YFP: Yellow Fluorescent Protein

ZAP-70: zeta-chain-associated protein kinase 70

CHAPTER ONE

Introduction

1.1 A Very Brief History

Researchers have sought to describe the structure and function of the plasma membrane since the name "plasma skin" was first coined in the late 1800s to describe the protective barrier surrounding the cell. Early functional studies of osmosis revealed that cell membranes passively and actively regulate the exchange of solutes between the extracellular medium and cytoplasm (potentially through a protein-based mechanism) [1]. Subsequent permeability studies revealed that the capacity of a molecule to cross the plasma membrane is directly correlated to its oil/water solubility coefficient (i.e., its solubility in oil compared to water) [2]. Thus, the plasma membrane was compositionally and functionally defined as a 'lipid impregnated boundary' containing cholesterol and phospholipids that selectively regulate membrane permeability under passive and active mechanisms [3].

In the first half of the twentieth century it was suggested that the lateral organization of proteins and lipids at the plasma membrane had functional consequences in regulating selective permeability. Early models portrayed cell surfaces as mosaic-like patterns of water permeable (lipids) and impermeable (protein) molecules [4]. Following the discovery that membranes were composed of bilayers [5], it was proposed that the adsorption of unstructured globular proteins at the exoplasmic and cytoplasmic leaflets regulated permeability through electrostatic shielding [6]. However, most contemporary conceptual descriptions of general membrane

organization stem from the 'fluid mosaic model,' which was proposed by Singer and Nicholson in 1972 and illustrated in Figure 1.1 [7]. According to this model, the plasma membrane behaves as a two dimensional homogenous liquid through which lipids and proteins (attached to the membrane, as well as embedded) freely diffuse.

While this model assumes that lipids and proteins freely diffuse due to the absence of long range ordering, early model membrane studies revealed that lipids with different biophysical properties have varying propensities to interact with one another. Additionally, it was revealed that cell surface proteins are not freely diffusing and can undergo different types of diffusion, including transient confined diffusion within spatially distinct zones [8-10]. Several models have been proposed to describe these transient confinement zones (TCZs), including work by Kusumi and colleagues [11-14]. According to the 'anchored protein picket fence model', proteins are bound to the underlying actin skeleton and act as boundaries that restrict the diffusion of both lipids and proteins [15, 16].

One model that attributes functional consequences to distinctly organized lipid domains is the 'lipid raft hypothesis' [17] . According to this model, lipids have the propensity to differentially organize into distinct domains based on their physical mixing properties. The preferential association of cholesterol, sphingomyelin, and other ordered, saturated phospholipids creates metastable microdomains, which are enriched in a selected subset of proteins and exclude others. While lipid rafts defined in this manner have been implicated in many cellular processes, such as protein trafficking, cell motility, and signal transduction, the physical and functional basis for their existence has yet to be fully elucidated.

The thorough characterization of lipid rafts has been difficult due to the ubiquitous use of the term 'raft' to describe many different types of membrane heterogeneities. For example, lipid rafts are often operationally described as 1) detergent resistant membrane (DRMs), 2) liquid ordered membranes, and 3) micro- and nano-sized lipid and protein-containing clusters 'visualized' by various experimental techniques. While a general consensus on the nature of rafts has not yet been reached, ever emerging studies of microdomains in model and biological membranes continue to contribute to our understanding of the functional basis for lateral heterogeneity at the plasma membrane of living cells.

1.2 Model Membrane Studies

The plasma membrane of mammalian cells is a complex structure containing many different types of lipids, including glycolipids, phospholipids, and sterols. According to the fluid mosaic model [7] described above and illustrated in Figure 1.1, the plasma membrane contains many embedded proteins which freely diffuse through the lipid bilayer. This fluidity is attributed to the lateral mobility of lipids within the bilayer and can be described by lipid phase behavior. In typical cholesterol-free phospholipid bilayers, non-polar acyl chains of adjacent lipids interact with one another through van der Waals interactions, and the degree of these interactions depends on lipid structure, mainly chain length and degree of saturation. If acyl chains are well ordered, the bilayer exists in the solid or gel phase, s_o, and lipids are relatively immobile. However, if acyl chains are disordered and van der Waals interactions are low, the bilayer assumes the liquid disordered phase, l_d, in which lipids are freely diffusing.

Adapted from: Singer, S.J. et al., *The fluid mosaic model of the structure of cell membranes*, Science, 1972 **175** (23):p. 720-731.

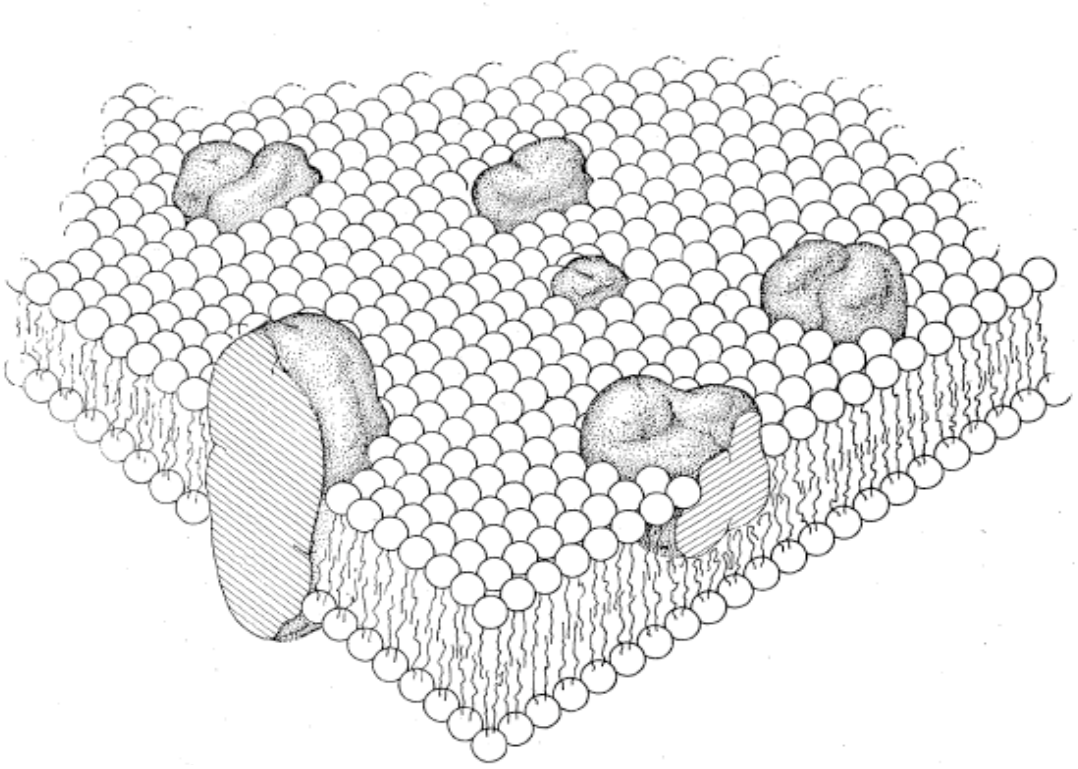

Figure 1.1: A cross-sectional and three-dimensional schematic of the plasma membrane according to the fluid mosaic model. Freely diffusing globular, integral proteins are embedded within the lipid bilayer.

Lipids in a bilayer can exist in either the solid or liquid phase, and the temperature at which a lipid 'melts' from a solid to a liquid is called its melting temperature, T_m. If lipid mixtures contain components with different melting temperatures, solid and liquid phases can co-exist. While early observations of solid-liquid phase separation in phospholipid bilayers provided an attractive basis for the origins of plasma membrane heterogeneity, it is argued that lipids rarely exist in the solid phase in living cells at physiological temperatures.

One unique feature of biological membranes in mammalian cells is the high concentration of cholesterol at the plasma membrane. Given its unique structure and abundance, a significant deal of work has been done to understand the role of cholesterol in lipid organization. As early as the 1920s, cholesterol containing model monolayer membranes revealed that phospholipids and cholesterol undergo non-ideal mixing due to lipid condensation [18]. Due to its small size and rigid structure, cholesterol acts as membrane fluidizer by disrupting packing order in the solid phase and stabilizing disordered acyl chains in the liquid phase [19]. The exact mechanism through which cholesterol stabilizes lipid chain order is not definitively known, although several models have been proposed, including the condensed complexes model [20], superlattice model, and umbrella model [21].

In addition to s_o and l_d phases, binary and ternary model membranes containing cholesterol have revealed the existence of liquid-liquid immiscibility, in which lipids phase separate into co-existing l_d, previously described, and liquid ordered, l_o, phases. In the l_o phase, lipids diffuse

laterally as a liquid, yet have highly ordered acyl chains approaching that of a solid. The observation of co-existing liquid phases in synthetic model membranes is a significant finding because it provides the first plausible physical mechanism for lipid-driven domain formation in living cells [22]. In addition to synthetically composed model membranes, cholesterol – dependent macroscopic liquid-liquid immiscibility has been observed in biologically derived model membranes extracted from cell plasma membranes rich in cholesterol, sphingomyelin, and glycosphingolipids [23].

Interestingly, work by Hammond et al. demonstrated that crosslinking of a minor membrane component, GM_1, induced liquid-liquid phase separation in PC/cholesterol/sphingomyelin containing model membranes [24]. Crosslinking GM_1 also caused the transmembrane peptide of linker for activation of T cells, LAT, an important signaling protein in immune cell signaling, to partition into a separate phase as shown in Figure 1.2. The significance of these experiments in suggesting functional roles for phase separated l_o/l_d domains is underscored by in vivo observations that crosslinking of cell surface GPI-anchored proteins, which associate with l_o domains, can induce signaling responses in cells [25].

Adapted from: Hammond A.T. et al., *Crosslinking a lipid raft component triggers liquid-ordered disordered phase separation in model plasma membranes*. Proc. Natl Acad USA, 2005. **102** (18):p. 6320-5.

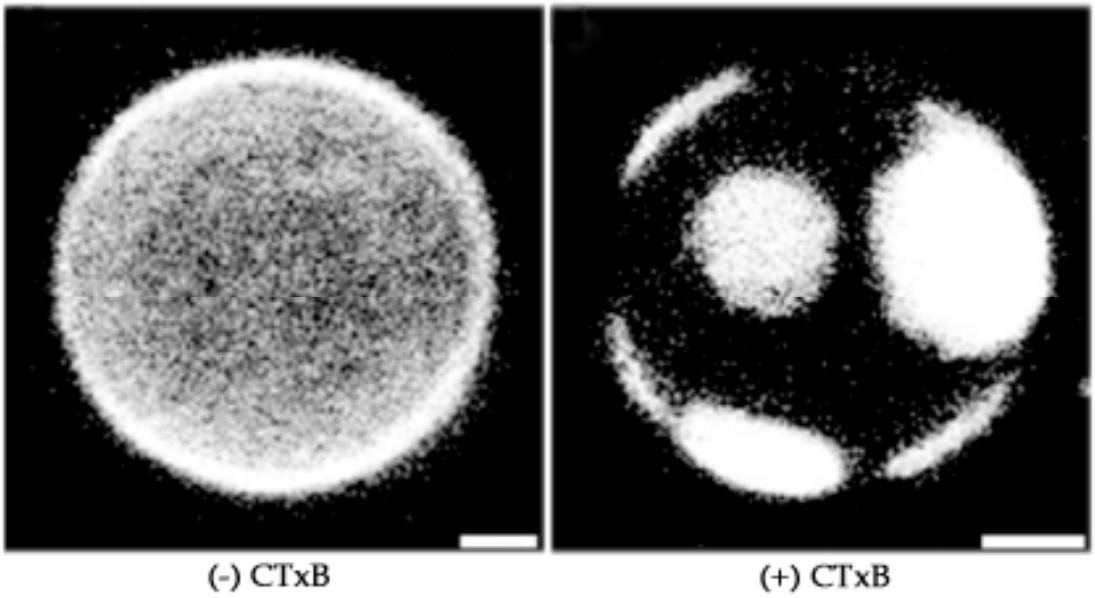

Figure 1.2: Binding of CTxB to GM_1 changes the phase state of the membrane. Crosslinking of GM_1 by CTxB results in the partitioning of the transmembrane peptide of LAT into the l_d phase. Bright areas represent rhodamine labeled LAT. GUVs are composed of DOPC:DOPG:Sph:Chol:GM_1 (44.1:4.9:19:30:2 mol%). Scale bar is 5μm.

While microscopic phase separation provides an attractive mechanism for the lateral segregation of membrane components into distinct cell surface domains, living cell membranes do not typically exhibit microscopic liquid-liquid immiscibility at physiological temperatures. However, recent FRET studies have demonstrated, in the absence of phase separation, the existence of ordered nano-scale (tens of nanometers) domains at physiological temperatures in model membranes with lipid compositions similar to that of the outer leaflet of mammalian plasma membranes [26]. Using a similar technique, these findings were extended by Sengupta et al. to demonstrate that lipids in the plasma membrane of living cells exhibit nanoscopic l_o/l_d heterogeneity [27].

Given the observation that nano-scale heterogeneity can arise in the absence of microscopic phase separation, it has recently been suggested that the physical basis for the formation of these domains may be explained by critical membrane phase behavior [28]. Using fluorescence microcopy, Veatch et al. demonstrated that giant plasma membrane vesicles (GPMVs) exhibited robust critical fluctuations near their phase miscibility transition temperature, T_c. Accordingly, predictions from the 2D Ising model suggest that the size of these fluctuations is ~ 20 nm at physiological temperatures, which is comparable to size predictions for lipid rafts in living cells [29].

1.3 Plasma Membrane Microdomains

Over a decade ago, Simons and Ikonen proposed that plasma membrane microdomains, called lipid rafts, exist that are rich in cholesterol and sphingolipids [28]. In this model, a particular subset of membrane components selectively associate with rafts, and these specialized membrane

microdomains have important functional roles in many cellular processes, such as protein trafficking, cell motility, lipid metabolism, and signal transduction. The conceptual framework that underlies this hypothesis originates from the observation that GPI-anchored proteins and glycosphingolipids are specifically trafficked to the apical (and not basolateral) membrane of polarized epithelial cells. To explain the polarized delivery of proteins lacking intracellular targeting sequences, Simons and van Meer proposed that GPI-anchored proteins preferentially associate with glycosphingolipids in the Golgi where they are compartmentalized into vesicles bound for apical microdomains [30], as depicted in Figure 1.3.

The original lipid raft definition, as proposed by Simons and Ikonen, has since evolved to incorporate the characteristic properties of DRMs, as well as liquid ordered membranes. Evidence for this comes from the observation that GPI-anchored proteins, cholesterol, and glycosphingolipids (which are spatially compartmentalized in polarized epithelial cells) are enriched in DRMs extracted from the same cells. Further, DRMs prepared from l_d/l_o phase separated model membranes (containing cholesterol, sphingomyelin, and phosphatidylcholine) revealed that DRMs are enriched in liquid ordered membranes. While 'lipid rafts', 'DRMs', and 'liquid ordered domains' have similar characteristics, mainly high levels of cholesterol and sphingolipids, they are not identical structural concepts. This is further complicated by the observation that biochemical criteria (detergent resistance and cholesterol modulation) for characterizing these microdomains have the potential to introduce artifacts in raft structure and composition.

Adapted from: Simons, K. & van Meer, G., *CLipid sorting in epithelial cells*, Biochemistry, 1988. **28** (17):p. 6197-6202 and Lipschutz, J.H., *Analysis of membrane traffic in polarized epithelial cells*, Current Protocols in Cell Biology, 2001. Chapter 15:Unit 15.5.

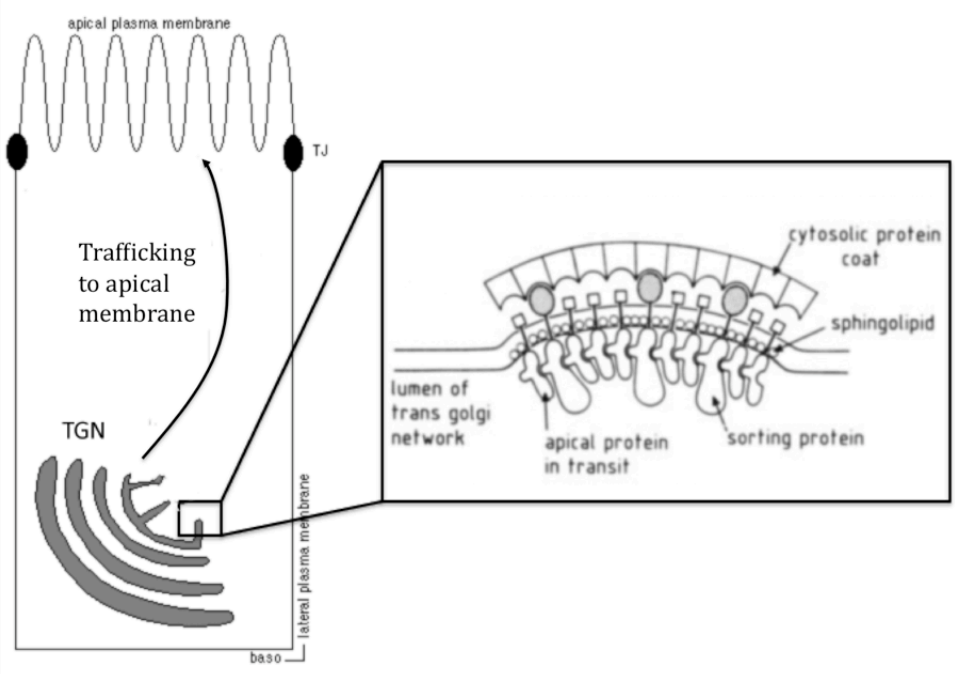

Figure 1.3: A subset of GPI-anchored proteins and glycosphinoglipids are compartmentalized in the Golgi and specifically trafficked to the apical membrane in polarized epithelial cells. The zoomed in region (right) depicts lipid/protein domains containing sphingolipids and apical bound proteins required for polarized membrane trafficking.

Since the introduction of the lipid raft hypothesis, the composition, size, structure, and physiological significance of lipid rafts has been the subject of significant debate. In fact, some have even postulated that lipid rafts do not exist [31]. The difficulty in providing definitive evidence for the existence of functional lipid rafts lies in the inability to directly visualize these structures at high spatial and temporal resolution using optical microscopy. If lipid rafts are larger than the resolution limit of light microscopy, they should be directly visualized by fluorescence microscopy (either by immunofluorescence labeling of proteins or by visualizing fluorescent lipid analogues or fluorescently expressing proteins). However, most fluorescence microscopy studies report relatively uniform plasma membrane labeling and fail to detect protein/lipid clusters indicative of lipid rafts. This failure may be due to the low enrichment of the labeled component within raft structures, limited spatial resolution to detect very small rafts, or limited temporal resolution to detect transient short-lived rafts.

Despite these inherent challenges, fluorescence microscopy, fluorescence resonance energy transfer (FRET), single particle tracking, and electron microscopy have revealed interesting information about lipid rafts and membrane heterogeneity. Reports of lipid raft size have varied from hundreds of nanometers down to tens of nanometers containing only a few molecules [9, 31, 32]. For example, homo-FRET measurements have suggested that 20-40% of GPI-anchored proteins are clustered into 4-5 nm clusters in living cells [33]. Despite reports that raft-associated GPI-anchored proteins have clustered distributions, FRET studies have reported unclustered distributions in MDCK, Cos-7, and Jurkat T cells [34, 35]. These observations are supported by single particle epifluorescence studies that report random

distributions of the Class 2 MHC proteins [36]. Interestingly, immuno-gold electron microscopy studies have suggested differential nano-scale heterogeneity for two raft-associated proteins, in which Thy-1 is clustered while GM_1 is random [37].

Early fluorescence single particle tracking (SPT) experiments revealed that GPI-anchored proteins, glycosphingolipids, and phospholipids can undergo non-random hindered diffusion within transient confinement zones (TCZs) ranging in size from tens to hundreds of nanometers [8-10, 15]. Akin to the previous hallmark of slowed lipid and protein diffusion within l_o model membranes, cholesterol and glycosphingolipid depletion was shown to decrease the abundance of TCZs, suggesting that hindered diffusion occurs within raft-like ordered microdomains [9, 15]. Studies investigating the effects of cytoskeletal perturbations and cleavage of cytosolic domains of transmembrane proteins have suggested that membrane-cytoskeleton interactions promote the formation of TCZs [12-14, 38, 39]. Accordingly, the 'membrane skeleton fence model,' suggests that interactions between the cytoplasmic domains of transmembrane proteins and the cytoskeleton cause transient confinement of nearby or associated proteins [11].

Ultra fast SPT experiments (25 microseconds per frame) have proposed that the plasma membrane may be organized into many different compartments ranging in size from 30-230 nm (depending on the cell type) [16]. For example, the transferrin receptor freely diffuses within 260 nm compartments at short time-scales (~55 ms), but 'hops' between larger 710 nm compartments at long time-scales (~1800 ms). Further, the formation of these compartments was insensitive to cholesterol depletion (i.e., not lipid raft mediated), and perturbation of the cytoskeleton had significant effects on both

compartment size and residency time within compartments. This is consistent with observations that lipids diffuse more slowly in plasma membranes (due to cytoskeletal compartmentalization) than in GUVs or GPMVs that lack an underlying cytoskeleton. Thus, in contrast to previous interpretations of confined diffusion, hindered diffusion may be a result of freely diffusing proteins 'hopping' between compartments at long time scales, rather than a consequence of slowed lipid and protein diffusion [16, 40]. Complementary to the membrane skeleton fence model, the 'anchored-protein picket model' proposes that the transient confinement of lipids results from the anchoring of transmembrane proteins to the cytoskeleton at 3-10 nm intervals, like pickets on a fence [16].

Using similar SPT techniques, Suzuki et al demonstrated that crosslinked GPI-anchored proteins are also confined within ~100 nm compartments. However, unlike monomeric GPI-anchored proteins, diffusion of crosslinked protein clusters between compartments was reduced in a cholesterol and Src family kinase activity dependent manner [41]. Additionally, these crosslinked clusters were shown to bind actin-associated sites, presumably by the association of actin-binding transmembrane proteins [41].

From these and previous observations, a hierarchy of lipid raft structures that differ in size, composition, and stability have been proposed. Pulse electron spin resonance (ESR) labeled and monomeric SPT experiments posit that lipid rafts may represent very transient and short-lived structures in which components diffuse in and out of rafts with a time-scale of 100 μs or less [42]. These raft structures are small and energetically unstable, and they consist of a limited number of outer leaflet-anchored proteins or inner leaflet

signaling proteins (such as Src family tyrosine kinases). After transmembrane or GPI-anchored receptor crosslinking, rafts become stabilized through the preferential association of cholesterol, sphingomyelin, and glycosphingolipids with saturated acyl chains. Coupling of outer and inner leaflet rafts may result in the formation of 'signaling rafts'. It is well known that crosslinked GPI-anchored proteins, which lack cytosolic signaling domains, are able to recruit intracellular signaling proteins and initiate signaling cascades. For example, crosslinking of Thy-1 results in calcium mobilization in murine and human T and B cells, as well as LAT in RBL-2H3 mast cells [43, 44].

Several studies have investigated whether inner leaflet rafts redistribute in concert with crosslinked GPI-anchored proteins. For example, Harder et al. demonstrated that crosslinking of the GPI-anchored protein placental alkaline phosphatase (PLAP) resulted in co-redistribution of Fyn, a raft associated Src family tyrosine kinase [45]. High-resolution SPT studies have also shown that crosslinking of GPI-anchored Thy-1 induces the transient recruitment and clustering of inner-leaflet anchored Lyn kinase [46]. Although the exact mechanism and extent to which outer and inner leaflet lipid rafts are coupled is unclear, it has been suggested that crosslinking GPI-anchored proteins imparts stability to lipid rafts by promoting stable association with cholesterol and saturated glycosphingolipids. The local ordering within crosslinked clusters could result in preferential recruitment of signaling-capable transmembrane proteins on the basis of either raft affinity or protein-protein interactions. Additionally, clustered GPI-anchored and transmembrane protein complexes may be stabilized through cytoskeletal binding interactions within cholesterol-dependent microdomains [25, 41]. Although expected to be a weak interaction energy, it has also been proposed

that the interdigitated structure of crosslinked outer leaflet rafts could cause transient stabilization of signaling protein rich inner leaflet rafts [42, 47].

1.4 Role of Rafts in Immune Cell Signaling and Disease

Further evidence that lipid rafts are involved in signal transduction comes from studies of B cell antigen receptor (BCR), T cell antigen receptor (TCR), and the high affinity IgE receptor (FcεRI) activation in B and T leukocytes and mast cells, respectively. Each of these multichain immune recognition receptors (MIRRs) possess extracellular ligand binding domains, as well as cytosolic domains that contain tyrosine residues within immunoreceptor tyrosine-based activation motifs (ITAMs). Because MIRRs do not have inherent kinase activity, receptor activation results from the crosslinking-dependent phosphorylation of receptor ITAMs by Src family kinases. Schematic representations of these ITAM-containing MIRRs are illustrated in Figure 1.4.

T Cell Signaling

In T leukocytes, crosslinking of TCR by major histocompatibility complexes (MHCs) expressed on the surface of antigen presenting cells (APCs) induces the phosphorylation of receptor ITAMs by the kinase Lck. Subsequent recruitment of Syk and ZAP-70 to phosphorylated receptor tyrosine residues leads to activation of LAT, which serves as a docking site for a host of different signaling molecules, including SLP-76, PLCγ, and PI3K. The redistribution of these signaling proteins occurs within spatially regulated structures called immunological synapses, which have been shown to be enriched in lipid raft components [48].

Adopted from: Kinet J. et al., *Signaling through the high-affinity IgE receptor FcεRI*. Nature, 1999. **402** (6760 Suppl):p. B24-30.

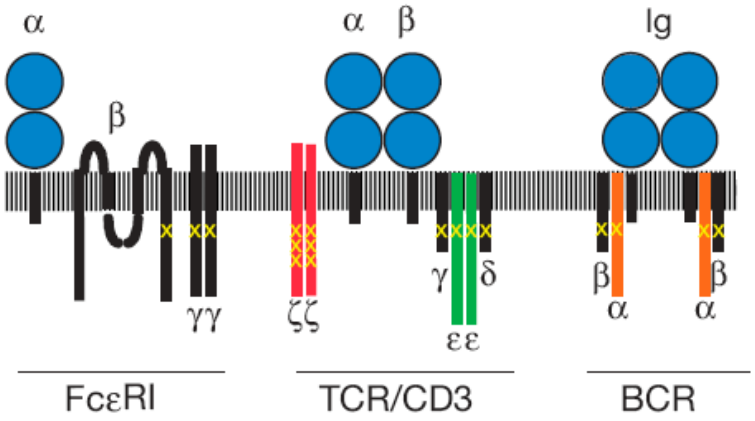

Figure 1.4: Schematic depicting the following ITAM-containing MIRRs: high affinity IgE receptor, T cell antigen receptor, and B cell antigen receptor. The blue circles represent immunoglobular domains, and the yellow crosses represent ITAM motifs. Upon receptor activation, phosphotyrosine residues within these ITAMs act as docking sites for SH2 domain-containing signaling proteins.

It has also been shown that lipid raft association of Lck and LAT occurs through palmitoylation of these proteins, and removal of these lipid moieties results in impaired TCR signaling [49, 50]. Further evidence for lipid raft involvement in TCR signaling comes from reports that 1) TCR crosslinking induces the translocation of multiple tyrosine phosphorylated proteins (such as PLCγ1, ZAP-70, and TCR itself) into lipid rafts isolated by sucrose density gradients (SDGs) and 2) raft-associated Lck is recruited to crosslinked TCRs, visualized by fluorescence microscopy [51, 52]. Additionally, cholesterol depletion has been shown to cause spontaneous, phosphorylation-induced, signaling cascades in the absence of TCR ligation, implicating lipid rafts with roles in homeostatic regulation of TCR signaling [53].

B Cell Signaling

In B cells, the BCR comprises a multi-chain spanning IgM sequence (that binds extracellular ligands) complexed with an Igα/Igβ heterodimer (containing cytoplasmic signaling sequences). Upon BCR crosslinking, receptor ITAMs become phosphorylated by Src family kinases, such as Lyn, Fyn, and Blk. Similar to T cells, Syk is recruited to phosphorylated receptor ITAM residues via its SH2 domains where its subsequent phosphorylation activates B cell linker protein, BLNK, and other downstream signaling proteins. In addition to activating downstream signaling proteins, Lyn also plays a significant inhibitory role by phosphorylating immunoreceptor tyrosine-based inhibition motifs (ITIMs) on proteins such as CD22, which recruits and activates downregulatory phosphatases, such as SHIP-1 and SHP1. Thus, Lyn plays a key regulatory role in BCR signaling. Consequently, Lyn deficient/impaired animal models display a host of aberrant phenotypes,

such as unregulated BCR signaling, reduced B cells, B cell hypersensitivity, and autoimmunity diseases such as glomerulonephritis [54, 55]. Given the many pathological similarities of this disease to human systemic lupus erythematosus (SLE), Lyn deficient/impaired model systems can provide useful insight the molecular basis for human diseases [56].

DRM studies have revealed that crosslinked BCR translocates to Lyn-containing lipid raft fractions, similar to crosslinked TCR association with lipid rafts in T cells. Consistent with raft-mediated BCR signaling, disruption of cholesterol-sensitive microdomains by filipin has been shown to significantly reduce BCR-mediated calcium mobilization, as well as inhibit the phosphorylation of PLCγ2 by Syk and Btk [57, 58]. Interestingly, work by Flores-Borja et al. found a positive correlation between reduced raft-association with Lyn in human patients suffering from SLE [59]. According to this study 1) total Lyn expression was reduced in 52% of SLE patients and 2) Lyn levels in lipid raft fractions obtained from those patient's B cells were reduced by 34%. These patients also exhibited reduced Lyn association with rafts, as demonstrated by a 20% reduction in co-localization of Lyn with the raft-marker GM_1-CTxB [59]. Collectively, these findings implicitly underscore a role for lipid rafts in human disease and motivate further studies to understand plasma membrane heterogeneities.

IgE-FcεRI Signaling in RBL-2H3 Mast Cells

RBL-2H3 mast cells have many signaling similarities to B and T leukocytes and provide a well-studied model system for investigating the molecular mechanisms that drive the redistribution of membrane proteins after stimulation with multivalent antigen. These cells express the high

affinity IgE receptor, FcεRI, which binds IgE with a high affinity (K_d~10^{-10} M). Ligand induced receptor crosslinking triggers a complex signaling cascade that is initiated by the phosphorylation of tyrosine residues within ITAMs on the β and γ subunits of IgE-FcεRI by Lyn. These phosphorylated tyrosine residues then act as docking sites for additional Lyn and Syk [60, 61], (similar to ZAP-70 in T cells). Phosphorylated PLCγ, which binds phosphorylated LAT at the plasma membrane via its SH2 domain, then hydrolyzes phosphatidylinositol-4,5-bisphoshpate (PIP2) into inositol-1,4,5-triphosphate (IP3) and diacylglycerol (DAG). Activation of protein kinase C (PKC) by DAG, as well as IP3-mediated calcium mobilization, promotes the release of secretory granules containing allergic mediators and cytokines into the extracellular environment.

While studies continue to reveal the plethora of signaling players involved in IgE-FcεRI-mediated signaling, the mechanism that drives their reorganization upon cell stimulation, as well as the physiological significance of lateral membrane heterogeneity in general, requires further study. Fluorescence microscopy studies of receptor organization reveal optically uniform labeling of the receptor at the plasma membrane. After stimulation, receptors redistribute into patchy micron-sized cell surface domains [62, 63]. Stabilization of these large patches without internalization of the clustered receptors requires incubation for several hours at low temperatures (typically 4°C. Subsequent studies under these conditions also demonstrated that fluorescently labeled Lyn co-redistributes into the same punctate plasma membrane microdomains [64-66]. As an alternative to soluble antigen stimulation, patterned antigen-containing supported bilayers provide a useful strategy for spatially regulating the size of cross-linked receptor complexes.

Using this technique, Wu et al. demonstrated that Lyn and actin selectively redistribute to micron sized crosslinked receptor clusters at 37˚C [67] shown in Figure 1.5. Further support for this compartmentalization comes from fluorescence cross-correlation spectroscopy (FCCS) studies, which demonstrated a stimulation dependent enhancement in cross-correlation between between IgE-FcεRI and Lyn [68]. Although the physical basis for the recruitment of Lyn to crosslinked IgE-FcεRI at early signaling times is unclear, two models have emerged that implicate both protein-protein interactions, as well as lipid-mediated or 'lipid raft' interactions.

Studies have also suggested that ordered microdomains or 'lipid rafts' play an important role in facilitating IgE-FcεRI and Lyn interactions during mast cell activation. Biochemical isolation of DRMs prepared from resting RBL-2H3 cells have been shown to be enriched in GPI-anchored proteins, Src family tyrosine kinases such as Lyn and Syk [69], and LAT [70-72]. Although IgE-FcεRI is largely excluded from DRMs in resting cells, stimulation with multivalent antigen causes IgE-FcεRI to associate with tyrosine kinase rich DRMs [73, 74]. Thus, it has been proposed that antigen stimulation causes a translocation or stabilization of crosslinked receptor clusters to ordered microdomains.

Adopted from: Wu, M. et al., *Visualization of plasma membrane compartmentalization with patterned lipid bilayers*. PNAS, 2004**. 101** (38):p. 13798-13803.

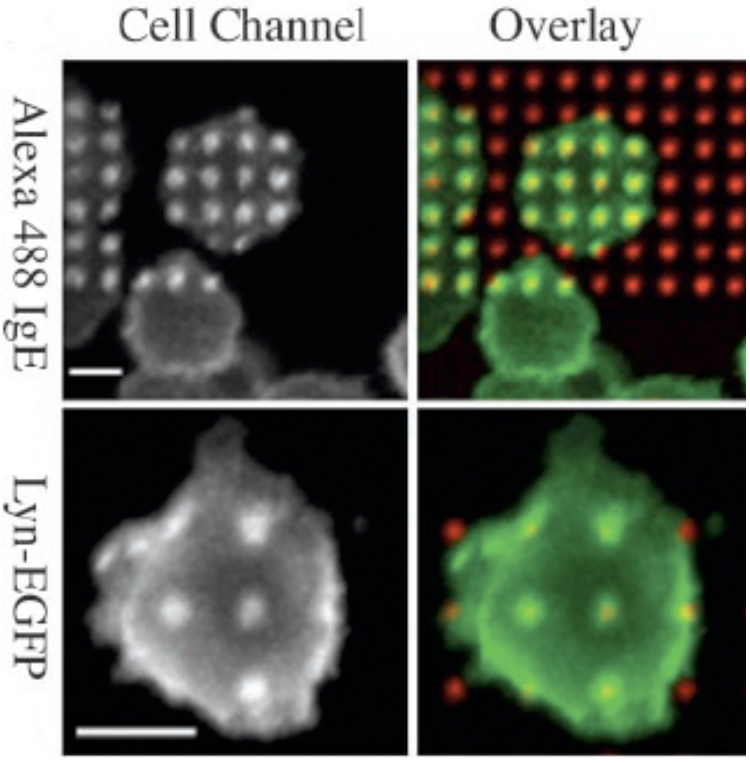

Figure 1.5: IgE-FcεRI and Lyn are recruited to micro-patterned antigen-containing lipid bilayers. Green fluorescence is used to visualize the distribution of A488-labeled IgE-FcεRI (top right) and GFP-expressing Lyn (bottom right) in separate experiments. In both overlays, red fluorescence visualizes the antigen-containing lipid bilayers underlying the cells.

The formation of ordered microdomains has been shown to depend critically on cholesterol, and reduced plasma membrane cholesterol levels severely influences IgE-FcεRI and Lyn interactions. In addition to inhibiting receptor phosphorylation, treatment with the cholesterol depleting agent methyl-beta-cyclodextrin (MβCD) prevents stimulation dependent association of receptors with DRMs as well as micron scale co-clustering of IgE-FcεRI and Lyn visualized by fluorescence microscopy [64]. It has also been demonstrated that improper targeting of Lyn to lipid rafts, via mutated myristoylated and palmitoylated acyl chains, prevents co-clustering of Lyn with crosslinked IgE-FcεRI [66].

Additionally, Young et al. demonstrated that Lyn kinase has a 4-5 fold higher activity in lipid raft-associated membranes versus non raft-associated membranes, further supporting lipid raft-mediated interactions between IgE-FcεRI and Lyn [75]. Subsequent demonstration that the active site of Lyn is more protected from dephosphorylation by transmembrane protein tyrosine phosphatase α (PTPα) within lipid rafts suggests that raft-resident activated IgE-FcεRI may also be protected from the same deactivating phosphatases [76].

An alternative model proposes that receptor phosphorylation and subsequent recruitment of Lyn to crosslinked IgE-FcεRI is mediated by protein-protein interactions. This model arises from early observations by Metzger and colleagues [77-79] that a small percentage of active Lyn is constitutively associated with IgE-FcεRI in resting cells through weak protein binding interactions via the N-terminal unique domain of Lyn. According to the 'transphosphorylation model', receptor crosslinking brings Lyn into close proximity to adjacent receptors that are subsequently phosphorylated. A

related mechanism for tyrosine phosphorylation-independent activation of BCR in B cells has been suggested based on similar observations that the Igα subunit of BCR is constitutively associated with the kinase Syk [80], as well as certain Src family kinases prior to receptor cross-linking [81, 82].

Additionally, studies using Tac receptor chimeras containing the cytoplasmic domain of the β and γ IgE receptor subunits have suggested that receptor phosphorylation by Lyn does not require receptor association with ordered microdomains [83]. Further evidence for this model comes from the observation that Lyn association with lipid rafts is not required for sufficient receptor phosphorylation by Lyn [66]. However, in the same study, the SH2 domain-dependent co-redistribution of Lyn with crosslinked IgE-FcεRI is postulated to occur with lipid raft environments. Thus, the mechanism responsible for IgE-FcεRI and Lyn association during early signaling events may very well result from both protein-protein and lipid-mediated interactions.

1.5 High-Resolution Studies on Membrane Heterogeneity

One of the major challenges in deciphering different models of membrane organization is directly visualizing plasma membrane protein organization at high resolution. Fluorescence microscopy studies carried out at low temperatures or with patterned substrates have revealed a stimulation-dependent micron-scale reorganization of IgE-FcεRI and associated signaling proteins into cell surface clusters. However, high spatial resolution of the size and composition of these microdomains under normal conditions is limited by the wavelength of light. Electron microscopy overcomes this barrier because the wavelength of an electron beam is much smaller than that of a photon of

light. Plasma membrane protein distributions, labeled with gold particles conjugated to specific antibodies, can be directly visualized using high resolution microscopy techniques.

Scanning electron microscopy (SEM) with both secondary electron detection (SED) and backscattered detection (BSD) allows direct visualization of membrane topography and protein distributions on the top surface of intact cells. The utility of this technique was first demonstrated over two decades ago by labeling cell surface proteins with 20 and 45 nm gold particles in human peripheral granulocytes [84]. Further studies by Stump et al., which monitored gold labeled IgE-FcεRI organization in stimulated RBL-2H3 cells, demonstrated that changes in membrane morphology could be correlated with receptor distributions [85]. Using the same technique, Johkura et al. demonstrated that a specific subset of cell surface proteins were preferentially localized to membrane ruffles and microvillii, while others had random topological distributions [86].

More recently, transmission electron microscopy (TEM) has been used to visualize immuno-gold labeled proteins on 'ripped-off' membrane sheets [87]. In this technique, the top surface of adherent living cells is detached as a continuous, cytoplasmic leaflet-exposed plasma membrane sheet and transferred directly to an electron microscopy grid. Proteins are then labeled with gold particles and imaged using high resolution TEM. Several of these studies have suggested that a wide variety of plasma membrane proteins have self-clustered distributions in resting cells, within spatially distinct cell surface microdomains, ranging in size from ~10-100 nm [71, 88-91], as visualized in Figure 1.6.

Adapted from: Prior, I.A. et al., *Direct visualization of Ras proteins in spatially distinct cell surface microdomains.* J Cell Biol, 2003. **160** (2): p. 165-170.

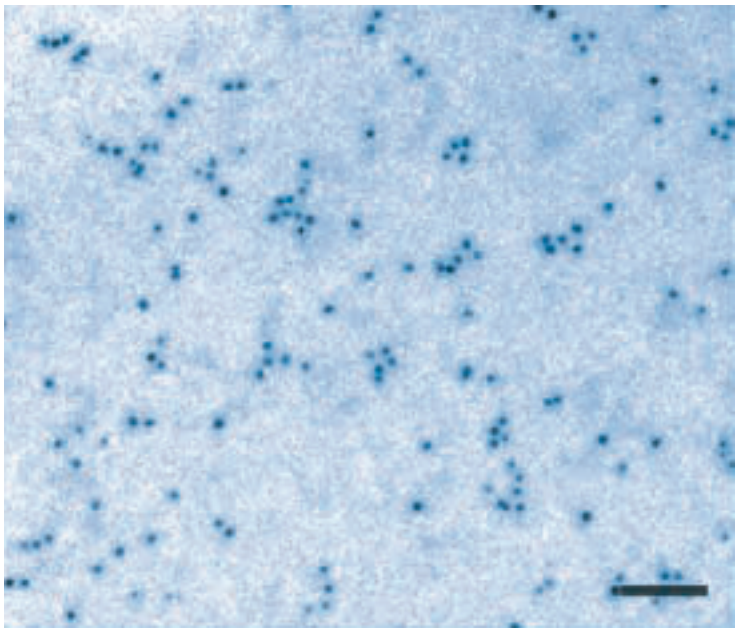

Figure 1.6: Gold particles labeling the inner-leaflet associated protein K-ras have self-clustered distributions in `ripped off' membrane sheets prepared from resting cells. Gold particles are 5 nm in size, and the scale bar is 50 nm.

Several studies have used 'ripped-off' sheets prepared from RBL-2H3 cells to monitor the distribution of IgE-FcεRI and associated signaling proteins before and after multivalent antigen stimulation [89, 90, 92]. In resting cells, Wilson et al. report that IgE-FcεRI, Lyn, Syk, and LAT have significantly clustered distributions, with LAT clusters being the largest (majority of IgE and Lyn clusters contain < 10 golds compared to 20 golds for LAT). While LAT clusters are spatially distinct from IgE-FcεRI, 20% of gold-labeled Lyn is observed to associate with receptor clusters in resting cells, consistent with previous biochemical evidence [79].

Further, Wilson et al. propose that stimulation with multivalent antigen induces rapid phosphorylation of IgE-FcεRI by Lyn, followed by a rapid segregation of crosslinked IgE-FcεRI away from Lyn into osmiophilic membrane patches concentrated in Syk, PLCγ2, PI3K, and Gab2. In contrast, LAT forms large clusters, rich in PLCγ1 and PI3K, which occasionally intersect but do not mix with crosslinked IgE-FcεRI domains [89, 90]. From these observations, it has been suggested that mast cells form primary signaling domains around IgE-FcεRI and Syk, while secondary signaling domains are organized around LAT. The high concentration of LAT within secondary signaling domains has been proposed to have functional significance for sustaining and amplifying signaling at long stimulation times as IgE-FcεRI is internalized [90].

While these studies suggest an intriguing mechanism for the redistribution of IgE-FcεRI-associated signaling proteins in activated mast cells, there are several important factors that need to be addressed. In many cases, descriptions of 'clustered distributions' are qualitative observations that may unfairly bias and/or misrepresent protein distributions. While previous

statistical analyses of these particle distributions using Ripley's Functions are well suited for determining whether particles are clustered over a random distribution, quantitative information about the size and composition of particle clusters is often difficult to extract. Lastly, it remains unclear to what degree the action of membrane detachment from the underlying cytoskeleton affects protein organization. It has been long known that a downstream consequence of IgE-FcεRI activation is a dramatic reorganization of the cytoskeleton into large lamellar ruffles [93]. Further, membrane interactions with the cytoskeleton have been implicated in the stabilization of crosslinked receptor complexes and with functional roles in receptor activity and serotonin secretion [94]. Support for this comes from the recent finding that multivalent antigen stimulation induces the recruitment of actin binding proteins to sites of receptor crosslinking [95]. Additionally, actin has been implicated in limiting IgE-FcεRI diffusion, as well as receptor-antigen immobilization and receptor clustering dynamics [96].

Open Questions

While these results have suggested unique hypotheses to describe the spatial organization of plasma membrane proteins during early signaling events, many questions remain unanswered and require further investigation. In particular, the physiological basis for self-clustered protein distributions at the plasma membrane has yet to be fully determined. Studies by Sengupta et al. [97] and others [88, 89, 98] find that virtually all proteins examined appear to be distributed in small ~20-50 nm clusters in resting cells. Often, these nano-cluster sizes are qualitatively compared to SPT 'hindered diffusion zone' domains as evidence to confirm the physical basis for autocorrelated protein

distributions; however, the two experimental methods represent very different physical descriptions of protein organization.

While nano-scale co-clustering of IgE-FcεRI and Syk may be expected [60, 99], the basis for receptor segregation away from Lyn [89] has not yet been determined, and it is somewhat surprising based on co-redistribution of IgE-FcεRI and Lyn detected in DRMs in vitro, as well as visualized by fluorescence microscopy in vivo [64, 65]. Evidence that the SH2 domain of Lyn binds phosphorylated tyrosine residues of the β subunit of IgE-FcεRI [60, 61] suggests a co-redistribution of Lyn with IgE-FcεRI, independent of whether initial receptor phosphorylation occurs within or outside of ordered membrane domains. In the same vein, the basis for LAT segregation into distinct microdomains that exclude Syk is still unclear [89]. Thus far, it has not been definitively demonstrated that interactions between IgE-FcεRI and Lyn are due either preferentially, or in whole, to protein-protein interactions or ordered microdomains. One possible strategy for uncoupling these two models would be a quantitative analysis of Lyn partitioning, as well as other signaling proteins, into crosslinked IgE-FcεRI domains when 1) ordered microdomains are perturbed with MβCD or 2) Lyn activity is inhibited (preventing receptor phosphorylation and subsequent binding of Lyn to phosphorylated receptor residues).

While high resolution studies of lateral protein organization have suggested that cell surface proteins are clustered into spatially, and perhaps functionally, distinct microdomains, quantitative methods for extracting information about the physical properties and characteristics of these structures (for example, size and composition) has been lacking. This is partially due to popularized mis-interpretations of (current) statistical analysis

tools used to describe immuno-gold labeled protein distributions, as well as the inherent difficulty in extracting quantitative stoichiometries from gold labeling densities.

There are still many questions that need to be addressed: For example, do crosslinked receptors form stable signaling platforms, and if so, how does the size and composition of these domains change as a function of stimulation time? Further elucidation of the mechanism that drives the redistribution of signaling proteins at the plasma membrane during mast cell activation may provide insight into the physiological significance of nano-scale lateral membrane heterogeneity.

1.6 Scope of Thesis

As described in this dissertation, I used fluorescence and electron microscopy techniques to probe the functional heterogeneity of the plasma membrane in RBL-2H3 mast cells. An overarching theme throughout these studies is the ability of the plasma membrane to respond to changes in its environment at both the micro- and nano-scale. Chapter Two describes collaborative studies where we used patterned poly (acrylic acid) (PAA) polymer brushes to explore the effects of surface chemistry and topography on cell-surface interactions. Interestingly, we found that when patterned at sub-cellular dimensions, cell-repellent PAA brushes become adhesion-promoting surfaces that initiate fibronectin-mediated cellular responses. By modifying brush thickness, we found that PAA can be 'tuned' to promote cell adhesion without triggering non-specific cell-surface interactions. Further, we demonstrated the utility of patterned PAA arrays as a tool to study immune

cell signaling by modifying brushes with ligands that specifically engage IgE bound to its high affinity cell surface receptor, FcεRI.

Chapter Three describes a different collaboration where we used pair correlation function analysis to investigate the lateral heterogeneity of the plasma membrane in resting RBL-2H3 cells. Using a combination of SED and BSD-SEM, we visualized immuno-gold labeled proteins at the top surface of intact resting cells. Consistent with previous reports, we found that gold particles labeling cell surface proteins, as well as proteins randomly immobilized onto silicon surfaces, have significantly clustered distributions. By (1) comparing correlation functions for cell surface proteins of varying densities, (2) imaging proteins covalently conjugated to a silicon surface, and (3) measuring cross-correlations between two pools of functionally identical but distinctively labeled (with differently sized gold particles) proteins, we found that this apparent clustering can be accounted for by multiple gold particles binding to individual target proteins. After correcting for this artifact, we found that all membrane proteins and lipids examined have random distributions. In double label experiments, we found that IgE-FcεRI and Lyn are significantly cross-correlated. To investigate the physical basis for IgE-FcεRI/Lyn interactions we modulated cholesterol levels and find that constitutive co-clustering of IgE-FcεRI and Lyn is sensitive to, but not wholly dependent on cholesterol.

In Chapter Four, we monitored the distribution of gold-labeled IgE-FcεRI, Lyn, Syk, and LAT before and after stimulation with multivalent antigen at 37˚C, and we quantified particle distributions with the analytical tools developed in Chapter Three. We found that after stimulation, IgE-FcεRI, Lyn, Syk, and LAT rapidly redistribute into large, stable clusters that may

represent signaling platforms. While stimulated protein clusters decrease in size at long stimulation times, we found that protein density within clusters increases, suggesting that the composition of the membrane underlying the clustered proteins changes as a function of stimulation time. Contrary to previous studies, which have suggested a segregation of Lyn away from crosslinked IgE-FcεRI, our double label experiments show that Lyn rapidly associates with crosslinked IgE-FcεRI and remains co-clustered at long stimulation times. Additionally, we found that stimulation-dependent clustering of IgE-FcεRI and Lyn is sensitive to both cholesterol depletion and inhibition of Src family kinase activity, indicating that both lipid raft-mediated and protein-protein interactions contribute to early IgE-mediated signaling events. In Chapter Five, we provide a summary of our findings and present a framework to describe the physical basis for the protein reorganization that occurs as a result of IgE-FcεRI mediated signaling.

In Appendix A, we investigated whether the actin cytoskeleton plays a role in the redistribution of IgE-FcεRI and its associated signaling proteins. Double label SEM experiments revealed that actin rapidly co-redistributes with IgE-FcεRI after stimulation with multivalent antigen at 37° C. Further, we provided strong evidence for an actin-dependent redistribution of signaling proteins after receptor crosslinking, evidenced by the dramatic effects of cytoskeletal perturbations on protein cluster size and composition.

As described in Appendix B, we used trivalent Y-shaped DNA ligands to crosslink IgE-FcεRI in a spatially regulated manner, and immuno-gold labeled IgE-FcεRI was visualized by SED and BSD-SEM. In previous fluorescence microscopy studies using these ligands, receptor phosphorylation was 5-10 fold reduced after stimulation with the longest

ligand (Y46-DNP3-DNA, 13.5 nm spacer) compared to stimulation with the shortest ligand (Y16-DNP_3-DNA, 4.5 nm) [100]. In single label SEM experiments, we found that crosslinking of IgE-FcεRI with Y46-DNP_3-DNA results in clusters that are dramatically reduced in size and composition (~80%), compared to crosslinking with Y16-DNP_3-DNA. Despite these dramatic nano-scale clustering differences, we find that both Y46-DNP_3-DNA and Y16-DNP_3-DNA induce nearly indistinguishable micron-scale clustering at the plasma membrane as visualized by fluorescence microscopy.

Collectively, our experimental findings have demonstrated that stimulation-induced redistribution of crosslinked IgE-FcεRI and associated signaling proteins results from many different contributions, and they provide new insight to describe the mechanism by which receptor organization is coupled to the recruitment of important signaling proteins during early cell signaling events.

REFERENCES

1. Pfeffer, W., *Osmotische Untersuchungen*. 1877, Leipzig: Engelmann.
2. Overton, E., *Studien uber die Narkose, zugleich ein Beitrag zur allgemeinen Parmakologie.* 1901, Jena: Gustav Fischer.
3. Overton, E., *Ueber die allgemeinen osmotischen Eigenschaften der Zelle, ihre vermuthlichen ursachen und ihre bedeutung fur die physiologie*. Vol. XLIV. 1899, Zurich: Verteljahr-shr. d. Naturf.-Ges. 88-135.
4. Nathansohn, A., *Ueber die Regulation der Aufnahme anorganischer Salze durch die KnoUen von Dahlia.* Jahrb. wiss. Bot., 1904. **39**: p. 697-644.
5. Gorter, E.a.G., F, *On bimolecular layers of lipoids on the chromocytes of the blood.* J Exp Med, 1925. **41**: p. 439.
6. Danielli, J.F.a.D., H, *A contribution to the theory of permeability of thin films.* Journal of Cellular and Comparative Physiology, 1935. **5**(4): p. 495-508.
7. Singer, S.J. and G.L. Nicolson, *The fluid mosaic model of the structure of cell membranes.* Science, 1972. **175**(23): p. 720-31.
8. Simson, R., E.D. Sheets, and K. Jacobson, *Detection of temporary lateral confinement of membrane proteins using single-particle tracking analysis.* Biophys J, 1995. **69**(3): p. 989-93.
9. Sheets, E.D., et al., *Transient confinement of a glycosylphosphatidylinositol-anchored protein in the plasma membrane.* Biochemistry, 1997. **36**(41): p. 12449-58.

10. Simson, R., et al., *Structural mosaicism on the submicron scale in the plasma membrane.* Biophys J, 1998. **74**(1): p. 297-308.
11. Kusumi, A. and Y. Sako, *Cell surface organization by the membrane skeleton.* Curr Opin Cell Biol, 1996. **8**(4): p. 566-74.
12. Sako, Y. and A. Kusumi, *Compartmentalized structure of the plasma membrane for receptor movements as revealed by a nanometer-level motion analysis.* J Cell Biol, 1994. **125**(6): p. 1251-64.
13. Sako, Y. and A. Kusumi, *Barriers for lateral diffusion of transferrin receptor in the plasma membrane as characterized by receptor dragging by laser tweezers: fence versus tether.* J Cell Biol, 1995. **129**(6): p. 1559-74.
14. Kusumi, A., Y. Sako, and M. Yamamoto, *Confined lateral diffusion of membrane receptors as studied by single particle tracking (nanovid microscopy). Effects of calcium-induced differentiation in cultured epithelial cells.* Biophys J, 1993. **65**(5): p. 2021-40.
15. Dietrich, C., et al., *Relationship of lipid rafts to transient confinement zones detected by single particle tracking.* Biophys J, 2002. **82**(1 Pt 1): p. 274-84.
16. Fujiwara, T., et al., *Phospholipids undergo hop diffusion in compartmentalized cell membrane.* J Cell Biol, 2002. **157**(6): p. 1071-81.
17. Simons, K. and E. Ikonen, *Functional rafts in cell membranes.* Nature, 1997. **387**(6633): p. 569-72.
18. Leathes, J.B., *On the role of fats in vital phenomena.* Lancet, 1925. **205208**(5304): p. 853-856.

19. Elliott, R., I. Szleifer, and M. Schick, *Phase diagram of a ternary mixture of cholesterol and saturated and unsaturated lipids calculated from a microscopic model.* Phys Rev Lett, 2006. **96**(9): p. 098101.

20. McConnell, H.M. and A. Radhakrishnan, *Condensed complexes of cholesterol and phospholipids.* Biochim Biophys Acta, 2003. **1610**(2): p. 159-73.

21. Huang, J. and G.W. Feigenson, *A microscopic interaction model of maximum solubility of cholesterol in lipid bilayers.* Biophys J, 1999. **76**(4): p. 2142-57.

22. Recktenwald, D.J. and H.M. McConnell, *Phase equilibria in binary mixtures of phosphatidylcholine and cholesterol.* Biochemistry, 1981. **20**(15): p. 4505-10.

23. Dietrich, C., et al., *Lipid rafts reconstituted in model membranes.* Biophys J, 2001. **80**(3): p. 1417-28.

24. Hammond, A.T., et al., *Crosslinking a lipid raft component triggers liquid ordered-liquid disordered phase separation in model plasma membranes.* Proc Natl Acad Sci U S A, 2005. **102**(18): p. 6320-5.

25. Harder, T. and K. Simons, *Clusters of glycolipid and glycosylphosphatidylinositol-anchored proteins in lymphoid cells: accumulation of actin regulated by local tyrosine phosphorylation.* Eur J Immunol, 1999. **29**(2): p. 556-62.

26. Silvius, J.R., *Fluorescence energy transfer reveals microdomain formation at physiological temperatures in lipid mixtures modeling the outer leaflet of the plasma membrane.* Biophys J, 2003. **85**(2): p. 1034-45.

27. Sengupta, P., D. Holowka, and B. Baird, *Fluorescence resonance energy transfer between lipid probes detects nanoscopic heterogeneity in the plasma membrane of live cells.* Biophys J, 2007. **92**(10): p. 3564-74.

28. Veatch, S.L., et al., *Critical fluctuations in plasma membrane vesicles.* ACS Chem Biol, 2008. **3**(5): p. 287-93.

29. Nicolau, D.V., Jr., et al., *Identifying optimal lipid raft characteristics required to promote nanoscale protein-protein interactions on the plasma membrane.* Mol Cell Biol, 2006. **26**(1): p. 313-23.

30. Simons, K. and G. van Meer, *Lipid sorting in epithelial cells.* Biochemistry, 1988. **27**(17): p. 6197-202.

31. Nichols, B., *Cell biology: without a raft.* Nature, 2005. **436**(7051): p. 638-9.

32. Schutz, G.J., et al., *Single molecule microscopy of biomembranes (review).* Mol Membr Biol, 2000. **17**(1): p. 17-29.

33. Sharma, P., et al., *Nanoscale organization of multiple GPI-anchored proteins in living cell membranes.* Cell, 2004. **116**(4): p. 577-89.

34. Glebov, O.O. and B.J. Nichols, *Lipid raft proteins have a random distribution during localized activation of the T-cell receptor.* Nat Cell Biol, 2004. **6**(3): p. 238-43.

35. Kenworthy, A.K. and M. Edidin, *Distribution of a glycosylphosphatidylinositol-anchored protein at the apical surface of MDCK cells examined at a resolution of <100 A using imaging fluorescence resonance energy transfer.* J Cell Biol, 1998. **142**(1): p. 69-84.

36. Vrljic, M., et al., *Translational diffusion of individual class II MHC membrane proteins in cells.* Biophys J, 2002. **83**(5): p. 2681-92.

37. Oliver, J.M., et al., *Membrane receptor mapping: the membrane topography of Fc(epsilon)RI signaling.* Subcell Biochem, 2004. **37**: p. 3-34.

38. Edidin, M., S.C. Kuo, and M.P. Sheetz, *Lateral movements of membrane glycoproteins restricted by dynamic cytoplasmic barriers.* Science, 1991. **254**(5036): p. 1379-82.

39. Edidin, M., M.C. Zuniga, and M.P. Sheetz, *Truncation mutants define and locate cytoplasmic barriers to lateral mobility of membrane glycoproteins.* Proc Natl Acad Sci U S A, 1994. **91**(8): p. 3378-82.

40. Murase, K., et al., *Ultrafine membrane compartments for molecular diffusion as revealed by single molecule techniques.* Biophys J, 2004. **86**(6): p. 4075-93.

41. Suzuki, K. and M.P. Sheetz, *Binding of cross-linked glycosylphosphatidylinositol-anchored proteins to discrete actin-associated sites and cholesterol-dependent domains.* Biophys J, 2001. **81**(4): p. 2181-9.

42. Subczynski, W.K. and A. Kusumi, *Dynamics of raft molecules in the cell and artificial membranes: approaches by pulse EPR spin labeling and single molecule optical microscopy.* Biochim Biophys Acta, 2003. **1610**(2): p. 231-43.

43. Kroczek, R.A., et al., *Thy-1 functions as a signal transduction molecule in T lymphocytes and transfected B lymphocytes.* Nature, 1986. **322**(6075): p. 181-4.

44. Heneberg, P., et al., *Topography of plasma membrane microdomains and its consequences for mast cell signaling.* Eur J Immunol, 2006. **36**(10): p. 2795-806.

45. Harder, T., et al., *Lipid domain structure of the plasma membrane revealed by patching of membrane components.* J Cell Biol, 1998. **141**(4): p. 929-42.

46. Suzuki, K.G., et al., *GPI-anchored receptor clusters transiently recruit Lyn and G alpha for temporary cluster immobilization and Lyn activation: single-molecule tracking study 1.* J Cell Biol, 2007. **177**(4): p. 717-30.

47. Bagatolli, L.A. and E. Gratton, *Two photon fluorescence microscopy of coexisting lipid domains in giant unilamellar vesicles of binary phospholipid mixtures.* Biophys J, 2000. **78**(1): p. 290-305.

48. Viola, A., et al., *T lymphocyte costimulation mediated by reorganization of membrane microdomains.* Science, 1999. **283**(5402): p. 680-2.

49. Zhang, W., R.P. Trible, and L.E. Samelson, *LAT palmitoylation: its essential role in membrane microdomain targeting and tyrosine phosphorylation during T cell activation.* Immunity, 1998. **9**(2): p. 239-46.

50. Kabouridis, P.S., A.I. Magee, and S.C. Ley, *S-acylation of LCK protein tyrosine kinase is essential for its signalling function in T lymphocytes.* EMBO J, 1997. **16**(16): p. 4983-98.

51. Montixi, C., et al., *Engagement of T cell receptor triggers its recruitment to low-density detergent-insoluble membrane domains.* EMBO J, 1998. **17**(18): p. 5334-48.

52. Janes, P.W., S.C. Ley, and A.I. Magee, *Aggregation of lipid rafts accompanies signaling via the T cell antigen receptor.* J Cell Biol, 1999. **147**(2): p. 447-61.

53. Kabouridis, P.S., et al., *Cholesterol depletion disrupts lipid rafts and modulates the activity of multiple signaling pathways in T lymphocytes.* Eur J Immunol, 2000. **30**(3): p. 954-63.

54. Yu, C.C., et al., *Lupus-like kidney disease in mice deficient in the Src family tyrosine kinases Lyn and Fyn.* Curr Biol, 2001. **11**(1): p. 34-8.

55. Verhagen, A.M., et al., *A kinase-dead allele of Lyn attenuates autoimmune disease normally associated with Lyn deficiency.* J Immunol, 2009. **182**(4): p. 2020-9.

56. Hibbs, M.L., et al., *Multiple defects in the immune system of Lyn-deficient mice, culminating in autoimmune disease.* Cell, 1995. **83**(2): p. 301-11.

57. Cheng, P.C., et al., *A role for lipid rafts in B cell antigen receptor signaling and antigen targeting.* J Exp Med, 1999. **190**(11): p. 1549-60.

58. Aman, M.J. and K.S. Ravichandran, *A requirement for lipid rafts in B cell receptor induced Ca(2+) flux.* Curr Biol, 2000. **10**(7): p. 393-6.

59. Flores-Borja, F., et al., *Decreased Lyn expression and translocation to lipid raft signaling domains in B lymphocytes from patients with systemic lupus erythematosus.* Arthritis Rheum, 2005. **52**(12): p. 3955-65.

60. Stauffer, T.P. and T. Meyer, *Compartmentalized IgE receptor-mediated signal transduction in living cells.* J Cell Biol, 1997. **139**(6): p. 1447-54.

61. Sada, K., J. Zhang, and R.P. Siraganian, *SH2 domain-mediated targeting, but not localization, of Syk in the plasma membrane is critical for FcepsilonRI signaling.* Blood, 2001. **97**(5): p. 1352-9.

62. Sullivan, A.L., P.M. Grimley, and H. Metzger, *Electron microscopic localization of immunoglobulin E on the surface membrane of human basophils.* J Exp Med, 1971. **134**(6): p. 1403-16.

63. Carson, D.A. and H. Metzger, *Interaction of IgE with rat basophilic leukemia cells. IV. Antibody-induced redistribution of IgE receptors.* J Immunol, 1974. **113**(4): p. 1271-7.

64. Sheets, E.D., D. Holowka, and B. Baird, *Critical role for cholesterol in Lyn-mediated tyrosine phosphorylation of FcepsilonRI and their association with detergent-resistant membranes.* J Cell Biol, 1999. **145**(4): p. 877-87.

65. Holowka, D., E.D. Sheets, and B. Baird, *Interactions between Fc(epsilon)RI and lipid raft components are regulated by the actin cytoskeleton.* J Cell Sci, 2000. **113 (Pt 6)**: p. 1009-19.

66. Kovarova, M., et al., *Structure-function analysis of Lyn kinase association with lipid rafts and initiation of early signaling events after Fcepsilon receptor I aggregation.* Mol Cell Biol, 2001. **21**(24): p. 8318-28.

67. Wu, M., et al., *Visualization of plasma membrane compartmentalization with patterned lipid bilayers.* Proc Natl Acad Sci U S A, 2004. **101**(38): p. 13798-803.

68. Larson, D.R., et al., *Temporally resolved interactions between antigen-stimulated IgE receptors and Lyn kinase on living cells.* J Cell Biol, 2005. **171**(3): p. 527-36.

69. Prieschl, E.E., et al., *Glycosphingolipid-induced relocation of Lyn and Syk into detergent-resistant membranes results in mast cell activation.* J Immunol, 2000. **164**(10): p. 5389-97.

70. Stefanova, I., et al., *GPI-anchored cell-surface molecules complexed to protein tyrosine kinases.* Science, 1991. **254**(5034): p. 1016-9.

71. Draberova, L. and P. Draber, *Thy-1 glycoprotein and src-like protein-tyrosine kinase p53/p56lyn are associated in large detergent-resistant complexes in rat basophilic leukemia cells.* Proc Natl Acad Sci U S A, 1993. **90**(8): p. 3611-5.

72. Zhang, W., et al., *LAT: the ZAP-70 tyrosine kinase substrate that links T cell receptor to cellular activation.* Cell, 1998. **92**(1): p. 83-92.

73. Field, K.A., D. Holowka, and B. Baird, *Fc epsilon RI-mediated recruitment of p53/56lyn to detergent-resistant membrane domains accompanies cellular signaling.* Proc Natl Acad Sci U S A, 1995. **92**(20): p. 9201-5.

74. Field, K.A., D. Holowka, and B. Baird, *Compartmentalized activation of the high affinity immunoglobulin E receptor within membrane domains.* J Biol Chem, 1997. **272**(7): p. 4276-80.

75. Young, R.M., D. Holowka, and B. Baird, *A lipid raft environment enhances Lyn kinase activity by protecting the active site tyrosine from dephosphorylation.* J Biol Chem, 2003. **278**(23): p. 20746-52.

76. Young, R.M., et al., *Reconstitution of regulated phosphorylation of FcepsilonRI by a lipid raft-excluded protein-tyrosine phosphatase.* J Biol Chem, 2005. **280**(2): p. 1230-5.

77. Yamashita, T., S.Y. Mao, and H. Metzger, *Aggregation of the high-affinity IgE receptor and enhanced activity of p53/56lyn protein-tyrosine kinase.* Proc Natl Acad Sci U S A, 1994. **91**(23): p. 11251-5.

78. Pribluda, V.S., C. Pribluda, and H. Metzger, *Transphosphorylation as the mechanism by which the high-affinity receptor for IgE is phosphorylated upon aggregation.* Proc Natl Acad Sci U S A, 1994. **91**(23): p. 11246-50.

79. Vonakis, B.M., et al., *The unique domain as the site on Lyn kinase for its constitutive association with the high affinity receptor for IgE.* J Biol Chem, 1997. **272**(38): p. 24072-80.

80. Hutchcroft, J.E., M.L. Harrison, and R.L. Geahlen, *Association of the 72-kDa protein-tyrosine kinase PTK72 with the B cell antigen receptor.* J Biol Chem, 1992. **267**(12): p. 8613-9.

81. Burkhardt, A.L., et al., *Anti-immunoglobulin stimulation of B lymphocytes activates src-related protein-tyrosine kinases.* Proc Natl Acad Sci U S A, 1991. **88**(16): p. 7410-4.

82. Tseng, J., et al., *The B cell antigen receptor complex: mechanisms and implications of tyrosine kinase activation.* Immunol Res, 1994. **13**(4): p. 299-310.

83. Vonakis, B.M., et al., *Interaction between the unphosphorylated receptor with high affinity for IgE and Lyn kinase.* J Biol Chem, 2001. **276**(2): p. 1041-50.

84. de Harven, E., R. Leung, and H. Christensen, *A novel approach for scanning electron microscopy of colloidal gold-labeled cell surfaces.* J Cell Biol, 1984. **99**(1 Pt 1): p. 53-7.

85. Stump, R.F., et al., *Mapping gold-labeled IgE receptors on mast cells by scanning electron microscopy: receptor distributions revealed by silver enhancement, backscattered electron imaging, and digital image analysis.* J Histochem Cytochem, 1988. **36**(5): p. 493-502.

86. Johkura, K., et al., *Spatial distribution of cell adhesion molecules on the peritoneal surface in the cecal perforation-induced peritonitis.* Anat Rec, 2001. **264**(2): p. 219-27.

87. Sanan, D.A. and R.G. Anderson, *Simultaneous visualization of LDL receptor distribution and clathrin lattices on membranes torn from the upper surface of cultured cells.* J Histochem Cytochem, 1991. **39**(8): p. 1017-24.

88. Prior, I.A., et al., *Direct visualization of Ras proteins in spatially distinct cell surface microdomains.* J Cell Biol, 2003. **160**(2): p. 165-70.

89. Wilson, B.S., J.R. Pfeiffer, and J.M. Oliver, *Observing FcepsilonRI signaling from the inside of the mast cell membrane.* J Cell Biol, 2000. **149**(5): p. 1131-42.

90. Wilson, B.S., et al., *High resolution mapping of mast cell membranes reveals primary and secondary domains of Fc(epsilon)RI and LAT.* J Cell Biol, 2001. **154**(3): p. 645-58.

91. Yang, S., et al., *Mapping ErbB receptors on breast cancer cell membranes during signal transduction.* J Cell Sci, 2007. **120**(Pt 16): p. 2763-73.

92. Surviladze, Z., et al., *Differential sensitivity to acute cholesterol lowering of activation mediated via the high-affinity IgE receptor and Thy-1 glycoprotein.* Eur J Immunol, 2001. **31**(1): p. 1-10.

93. Oliver, J.M., et al., *Signal transduction and cellular response in RBL-2H3 mast cells.* Prog Allergy, 1988. **42**: p. 185-245.

94. Seagrave, J., et al., *Relationship of IgE receptor topography to secretion in RBL-2H3 mast cells.* J Cell Physiol, 1991. **148**(1): p. 139-51.

95. Torres, A.J., et al., *Focal adhesion proteins connect IgE receptors to the cytoskeleton as revealed by micropatterned ligand arrays.* Proc Natl Acad Sci U S A, 2008. **105**(45): p. 17238-44.

96. Andrews, N.L., et al., *Actin restricts FcepsilonRI diffusion and facilitates antigen-induced receptor immobilization.* Nat Cell Biol, 2008. **10**(8): p. 955-63.

97. Sengupta, P., *Lateral organization of proteins and lipids in the plasma membrane of RBL-2H3 mast cells and phase separated giant plasma membrane vesicles: implications for plasma membrane architecture*, in *Department of Chemistry and Chemical Biology*. 2007, Cornell University: Ithaca. p. 156.

98. Plowman, S.J., et al., *H-ras, K-ras, and inner plasma membrane raft proteins operate in nanoclusters with differential dependence on the actin cytoskeleton.* Proc Natl Acad Sci U S A, 2005. **102**(43): p. 15500-5.

99. Kihara, H. and R.P. Siraganian, *Src homology 2 domains of Syk and Lyn bind to tyrosine-phosphorylated subunits of the high affinity IgE receptor.* J Biol Chem, 1994. **269**(35): p. 22427-32.

100. Sil, D., et al., *Trivalent ligands with rigid DNA spacers reveal structural requirements for IgE receptor signaling in RBL mast cells.* ACS Chem Biol, 2007. **2**(10): p. 674-84.

CHAPTER TWO

Investigating Cellular Responses to Patterned Poly (Acrylic Acid) Polymer Brush Surfaces *

Summary

We use patterned poly (acrylic acid) (PAA) polymer brushes to explore the effects of surface chemistry and topography on cell-surface interactions. Most past studies of surface topography effects on cell adhesion have relied on patterned feature sizes that are larger than the dimensions of a cell. Here we report cell adhesion studies for RBL-2H3 mast cells incubated on PAA brush surfaces patterned with a variety of different feature sizes and brush thicknesses. Interestingly, we find that when patterned at sub-cellular dimensions, cell-repellent PAA brushes become adhesion-promoting surfaces that initiate fibronectin-mediated cellular responses. Integrin engagement over PAA brush regions causes a dramatic reorganization of the plasma membrane involving actin polymerization at the cell-surface interface. By modifying brush thickness, we find that PAA can be 'tuned' to promote cell adhesion without triggering non-specific membrane accumulation over patterned brush regions. We demonstrate the utility of patterned PAA arrays as a tool to study mast cell signaling by modifying brushes with ligands that specifically engage IgE receptor complexes on cellular surfaces.

---

* This work was carried out in collaboration with Rong Dong, who contributed to the synthesis and fabrication of the patterned PAA and PAA-DNP arrays.

2.1 INTRODUCTION

At the cell level in living systems, interactions between the cell membrane and the extracellular matrix (ECM) are important for cell adhesion, motility, structural support, cell growth and regulation, tissue segregation, and many other cellular responses. In the fields of biomedical implantation, tissue engineering, and cell-based sensors, the successful incorporation of materials and devices into biological systems requires a thorough understanding of cellular response to a substrate's surface chemistry and topography. Thus, systematic assessment of how cells interact and respond to their environment at the nano- and micro-scopic level is key to tuning the bio-compatibility of a material's surface.

One technique commonly used to promote favorable cell-surface interactions is the immobilization of adhesion-promoting biomolecules, such as fibronectin, onto bio-incompatible surfaces via adsorption or covalent modification. Additionally, cell adhesion and behavior can be modified by the chemical composition and/or topography of the substrate. Recently, polymer brushes have attracted considerable attention as bio-functional surfaces due to their versatile properties. Compared to self-assembled monolayers (SAMs), polymer brushes provide a higher density of functional groups and can be used to immobilize multiple layers of proteins. Due to the thickly branched ("brush-like") structure of polymer brushes in aqueous solution, hydrophilic polymer brushes may also prove superior to SAMs for mimicking the in vivo extracellular matrix (ECM) environment.

Previous studies investigating surface topography effects on cell adhesion have typically utilized patterned feature sizes that are larger than the dimensions of a cell. Here we report cell adhesion studies for RBL mast cells incubated on poly (acrylic acid) (PAA) polymer brush surfaces patterned with a variety of different feature sizes. Further, we explore the cellular processes and biological mechanisms that drive interactions at the cell-surface interface. Interestingly, we find that when patterned at sub-cellular dimensions, cell-repellent PAA brushes become adhesion-promoting surfaces that initiate fibronectin-mediated cellular responses. By adjusting polymer brush thickness and patterned feature sizes, we find that PAA brushes can be 'tuned' to become adhesion-promoting surfaces, which do not accumulate membrane. Lastly, we demonstrate that patterned PAA arrays can be covalently modified to study mast cell signaling, by synthesizing PAA-DNP arrays that specifically crosslink IgE bound to its high affinity cell surface recepter FcεRI.

2.2 MATERIALS and METHODS

Materials:

Allyl 2-bromo-2-methylpropionate, chlorodimethylhydrosilane, Pt on activated carbon (10 wt %), triethylamine, CuBr, $CuBr_2$, 2,2′-bipyridine, sodium acrylate, diisoproplycarbodiimide (DIPC), bovine fibronectin, cytochalasin D, and all solvents used were purchased from Sigma (St. Louis, MO). All chemicals were used without further purification. Distilled deionized water and high-purity nitrogen gas (99.99 %, Airgas) were used throughout. Silicon wafers covered with native silicon oxide layer were

purchased from Montco Silicon Technologies, Inc. (Spring City, PA). Surface initiator for silica substrates was synthesized and immobilized on substrates as described below. 4-(dimethylamino)pyridinium-4-toluenesulfonate (DPTS) was synthesized according to a literature procedure [1]. A488-IgE was prepared by modification of purified mouse monoclonal anti-2,4-dinitrophenyl (DNP) IgE with Alexa Fluor 488 (Invitrogen Corp.) as previously described [2]. Alexa Fluor 488 cholera toxin subunit B (A488-CTxB), 1,1'-dihexadecyl-3,3,3',3'-tetramethylindocarbocyanine perchlorate ($DiIC_{16}$), Texas red dipalmitoyl-phosphatidylethanolamine (TR-DPPE), and Alexa Fluor 555 (A555)-conjugated goat anti-mouse pAb were purchased from Invitrogen Corp. (Eugene, OR). Monoclonal anti-fibronectin was purchased from Abcam (Cambridge, MA), and RGD peptides were purchased from Calbiochem (Gibbstown, NJ).

Patterning and Synthesis of PAA Brushes on Silicon Surfaces:

PAA brushes were patterned on silicon surfaces using a photolithography procedure, which is shown in Figure 2.1 and described elsewhere [3]. Briefly, a layer of lift-off resist 5A (LOR 5A) was spin-coated onto a silicon wafer prior to performing general photolithography. The solubility of LOR 5A in the photolithography developer solution allows good pattern transfer from photoresist to LOR 5A. Additionally, the insolubility of LOR 5A in organic solvents protects the underlying silica surface from unwanted chemical reactions. Surface initiator was attached to the exposed silicon surface, followed by surface-initiated polymerization of PAA and

subsequent removal of LOR 5A. Patterned PAA brushes were characterized using atomic force microscopy (AFM), and brush thicknesses were determined using AFM images and ellipsometry.

Synthesis of PAA-DNP Brushes:

Patterned PAA brush surfaces were prepared, as described previously [4], using slightly shorter polymerization times (~20 min). PAA brushes were prepared with different thicknesses (30 nm to 8 nm) by varying the monomer concentrations in the polymerization media (1.88 g sodium acrylate dissolved in 4, 5, and 6 mL of DI water). DNP-PEG was synthesized as previously reported [5] and attached to the patterned PAA brushes via hydroxyl moieties, as shown in Figure 2.2. Briefly, patterned PAA substrates were placed in a 25 mL Schlenk flask containing 75 mg DPTS. Following evacuation and back-filling with nitrogen three times, 4 mL anhydrous dichloromethane was added to the flask using a cannula. After the DPTS completely dissolved, 0.05 mL DNP-PEG and 0.05 mL DIPC was added to the reaction mixture, and the solution was kept overnight at room temperature. The patterned PAA-DNP substrates were then rinsed with water and isoproponal, blown dry, and stored in the dark prior to use for cell experiments. X-ray photoelectron spectroscopy (XPS) was used to confirm attachment of DNP to PAA by monitoring the appearance of a nitrogen peak in the XPS spectrum.

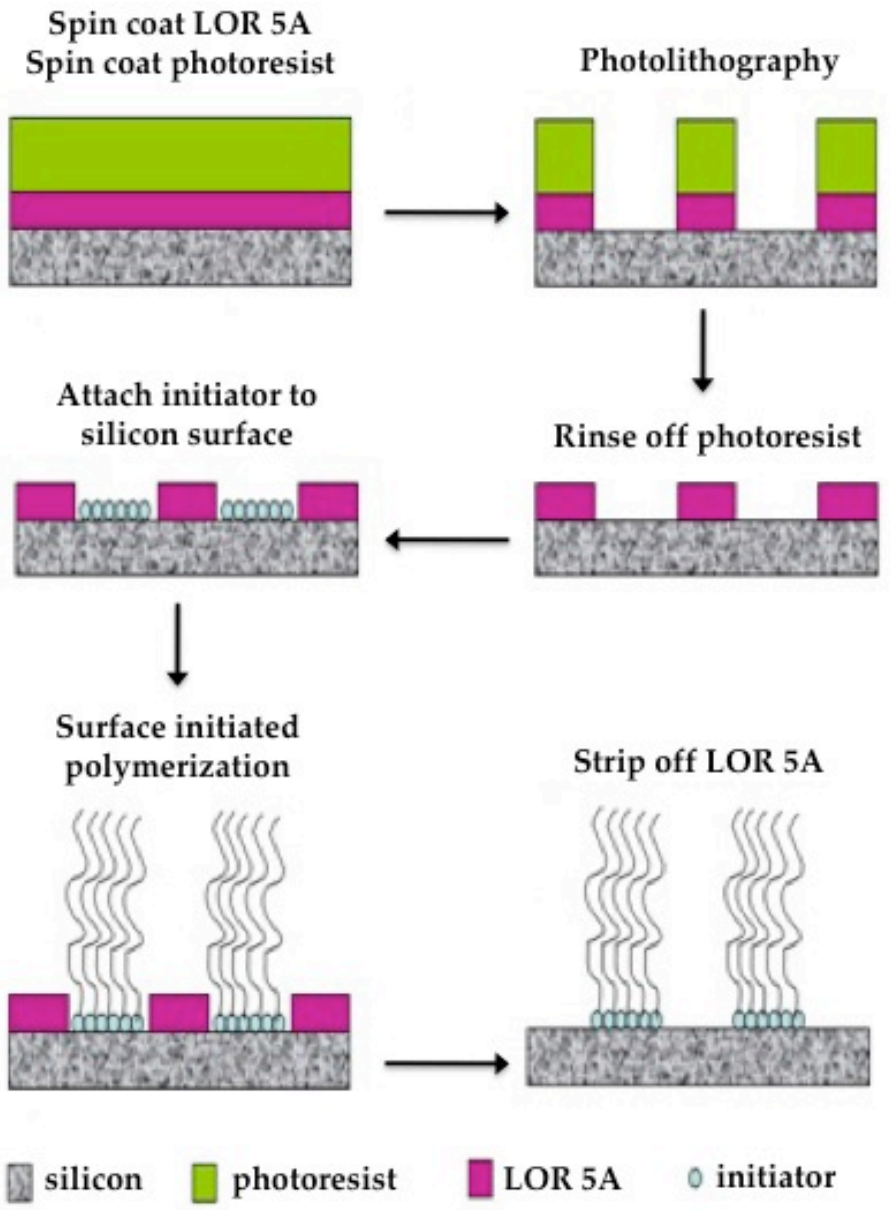

Figure 2.1: Patterning of PAA brushes. Lift-off resist and photo resist are sequentially deposited onto a silicon wafer. UV photolithography and subsequent resist development results in pattern transfer of micron-sized squares (or lines) into the lift-off resist. After attachment of initiator to the silicon surface and subsequent surface-initiated polymerization, the lift-off resist is removed.

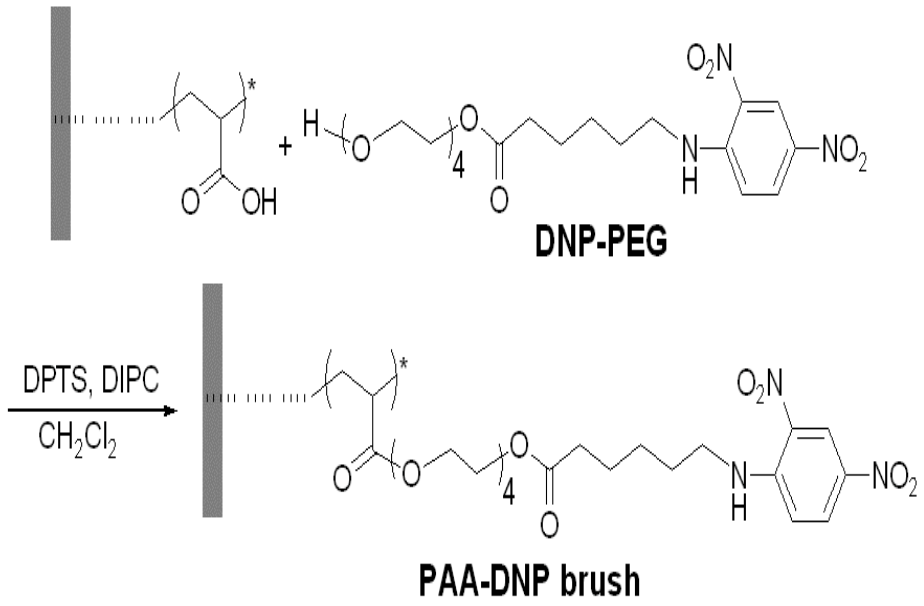

Figure 2.2: Modification of patterned PAA brushes with DNP. For detailed description see Materials and Methods.

RBL Cells Incubated on Patterned Brush Surfaces:

RBL-2H3 cells were maintained in tissue culture and harvested as previously described [6]. After 1 hr of sensitization with A488-IgE (1 μg/mL), cells were incubated on patterned PAA substrates (at a concentration of $0.5x10^6$ cells/mL) at either 37° C or room temperature for ~ 20 min. The substrates were then gently rinsed with buffered-saline solution (BSS:150 mM NaCl, 2.5 mM KCl, 12 mM $NaHCO_3$, 2 mM $MgCl_2$, 2 mM $CaCl_2$, 1 mg/mL bovine serum albumin, 1 mg/mL dextrose, pH 7.4) to remove unattached cells. The patterned substrates were then placed in MatTek dishes filled with BBS and imaged using confocal fluorescence microscopy. For most experiments, cells were visualized using fluorescently labeled A488-IgE. In some cases, cell membrane was labeled with either 2 μg/mL A555-CTxB, 10 μM TR-DPPE, or 10 μM $DiIC_{16}$, which typically labeled >80% of all cells. Membrane markers were added to suspended cells for 5 min at room temperature prior to cell incubation on patterned substrates. RBL cells expressing GFP-actin were produced using standard transfection protocols, as previously described [6].

Preparing Fibronectin-coated Surfaces:

Patterned substrates were incubated with 50 μg/mL bovine fibronectin for 1 hr at 37° C and then rinsed with BSS to remove unattached fibronectin. Fibronectin distributions were visualized using confocal microscopy after sequential immunofluorescence antibody labeling (anti-fibronectin mAb and A555-labeled goat anti-mouse pAb).

Treatment with Cytochalasin D and RGD Peptides:

RBL cells were treated with cytochalasin D before and after incubation on patterned PAA substrates. Prior to incubation, suspended cells were treated with 1 μg/mL cytochalasin D for 10 min at 37° C and then incubated on patterned substrates (in the presence of cytochalasin D) for 20 min at 37° C. In drug-washout experiments, the cytochalasin D-containing BSS solution was replaced with fresh BSS, and cell samples were re-incubated at 37° C for ~20 min. Identical concentrations and incubation times were used to treat cells with cytochalasin D post-incubation on the patterned PAA substrates. To inhibit integrin receptor binding, RBL cells were pre-treated with 1 μg/mL RGD peptides for ~30 min at 37° C prior to incubation on the patterned PAA substrates.

Confocal Microscopy:

Images of fluorescently labeled RBL cells on patterned PAA surfaces were obtained with a Leica TCS SP2 confocal microscope at room temperature. A 40x 0.8 NA long working distance water immersion lens was used for image acquisition. Reflectance images were acquired using a highly attenuated laser to visualize the polymer brush pattern borders. For visualization purposes, grids were generated using these reflectance images and superimposed, when necessary, over cellular fluorescence images to more clearly identify co-localization of cellular fluorescence with the underlying PAA brush patterns.

2.3 RESULTS

Patterned PAA Surfaces Promote Cell Adhesion.

As described above, we used photolithography to pattern 30 nm thick PAA brush surfaces with the following features: 100 μm wide lines, 20 μm wide lines, 10 μm squares, and 2 μm squares. The unpatterned surface between patterned PAA brush regions is bare silicon. RBL mast cells were labeled with A488-IgE that binds with high affinity (low dissociation constant) to cell surface FcεRI. Cells were incubated on each patterned surface for ~20 min at 37° C and visualized using confocal fluorescence microscopy, as shown by representative images in Figure 2.3.

Surfaces with 100% PAA brush coverage are extremely cell-repellent, and cell incubation on these surfaces results in nearly ~0% cell attachment (images not shown). Similarly, when cells are incubated on PAA surfaces patterned with 100 μm or 20 μm wide alternating lines of PAA and silicon, cells completely avoid PAA regions and preferentially adhere to bare silicon, as shown in Figure 2.3A-B (patterned PAA regions are shown in red). In both of these cases, patterned PAA feature dimensions are larger than the size of a cell (~20 μm) and most settling cells come into contact with only one surface (PAA) or the other (silicon).

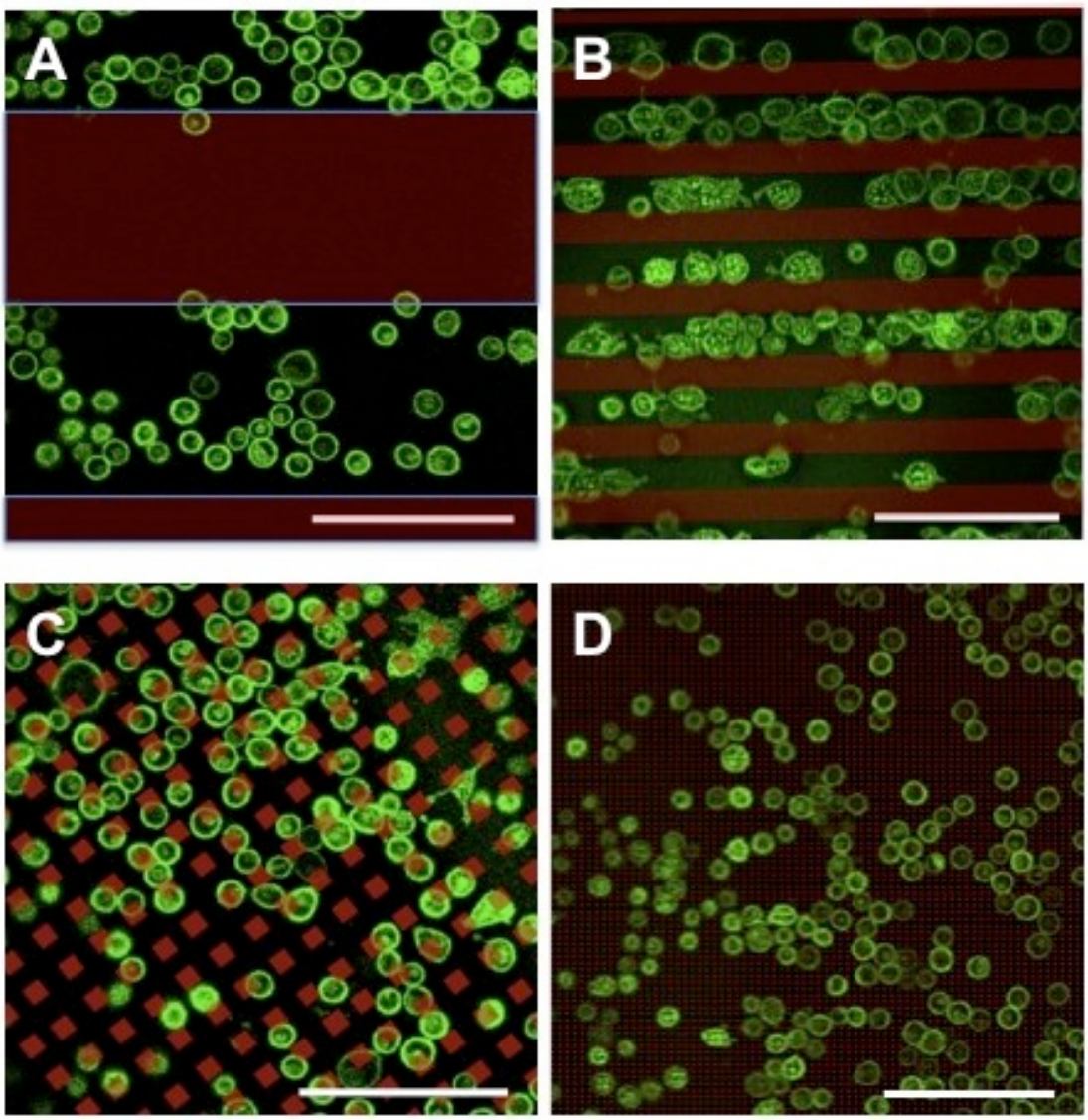

Figure 2.3: Cells attach and spread over small PAA brush features (<10 μm) while avoiding large feature sizes. RBL cells were labeled with A488-IgE and incubated for 20 min at 37˚ C on a variety of different PAA (~30 nm thick) surfaces. PAA regions are false-colored red. Cells completely avoid 100 μm wide (A) and 20 μm wide (B) lines of PAA. Cells mostly avoid 10 μm PAA squares (C), but partially adhere over PAA regions. Cells adhere and spread over surfaces patterned with 2 μm square PAA features (D). Scale bar is 100 μm.

However, when patterned surface features are smaller than the dimensions of a cell, settling cells come into contact with surfaces that posses mixed chemical and structural compositions (i.e. surface attachment requires interactions with both PAA and silicon). When cells are incubated on PAA surfaces patterned with 10 μm squares, the majority (~75%) of cells adhere to bare silicon. The remaining cells adhere mostly to silicon with partial membrane spreading over PAA brushes as illustrated in Figure 2.3C. However, cells incubated on PAA surfaces patterned with 2 μm squares necessarily come into contact with both silicon and PAA brushes and spread equally over patterned and unpatterned features, shown in Figure 2.3D.

Given this result, we quantified adhesion in Figure 2.4 by determining average cell densities on unpatterned silicon surfaces, unpatterned PAA (~30 nm thick) surfaces, and PAA (~30 nm thick) surfaces patterned with 2μm squares. More than 10 randomly selected regions on each substrate surface were collected for analysis. Compared to surfaces comprised of only silicon (~25 cells/100 μm^2), average cell densities on unpatterned PAA surfaces are dramatically reduced (~1 cells/100 μm^2). Interestingly, cell adhesion is significantly improved when cells are incubated on PAA surfaces patterned with 2 μm squares (~18 cells/100 μm^2), and the average cell density is very similar to the bare silicon surfaces.

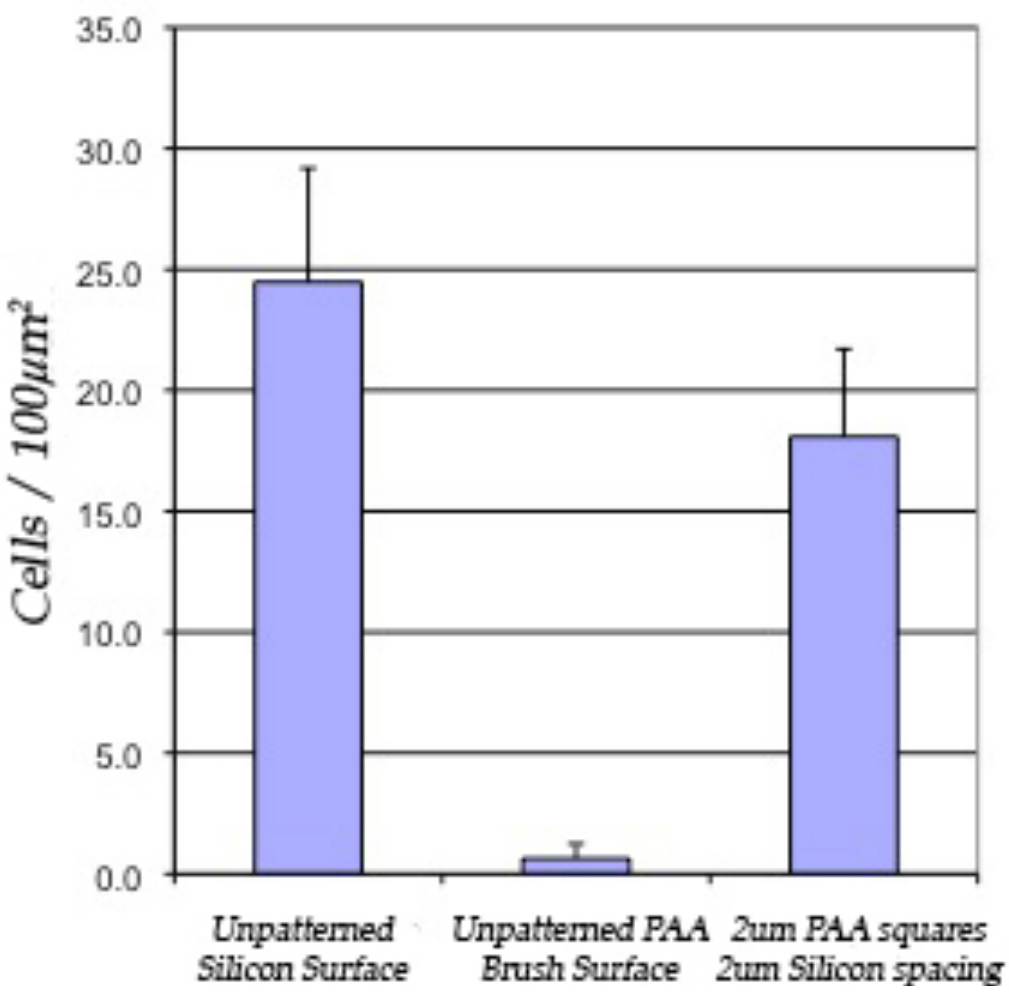

Figure 2.4: Patterning PAA brushes at small dimensions enhances cell adhesion. RBL cells were incubated for ~20 min at 37˚ C on unpatterned silicon surfaces, unpatterned PAA (~30 nm thick) surfaces, and PAA (~30 nm thick) surfaces patterned with 2 μm squares. While surfaces with 100% PAA brush coverage are extremely cell-repellent, cell adhesion on PAA brush surfaces patterned with 2 μm squares is comparable to adhesion on unpatterned silicon surfaces. Average cell densities on each surface were determined by quantifying attached cells in many images (n>10) over different experiments.

Membrane Accumulates over Patterned PAA Regions at 37˚ C.

Given the cell-repellent properties of PAA brushes, we unexpectedly found that the plasma membrane dramatically accumulated over 2 μm square PAA regions. In these experiments, cells were incubated on PAA (~30 nm thick) surfaces patterned with 2 μm squares for 20 min at 37˚ C, and membrane accumulation was visualized by concentration of different fluorescent membrane markers (A488-IgE, TR-DPPE and A488-CTxB) over PAA regions, shown in representative confocal fluorescence microscopy images (Figure 2.5A-C). The same membrane accumulation is observed when cells are incubated on PAA surfaces patterned with 2 μm and 5 μm wide lines (data not shown). However, cell densities on these surfaces were significantly lower after incubation on these "line-patterned" surfaces (>50% reduction) than those obtained on PAA surfaces patterned with 2 μm squares. One possible explanation is that patterned square features allow cell membrane contact with silicon surfaces around the periphery of PAA brush patterns, thereby compensating for unfavorable PAA brush-membrane interactions.

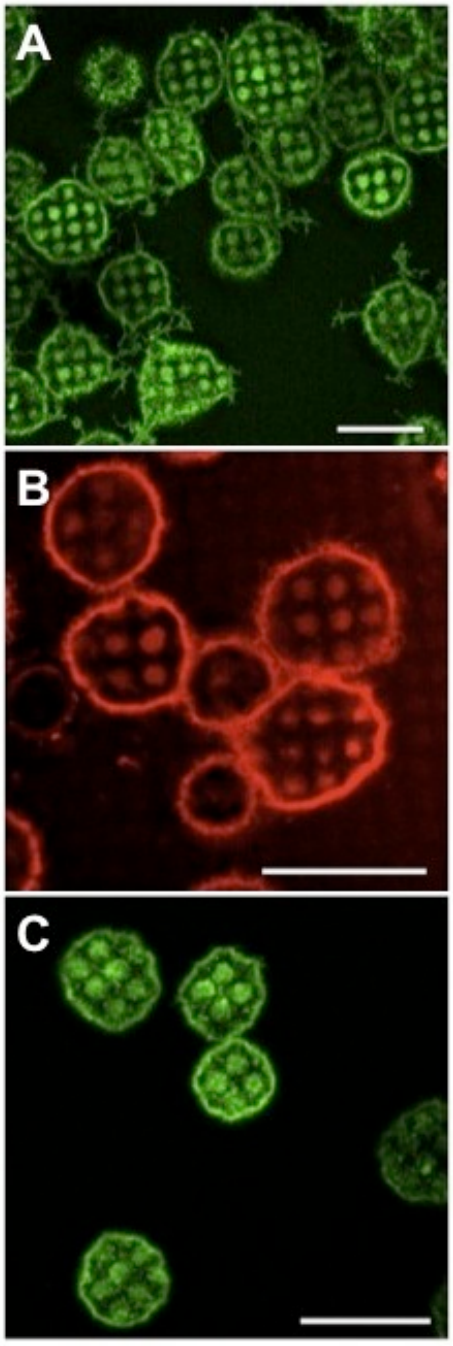

Figure 2.5: Cell membrane accumulates over PAA surfaces patterned with small (2 μm square) feature sizes. Confocal fluorescence micrographs show cells incubated on PAA surfaces (~30 nm thick) patterned with 2 μm square features. After 20 min of incubation at 37° C, membrane markers, including: A488-IgE (A), TR-DPPE (B), and A488-CTxB (C), accumulate over PAA regions. Scale bar is 20 μm.

We also investigated the effects of cell incubation temperature on membrane recruitment and accumulation over 2 μm square PAA (~30 nm thick) regions. Cells were labeled with A488-IgE and incubated at room temperature for 20 min, followed by an upward temperature shift to 37° C. When cells are incubated at room temperature, very few cells adhere to the patterned PAA surface (<10%). Of the cells that do adhere, membrane does not accumulate over patterned PAA regions, shown in Figure 2.6A. However, when the same sample of adherent cells is incubated at 37° C for 20 additional min, membrane accumulates over PAA patterns, as shown in Figure 2.6B. If, instead, cells are initially incubated at 37° C (allowing membrane to accumulate over PAA patterns) and then incubated at room temperature for 20 additional min, we observe sustained membrane accumulation over PAA patterns (data not shown).

Membrane Accumulation Requires Fibronectin-Integrin Binding.

Given the localized accumulation of plasma membrane over PAA brush regions, we investigated the mechanisms driving interactions at the membrane-brush interface. To identify whether PAA adsorbs, and thereby selectively concentrates, the ECM protein fibronectin, PAA surfaces (~30 nm thick) patterned with 2 μm square features were incubated with 50 μg/mL soluble fibronectin for 1 hr at 37° C. Fibronectin distributions were labeled by immunofluorescence and visualized by confocal fluorescence microscopy. As illustrated in Figure 2.7, fibronectin concentrates over patterned PAA regions, potentially due to the high surface area presented by the thick PAA brushes.

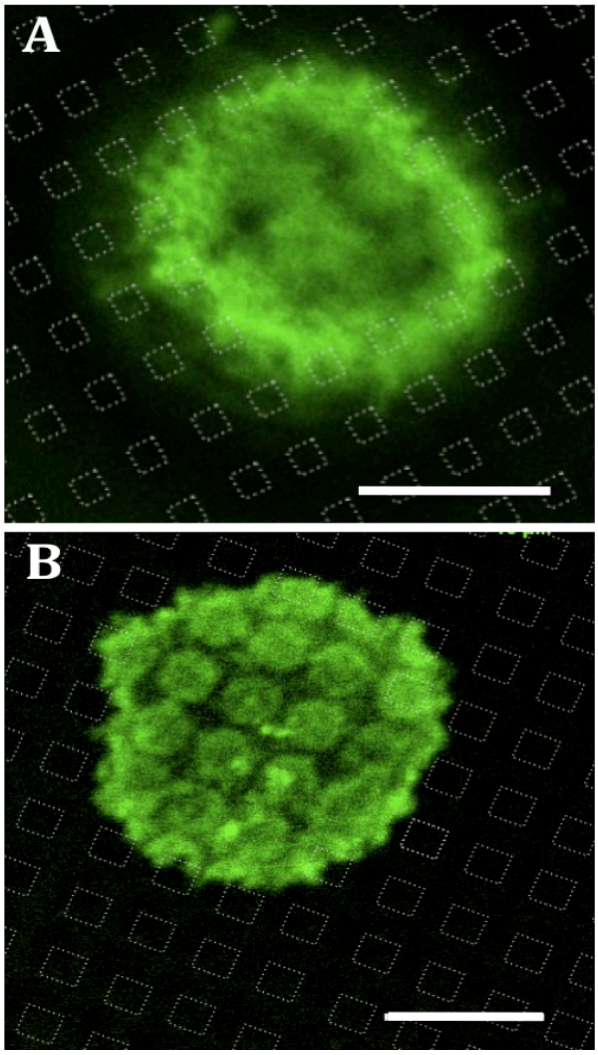

Figure 2.6: Membrane accumulates over PAA brushes at 37° C, but not at room temperature. Confocal fluorescence micrographs of cells labeled with A488-IgE and incubated on PAA (~30 nm thick) surfaces patterned with 2 μm square features. A) At room temperature, the cell membrane is homogeneously distributed over the patterned surface. B) When the same cells are re-incubated at 37° C for 20 min, membrane redistributes and accumulates over the brushes. White squares are superimposed over the fluorescence images to identify co-localization of accumulated plasma membrane with the underlying patterned PAA surface. Scale bar is 10 μm.

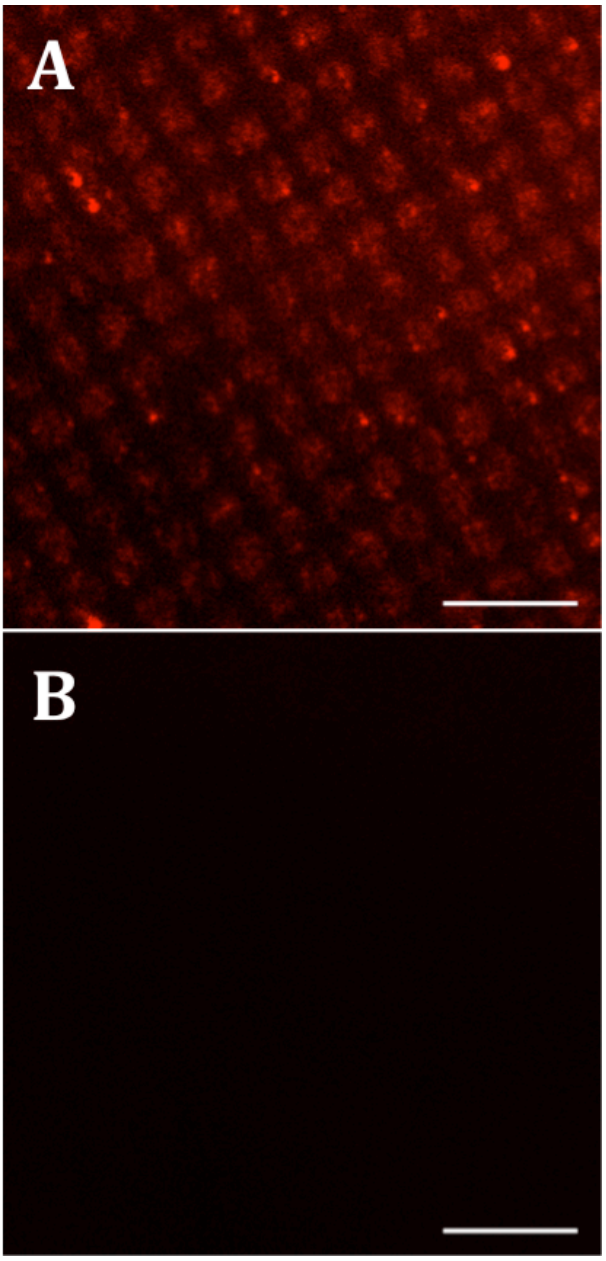

Figure 2.7: Fibronectin adsorbs to PAA brushes. Confocal fluorescence micrographs show PAA surfaces (~30 nm thick) patterned with 2 μm square features, which were incubated in the (A) presence (50 μg/mL) or (B) absence of soluble fibronectin. Fibronectin distributions were visualized by immunofluorescence labeling (anti-fibronectin mAb and A555-labeled goat anti-mouse pAb) and imaged under identical conditions. Scale bar is 10 μm.

This localized accumulation of fibronectin suggested that integrin receptors may be undergoing selective and localized ligation via fibronectin-enriched PAA brushes. To uncouple fibronectin-integrin interactions, cells were treated in the presence or absence of Arginine-Glycine-Aspartate (RGD)-containing peptides for 30 min at 37˚ C prior to incubation with PAA (~30 nm thick) surfaces patterned with 2 μm squares. Cells were labeled with A488-IgE and visualized using confocal fluorescence microscopy. In the absence of RGD peptides, membrane accumulated over PAA regions, as shown in Figure 2.8A. While pre-treatment with RGD peptides prevents the accumulation of membrane over PAA patterns, cells are able to attach, albeit less robustly, to PAA surfaces (Figure 2.8B).

The previous observation that fibronectin-integrin binding is required for membrane accumulation over PAA regions but not for cell attachment to the patterned surface (over both PAA and silicon regions) suggested that fibronectin adsorption to large 100 μm wide lines of PAA (previously demonstrated to be cell-repellent in Figure 2.3A) could facilitate cell adhesion. After confirming that fibronectin accumulates over 100 μm PAA regions by immunofluorescence (using the same fibronectin concentration as in Figure 2.7; data not shown), cells were incubated on the fibronectin-adsorbed surfaces for ~20 min at 37˚ C. Interestingly, cells still preferentially adhered to bare silicon, indicating that the presence of fibronectin alone is not sufficient to mitigate the cell-repellent nature of the PAA brushes (data not shown) and cell adherence requires some attachment to silicon. This is also consistent with the

observation that surfaces with 100% PAA brush coverage are extremely cell-repellent.

Collectively, these results suggest that localized membrane accumulation over PAA regions occurs through a two-step process where (1) cell adhesion only occurs if the cell-repellent patterned PAA features are small enough so that cells are exposed to sufficient silicon surface area and (2) attached cells secrete soluble fibronectin, which adsorbs to PAA regions and initiates fibronectin-integrin receptor engagement over PAA regions.

Cytoskeletal Contributions to Membrane Accumulation

As actin polymerization and cytoskeletal remodeling are hallmarks of integrin activation, we explored the role of actin in the recruitment of plasma membrane to PAA regions. GFP-actin constructs were introduced into cells by transient transfection, and cells expressing fluorescently labeled actin were incubated on patterned PAA surfaces (2 μm squares) at room temperature for 20 min followed by an upward temperature shift to 37° C for an additional 20 min. Actin distributions were visualized at both temperatures using confocal fluorescence microscopy. At room temperature, GFP-actin is uniformly distributed at the plasma membrane over both silicon and PAA regions (Figure 2.9A). However, there is a dramatic redistribution of GFP-actin to PAA regions when the incubation temperature is increased to 37° C (Figure 2.9B). This temperature-dependent reorganization of actin to PAA regions parallels that of the fluorescent membrane markers visualized in Figure 2.6.

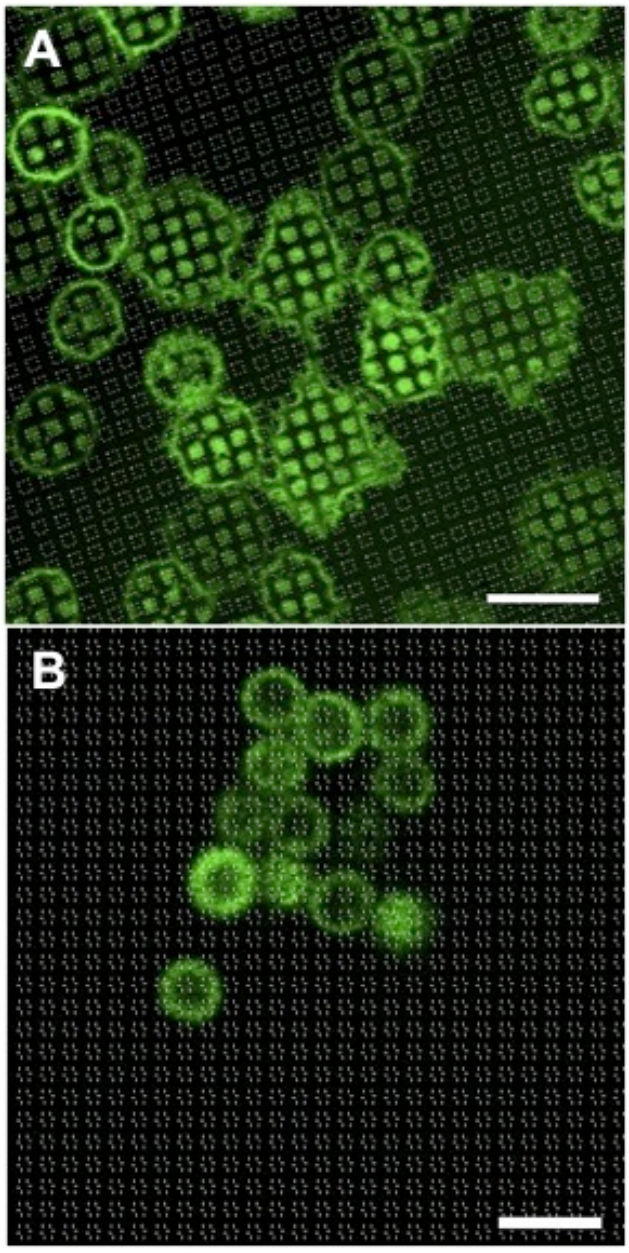

Figure 2.8: Inhibition of integrin receptor binding prevents membrane accumulation over PAA brushes. Confocal fluorescence micrographs show A488-IgE labeled cells incubated on PAA (~30 nm thick) surfaces patterned with 2 μm square features. A) Cell membrane accumulates over brush patterns in the absence of RGD peptides. B) When cells are pre-treated with 1 μg/mL RGD peptides for 30 min at 37° C, prior to incubation with the patterned surface, membrane does not accumulate over the PAA brushes. Scale bar is 20 μm.

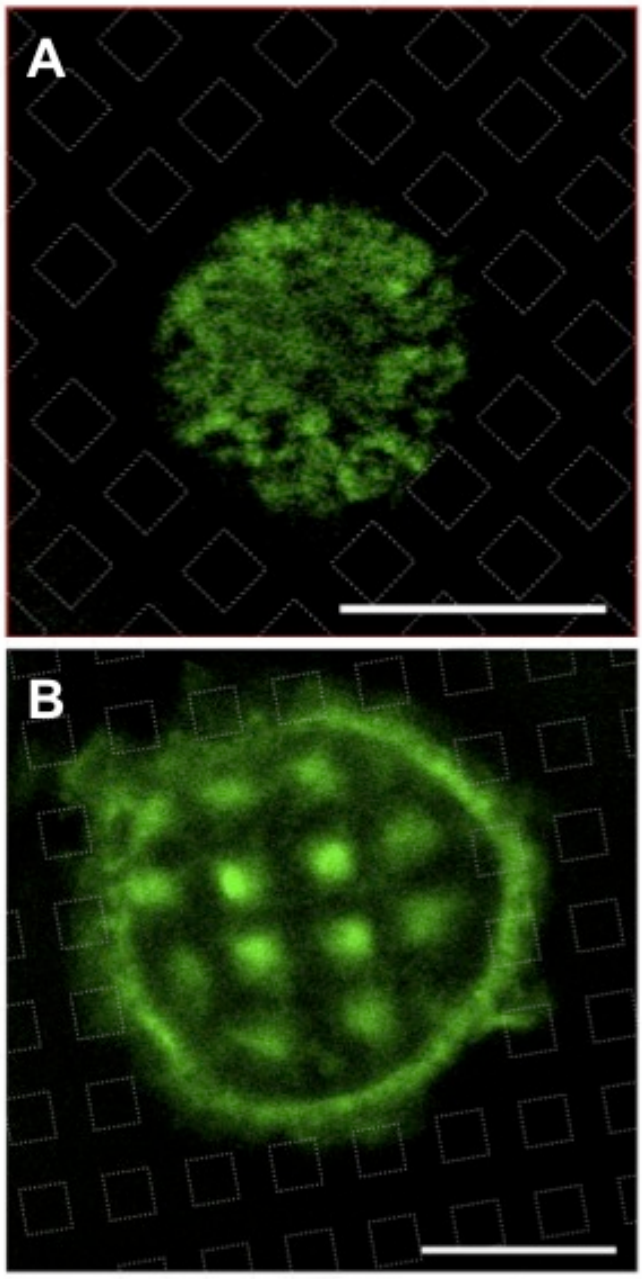

Figure 2.9: GFP-actin accumulates over patterned PAA brush regions at 37° C, but not at room temperature. Confocal fluorescence micrographs show cells expressing GFP-actin incubated on PAA (~30 nm thick) surfaces patterned with 2 μm square features for 20 min at room temperature. A) GFP-actin does not accumulate over PAA regions at room temperature. B) GFP-actin redistributes to PAA regions at 37° C. Scale bar is 10 μm.

To further implicate actin in this process, we investigated the effects of cytochalasin D, a drug that inhibits actin polymerization, on plasma membrane accumulation over patterned PAA (~30 nm thick) regions (2 μm squares). When A488-IgE sensitized cells are pre-treated with cytochalasin D for 10 min at 37° C and then incubated for 20 min at 37° C, membrane does not accumulate over PAA regions (Figure 2.10A). After the subsequent removal of cytochalasin D and re-incubation at 37° C for 20 min, membrane accumulates over PAA regions (Figure 2.10B). However, if cells are first incubated on patterned PAA surfaces for 20 min at 37° C (Figure 2.10C) and then treated with cytochalasin D (Figure 2.10D), we observe a sustained accumulation of membrane over PAA regions. These results indicate that while localized actin polymerization initiates the recruitment of membrane to PAA regions, sustained membrane accumulation over PAA does not require continuing actin polymerization.

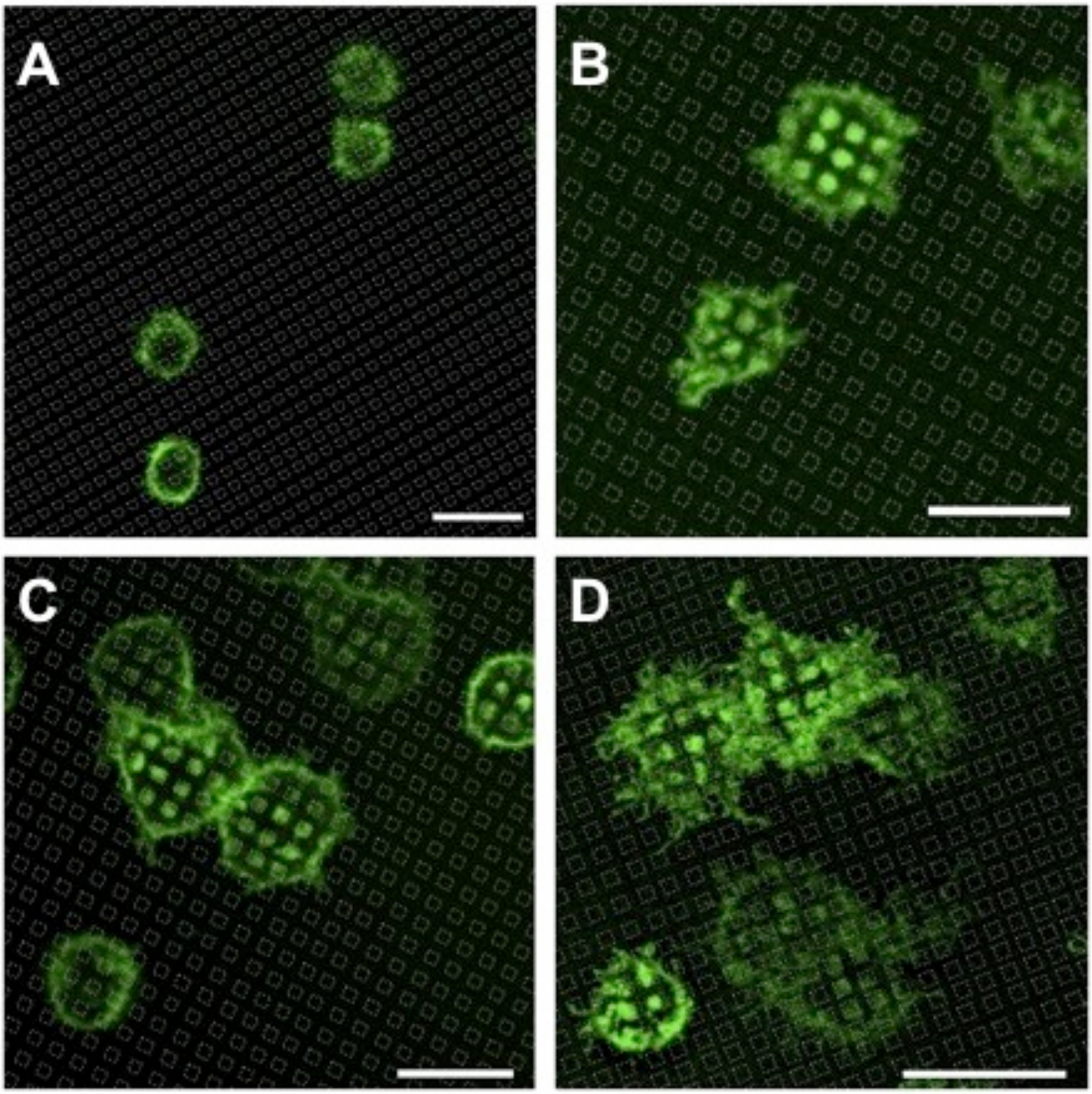

Figure 2.10: Cytochalasin D prevents membrane accumulation over patterned PAA regions. Confocal fluorescence micrographs show A488-IgE labeled cells incubated on PAA (~30 nm thick) surfaces patterned with 2 μm features. A) Pre-treatment with cytochalasin D for 10 min at 37˚ C prevents membrane accumulation over PAA regions. B) Subsequent removal of cytochalasin D and re-incubation at 37˚ C causes membrane to accumulate over PAA regions. C) Membrane accumulates over PAA at 37˚ C. D) Membrane, which had previously accumulated over PAA regions (as observed in (C)), does not redistribute away from PAA regions after similar treatment with cytochalasin D. Scale bar is 20 μm.

Tuning Membrane Accumulation by Varying PAA Brush Thickness.

As described above, cells incubated on 30 nm thick patterned PAA surfaces undergo an orchestrated membrane reorganization that is driven by the chemical and topographical properties of the patterned PAA arrays. Motivated by previous studies, which suggest that topographical depth of patterned features influences cell adhesion, we explored the role of PAA brush thickness (i.e., the height from the silicon surface to the tip of the extended brush structures) in regulating the recruitment of membrane to PAA regions. Therefore, in addition to the 30 nm thick PAA brushes used in all experiments discussed thus far, we also synthesized PAA brushes with reduced thicknesses (15 nm and 8 nm). A488-IgE labeled cells were incubated for 20 min at 37˚ C on patterned PAA surfaces (with 2 μm square features) with varying brush thicknesses and imaged using confocal fluorescence microscopy. We found that the plasma membrane strongly accumulates over 30 nm (as expected from all previous experiments) and 15 nm thick PAA brushes, as illustrated in Figure 2.11A-B. However, when PAA brush thickness is reduced to 8 nm, membrane no longer accumulates over PAA regions, and cell adhesion (cell density) is equivalent to that observed for 30 nm thick PAA surfaces with 2 μm features (Figure 2.3D) and on bare silicon (Figure 2.4).

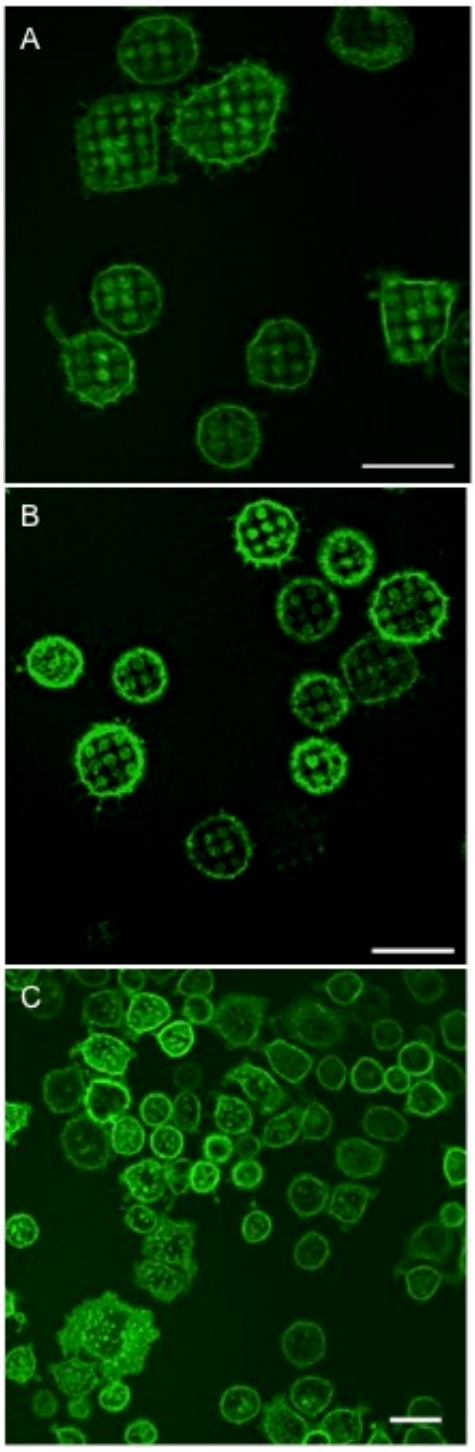

Figure 2.11: Membrane accumulates over patterned PAA brushes as a function of increased brush thickness. Confocal fluorescence images of A488-IgE labeled cells incubated for 20 min at 37˚C on PAA (~30 nm thick) surfaces patterned with 2 μm square features. Dry brush thickness is 30 nm (A), 15 nm (B), and 8 nm (C). Scale bar is 20 μm.

Patterned PAA-DNP Arrays for Spatially Restricting IgE-FcεRI Signaling.

The ability to reduce membrane accumulation (integrin-mediated) at the plasma membrane-PAA brush interface using thin (~8 nm) PAA brushes provided the impetus to investigate the utility of these surfaces as versatile arrays for studying specific cell-surface interactions. As such, we investigated whether patterned PAA surfaces could be conjugated with ligands that selectively engage specific cell surface immune receptors. Previously, patterned lipid bilayers [6] and SAMs [7] containing 2,4-dinitrophenyl (DNP) ligands were utilized to specifically crosslink anti-DNP IgE bound to cell surface FcεRI in RBL cells. We prepared patterned PAA-DNP ligand arrays by chemically functionalizing thin (~8 nm) patterned PAA brushes (2 μm square feature sizes) with DNP-PEG, as described in Materials and Methods. Incorporation of a PEG linker reduces non-specific interactions between the substrate and other proteins and provides flexibility to the DNP-brushes in cell media. This provides DNP groups better accessibility to IgE antibodies, which is necessary for robust clustering of cell surface IgE-FcεRI [8].

Cells were labeled with A488-IgE and visualized using confocal fluorescence microscopy. After cell incubation on patterned PAA-DNP surfaces (2 μm squares) for 20 min at 37˚ C, A488-IgE accumulated over PAA-DNP regions (Figure 2.12A). The specificity of IgE-FcεRI redistribution to PAA-DNP was confirmed by double labeling cells with A488-IgE, as well as the fluorescent lipid analogue, DiI-C_{16}. As expected, A488-IgE-FcεRI accumulated over PAA-DNP regions (Figure 2.12B), while DiI-C_{16} remained

uniformly distributed over both silicon and PAA-DNP regions (Figure 2.12C). The lack of visual correlation between IgE-FcεRI and $DiIC_{16}$ (Figure 2.12D) indicates selective redistribution of IgE-FcεRI to PAA-DNP arrays.

2.4 DISCUSSION

The incorporation of materials and devices into biological systems triggers surrounding cells and tissues to initiate cellular responses that either favor device assimilation or promote rejection. The importance of guaranteeing a material's biocompatibility is underscored by the increasing utilization of non-biological materials in clinical research and medicine (for example, over 800,000 hip replacement surgeries are performed annually worldwide [9]). For this reason, the ability to control interactions at the interface between non-biological materials and cells within host tissues is being ardently pursued in the field of biomedical engineering.

In vivo, cell membranes are surrounded by a highly porous meshwork of glycosaminoglycans and fibrous proteins, such as fibronectin and collagen, forming the ECM. Several techniques are commonly used to impart bio-mimetic properties to a material's surface, including: adsorption and covalent attachment of adhesion-promoting biomolecules [10], modulating surface topology [11], and modified surface chemistries [12]. Polymer brushes have gained increasing popularity over the last decade as a means of incorporating versatile functionality to a material's surface.

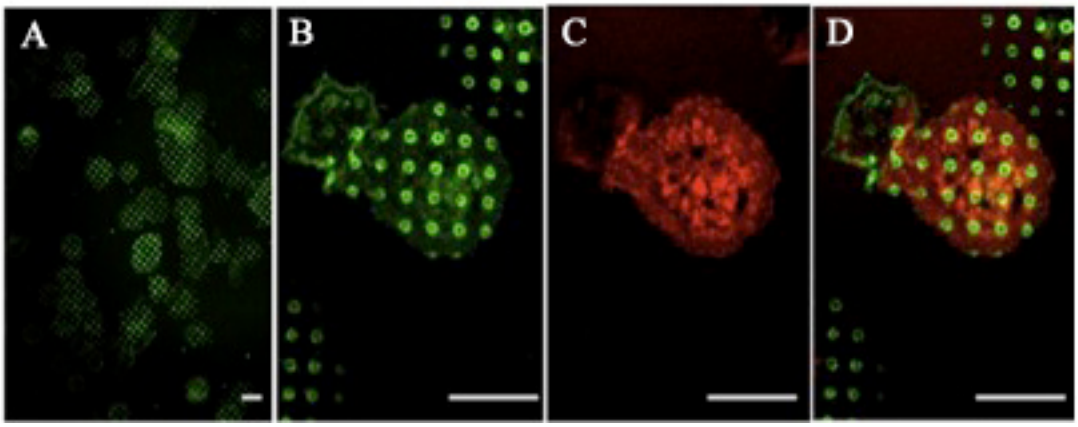

Figure 2:12. Patterned DNP-PAA brushes specifically crosslink IgE-FcεRI. Cells were labeled with A488-IgE (green) and $DiIC_{16}$ (red) and incubated on thin (~8 nm) patterned (2 μm squares) PAA-DNP surfaces at 37° C for 20 min. A) IgE-FcεRI selectively accumulates over patterned DNP-PAA regions. B) Higher magnification of (A). C) The fluorescent membrane marker $DiIC_{16}$ is uniformly distributed over the same cell shown in (B). D) Membrane fluorescence (red) is uncorrelated to the patterned arrays of fluorescently labeled IgE-FcεRI (green), indicating that only IgE-FcεRI selectively binds and accumulates over DNP-PAA brushes. Scale bar is 10 μm.

Of particular interest to this study is PAA's ability to act as a scaffold for immobilizing different biomolecules with specific cellular functions. Due to a high concentration of carboxylic acid groups (-COOH), unmodified PAA brushes have a strong capacity to adsorb proteins [13] and have thus been exploited as scaffolds for immobilizing collagen to enhance cell adhesion [14]. Additionally, PAA has been covalently modified with various proteins, demonstrating their utility as patterned protein arrays [3]. In this study, we used patterned PAA brushes to explore the effects of both surface chemistry and topography (pattern dimensions and thickness) on cell-surface interactions.

When RBL mast cells are incubated on surfaces composed of 100% PAA, very few cells attach to the PAA brush surface. This is consistent with previous reports that demonstrate PAA surface modification adversely affects cell adhesion [15]. Consequently, it is not surprising that cells incubated on PAA surfaces patterned at large dimensions (larger than the size of a cell) preferentially adhere to bare silicon regions (Figure 2.3A-C). Interestingly, when PAA brushes are patterned at dimensions smaller than that of a cell (2 μm squares) we found that 1) cells attach and spread over both PAA and silicon regions (Figure 2.3D) and 2) cell membrane selectively accumulates over (previously cell-repellent) PAA regions (Figure 2.5) at 37° C, and much less at room temperature (Figure 2.6). We also found that the accumulation of membrane over PAA regions is PAA brush thickness-dependent (i.e., reducing brush thickness from 30 nm to 8 nm prevents membrane accumulation), as shown in Figure 2.11. Additionally, we showed that soluble

fibronectin selectively accumulates over patterned PAA regions (Figure 2.7) and hypothesized that membrane accumulation is mediated by fibronectin-rich PAA regions. This may be due to the large surface area of the PAA brushes, and it is consistent with PAA brush thickness-dependent membrane accumulation over PAA regions.

Given the high concentration of fibronectin over patterned PAA regions, we hypothesized that integrin receptors were being selectively crosslinked over PAA regions. To test this, we prevented binding between cell surface integrin receptors and fibronectin-rich PAA brushes using RGD-containing peptides. Under these conditions, cell membrane does not accumulate over PAA regions (Figure 2.8), suggesting that membrane accumulation requires integrin activation via fibronectin binding.

One important consequence of multiple integrin engagement with fibronectin is rapid actin polymerization that accompanies localized cytoskeleton remodeling [16]. To test whether membrane redistribution to PAA regions is driven by integrin-dependent actin reorganization, we first confirmed that GFP-actin accumulates over PAA regions (Figure 2.9). We then demonstrated that inhibiting actin polymerization prevents membrane accumulation over PAA regions (Figure 2.10A). Interestingly, while actin polymerization drives the formation of accumulated membrane structures over PAA regions, persistent actin polymerization is not required for sustained membrane association with PAA brushes (Figure 2.10D).

Many actin-rich membrane structures have been identified in RBL cells such as membrane ruffles, protrusions, and podosomes, and these have been shown to play important roles in cell adhesion and motility, membrane trafficking, and signaling. Despite varied diversity in protein composition and morphology, these structures serve a common purpose for sensing, responding, and interacting with the surrounding ECM.

One type of membrane extension that has several hallmarks consistent with the structures we observe at the cell membrane-PAA brush interface is invadopodia. These membrane structures are highly enriched in actin and adhesion receptor molecules, and they have been implicated in tissue invasiveness and proteolytic ECM degradation [17-20]. Given the high local concentration of fibronectin at the PAA brush-membrane interface, we hypothesize that actin polymerization drives the formation of interdigitating membrane structures that are structurally and functionally related to invadopodia. Both the high concentration of fibronectin, as well as the porous nature of the PAA brushes, may cause the cell plasma membrane to actively investigate the patterned regions. In fact, Moran-Mirabal et al. showed that the plasma membrane structures actively investigate nanofabricated holes (40 nm -150 nm), most likely through an actin-dependent mechanism [21]. The large-scale accumulation of membrane over PAA regions may represent micron-sized membrane structures that concentrate the lipids and proteins necessary for initiating and sustaining invadopodia-like interactions.

Previous studies have suggested that cell adhesion to artificial substrates can induce rapid actin polymerization, cell spreading, and frustrated phagocytosis [22]. Previous observations of phagocytic degradation of collagen and fibronectin in fibroblasts and epithelial cells provide several parallels to our own findings [23]. It has been suggested that collagen phagocytosis involves the extension of membrane protrusions that surround and enclose collagen fibrils, followed by the activation and release of proteolytic enzymes such as matrix metalloproteases (MMPs) [24]. In a similar fashion, RBL-2H3 cells may actively explore the porous fibronectin-rich PAA patterns, and subsequent fibronectin-integrin engagement initiates actin remodeling and triggers an integrin-mediated phagocytic response [23]. If cells are unable to internalize the densely adsorbed fibronectin-PAA network, frustrated phagocytosis may occur, resulting in the concomitant release of MMPs and reactive oxygen species capable of breaking down the ECM [25] . Further, it has been shown that ECM fragments exhibit chemotactic activity [26]; thus, ECM degradation over PAA patterns may sustain membrane accumulation over PAA brushes and further drive the formation of invadopodia-like structures at the cell-surface interface.

This study was, in part, motivated by the observation that much work in the field of biomaterials uses cell adhesion statistics as a readout of successful biocompatibility. While this represents one useful metric for assessing a material's biocompatibility, our findings clearly demonstrate that, independent of favorable adhesion statistics, engineered surfaces can induce multiple non-linear effects on cellular responses dependent on surface

composition and patterning morphology. Such responses may or may not be desirable for a given application. The capacity to generate cell-adhesive surfaces from cell-repellent materials using patterned surface morphologies may provide useful strategies for enhancing the biocompatibility of similarly incompatible materials. Additionally, the capacity to 'tune-down' cellular responses elicited by patterned PAA surfaces, as well as immobilize biomolecules and ligands that specifically target cell surface proteins, demonstrates that PAA arrays are versatile substrates for engineering biological-materials interfaces for a wide variety of applications.

REFERENCES

1. Moore, J.S., Stupp, S.I., *Room-Temperature Polyesterification.* Macromolecules, 1990. **23**: p. 65-70.
2. Larson, D.R., et al., *Temporally resolved interactions between antigen-stimulated IgE receptors and Lyn kinase on living cells.* J Cell Biol, 2005. **171**(3): p. 527-36.
3. Dong, R., et al., *Patterned biofunctional poly(acrylic acid) brushes on silicon surfaces.* Biomacromolecules, 2007. **8**(10): p. 3082-92.
4. Dong, R., *Synthesis, Characterization And Biological Applications Of Polyelectrolyte Brushes*, in *Department of Chemistry and Chemical Biology*. 2009, Cornell University: Ithaca.
5. Baird, E.J., et al., *Highly effective poly(ethylene glycol) architectures for specific inhibition of immune receptor activation.* Biochemistry, 2003. **42**(44): p. 12739-48.
6. Wu, M., et al., *Visualization of plasma membrane compartmentalization with patterned lipid bilayers.* Proc Natl Acad Sci U S A, 2004. **101**(38): p. 13798-803.
7. Senaratne, W., et al., *Functionalized surface arrays for spatial targeting of immune cell signaling.* J Am Chem Soc, 2006. **128**(17): p. 5594-5.
8. Das, R., et al., *Binding mechanisms of PEGylated ligands reveal multiple effects of the PEG scaffold.* Biochemistry, 2008. **47**(3): p. 1017-30.
9. White, L.M., et al., *Complications of total hip arthroplasty: MR imaging-initial experience.* Radiology, 2000. **215**(1): p. 254-62.

10. Altankov, G., F. Grinnell, and T. Groth, *Studies on the biocompatibility of materials: fibroblast reorganization of substratum-bound fibronectin on surfaces varying in wettability.* J Biomed Mater Res, 1996. **30**(3): p. 385-91.
11. Kam, L., et al., *Correlation of astroglial cell function on micro-patterned surfaces with specific geometric parameters.* Biomaterials, 1999. **20**(23-24): p. 2343-50.
12. Keselowsky, B.G., D.M. Collard, and A.J. Garcia, *Integrin binding specificity regulates biomaterial surface chemistry effects on cell differentiation.* Proc Natl Acad Sci U S A, 2005. **102**(17): p. 5953-7.
13. Dai, J., et al., *High-capacity binding of proteins by poly(acrylic acid) brushes and their derivatives.* Langmuir, 2006. **22**(9): p. 4274-81.
14. Bisson, I., et al., *Acrylic acid grafting and collagen immobilization on poly(ethylene terephthalate) surfaces for adherence and growth of human bladder smooth muscle cells.* Biomaterials, 2002. **23**(15): p. 3149-58.
15. Gupta, B., et al., *Plasma-induced graft polymerization of acrylic acid onto poly(ethylene terephthalate) films: characterization and human smooth muscle cell growth on grafted films.* Biomaterials, 2002. **23**(3): p. 863-71.
16. Lofgren, R., et al., *Beta 2 integrin engagement triggers actin polymerization and phosphatidylinositol trisphosphate formation in non-adherent human neutrophils.* J Cell Biol, 1993. **123**(6 Pt 1): p. 1597-605.
17. Bowden, E.T., et al., *Co-localization of cortactin and phosphotyrosine identifies active invadopodia in human breast cancer cells.* Exp Cell Res, 2006. **312**(8): p. 1240-53.

18. Coopman, P.J., et al., *Integrin alpha 3 beta 1 participates in the phagocytosis of extracellular matrix molecules by human breast cancer cells.* Mol Biol Cell, 1996. **7**(11): p. 1789-804.

19. Linder, S., *The matrix corroded: podosomes and invadopodia in extracellular matrix degradation.* Trends Cell Biol, 2007. **17**(3): p. 107-17.

20. Stylli, S.S., A.H. Kaye, and P. Lock, *Invadopodia: at the cutting edge of tumour invasion.* J Clin Neurosci, 2008. **15**(7): p. 725-37.

21. Jose M Moran-Mirabal, A.J.T., Kevan T Samiee, Barbara A Baird, Harold Craighead, *Cell investigation of nanostructures: zero-mode waveguides for plasma membrane studies with single molecule resolution.* Nanotechnology, 2007(19).

22. Bengtsson, T., et al., *Actin dynamics in human neutrophils during adhesion and phagocytosis is controlled by changes in intracellular free calcium.* Eur J Cell Biol, 1993. **62**(1): p. 49-58.

23. Zhao, M.W., et al., *A distinct integrin-mediated phagocytic pathway for extracellular matrix remodeling by RPE cells.* Invest Ophthalmol Vis Sci, 1999. **40**(11): p. 2713-23.

24. Everts, V., et al., *Phagocytosis and intracellular digestion of collagen, its role in turnover and remodelling.* Histochem J, 1996. **28**(4): p. 229-45.

25. Clark, R.A., K. Ghosh, and M.G. Tonnesen, *Tissue engineering for cutaneous wounds.* J Invest Dermatol, 2007. **127**(5): p. 1018-29.

26. Senior, R.M., G.L. Griffin, and R.P. Mecham, *Chemotactic responses of fibroblasts to tropoelastin and elastin-derived peptides.* J Clin Invest, 1982. **70**(3): p. 614-8.

CHAPTER THREE

Correlation Analysis of SEM Images Corrects for Artifactual Self-Clustering and Quantifies Co-localization of FcεRI and Lyn in Unstimulated RBL Mast Cells*

Summary

We use pair auto- and cross-correlation functions to quantify lateral heterogeneity within the plasma membranes of unstimulated RBL-2H3 mast cells. Immuno-gold labeled proteins and lipids in plasma membranes of intact cells are visualized using scanning electron microscopy (SEM). Consistent with previous reports, a variety of gold-labeled plasma membrane proteins appear clustered, but we find that this clustering can be accounted for by multiple gold particles binding to individual target proteins. We demonstrate this artifactual clustering: by imaging proteins conjugated to a silicon surface, by comparing correlation functions for a wide range of cell surface labels with varying surface densities, and by measuring cross-correlations between functionally identical but distinguishably labeled pools of either IgE-FcεRI or CTxB-GM_1. We determined that none of the several membrane proteins we examined are significantly self-clustered after correcting for multiple labels. In contrast, we find significant cross-correlation between IgE-FcεRI and its inner leaflet signaling partner Lyn kinase.

* This work was done in collaboration with Sarah Veatch, who developed the analytical methods to robustly quantify gold-labeled protein distributions and correct for artifactual gold labeling, and Prabbuddha Sengupta, who provided SEM images of 5 nm gold labeled Thy-1, YFP-GT46, and YFP-GPI.

3.1 INTRODUCTION

Numerous biochemical and biophysical studies support the hypothesis that cell plasma membranes are heterogeneous on the nano-scale, and that this plays regulatory and targeting roles in cell function [1-3]. However, direct imaging studies of plasma membrane heterogeneity have been limited because domains and other predicted structures, if present, are smaller than can be visualized using traditional optical imaging techniques [4-6]. For this reason, electron microscopy has been widely used to examine the nano-scale lateral heterogeneity in cell plasma membranes [7-17]. For visualization of specific components, membrane proteins and lipids are typically labeled with primary antibodies and secondary gold-antibody conjugates. Electron microscopy is used to image gold particles on intact cells [13, 14] or on "ripped-off" membrane sheets [7-12, 15-18]. In most cases, gold-labeled membrane proteins have been reported to self-associate into small and distinct cell surface clusters, and these findings of self-clustering have contributed to our current view of membrane heterogeneity and its participation in cell function [19-21].

We developed experimental and analytical methods to investigate the structural manifestation of plasma membrane heterogeneity in resting cells that may be relevant for changes that occur with cell activation. We used scanning electron microscopy (SEM) with both secondary electron detection (SED) and backscattered electron detection (BSD) to examine immuno-gold labeling of IgE-FcεRI and a variety of plasma membrane proteins in

unstimulated RBL mast cells. We quantify images of gold particle centers using pair auto- or cross-correlation functions. Correlation functions provide advantages over commonly used Ripley's methods because they are intuitive, straightforward to calculate, and can be used to explore the physical interactions that give rise to spatial organization. We utilize these properties to investigate why immuno-gold particles labeling plasma membrane proteins appear self-clustered in unstimulated cells, as has been reported in related studies [8, 15-17].

RBL-2H3 mast cells provide a useful model system for investigating plasma membrane lateral heterogeneity because membrane organization has been linked to functional responses [2]. Multivalent crosslinking of IgE bound with high affinity to its receptor FcεRI initiates a signaling cascade that leads to the release of secretory granules containing histamine and other mediators of inflammatory responses. It is well documented that early steps in this stimulated response take place at the plasma membrane and are modulated by alterations in membrane structure [2, 22-24]. In this study, we monitor lateral distributions of two proteins involved in early steps of this pathway: IgE bound to transmembrane FcεRI and Lyn, a Src family kinase, that is anchored to the inner leaflet of the plasma membrane by saturated acyl chains. We also monitor the resting cell distributions of plasma membrane components typically associated either with ordered lipid "raft" domains (cholera toxin B subunit bound to the ganglioside GM_1, glycosyl phosphatidyl inositol (GPI)-linked Thy-1, and YFP-GPI) or with disordered, "non-raft" environments (YFP-GT46). Our results show that apparent self-clustering of plasma

membrane proteins commonly arises from binding of multiple gold-conjugated antibodies to the same target protein. Our results further provide new evidence for some co-localization of FcεRI and Lyn kinase in unstimulated cells.

3.2 MATERIALS and METHODS

Chemicals and Reagents:

Rabbit anti-Alexa Fluor 488 (A488), A488-cholera toxin subunit B (A488-CTxB), and FITC-cholera toxin subunit B (FITC-CTxB) were purchased from Invitrogen Corp. (Eugene, OR). Mouse anti-Lyn (H-6) was purchased from Santa Cruz Biotechnology Inc. (Santa Cruz, CA). Mouse mAb OX-7 (anti-Thy-1) was purchased from BDPharmingen (San Diego, CA). Glutaraldehyde (25% stock) was purchased from Ted Pella Inc. (Redding, CA). Paraformaldehyde was purchased from Electron Microscopy Services (Hatfield, PA). Mouse anti-FITC, mouse anti-GFP (and YFP), 3-aminopropyltriethoxysilane (APTES), 10 nm gold-conjugated anti-rabbit IgG (whole molecule), 10 nm gold-conjugated anti-mouse IgG (whole molecule), methyl-β-cyclodextrin (MβCD), and cholesterol-loaded MβCD were purchased from Sigma (St. Louis, MO). 5 nm gold-conjugated anti-rabbit IgG (whole molecule) was purchased from GE Healthcare (Piscataway, NJ). Rabbit anti-actin was purchased from Abcam (Cambridge, MA). A488-IgE and FITC-IgE were prepared by modification of purified mouse monoclonal anti-2,4-dinitrophenyl (DNP) IgE with FITC or A488 (Invitrogen Corp.) as previously described [25, 26]. Vectors containing cDNA for YFP-GT46 and

YFP-GL-GPI were provided by J. Lippincott-Schwartz (NIH, Bethesda) and A. Kenworthy (Vanderbilt University School of Medicine, Nashville, TN), respectively, and the plasmids encoding monomeric YFP-GL-GPI and monomeric YFP-GT46 were constructed from YFP-GL-GPI and YFP-GT46 by introducing the A206K mutation [27] as previously described [28].

Cell Culture and SEM Sample Preparation:

RBL-2H3 mast cells were grown overnight to ~50% confluency on 2 mm x 2 mm silicon chips at 37° C under standard cell culture conditions [29], and high affinity IgE receptors (FcεRI) were labeled with A488-IgE (1 μg/mL) for 2-3 hours and washed before preparing samples for SEM. In double label IgE or CTxB experiments cells were sensitized with a 1:1 mixture of A488-IgE and FITC-IgE (total of 1 μg/mL) or incubated for 1 hr with a 1:1 mixture of A488-CTxB and FITC-CTxB (total 1.5 μg/mL). For some experiments, cells were incubated for 5 min at 37° C with either 10 mM MβCD or 10 mM cholesterol-loaded MβCD. Cells were quickly washed in phosphate buffered saline (PBS) and immediately fixed in 4% (w/v) paraformaldehyde and 0.1% (w/v) gluteraldehyde for 10 min at room temperature in PBS. Fixed cell samples were washed in blocking solution (2mg/mL BSA and 2% (v/v) fish gelatin in PBS) and labeled sequentially with primary antibodies and secondary antibody-gold conjugates (5 or 10 nm diameter) in the presence (usual) or absence (control) of 0.1% Triton X-100 (TX-100) in blocking solution. Each antibody labeling incubation was 1 hr at room temperature with wash steps in between. For labeling with differently sized gold particles, samples

were first labeled with 10 nm and then 5 nm gold antibody conjugates. The immuno-gold labeled cell samples were further fixed in 4% paraformaldehyde and 1% gluteraldehyde for 5 min at room temperature, and then thoroughly washed in distilled water. Following dehydration through a series of graded ethanol washing steps, samples were critical point dried, mounted on round aluminum SEM stubs, and sputtered with carbon to prevent charging.

Preparation of Immobilized Gold on Surfaces:

Following plasma-treatment, silicon chips were immersed in a 2% (v/v) APTES solution in acetone for 10 min and thoroughly washed with acetone and then PBS. These amino-functionalized surfaces were then treated with 0.1% glutaraldehyde (in PBS) for 30 min at room temperature, followed by a 1 hr incubation at room temperature with either 10 μg/mL or 50 μg/mL A488-IgE. A488-IgE immobilized surfaces were labeled with primary and gold-conjugated secondary antibodies and prepared for SEM imaging as described above for cell samples.

Electron Microscopy and Imaging Statistics:

Mounted samples were imaged with a Schottky field emission scanning electron microscope (LEO 1550) at 20KeV. The dorsal (top) surfaces of intact, adherent cells were imaged using secondary electron detection (SED) and backscattered detection (BSD) at high magnification. Flat membrane regions were selected for imaging. For imaging with 10 nm gold particles, individual micrographs were obtained at 35K magnification, and typical images cover 2.4

μm^2 of the cell surface. For imaging 5 nm gold particles and in double label experiments with 10 nm and 5 nm gold particles, micrographs were obtained at 75K-100K magnification. Immuno-gold labeled protein distributions for many different cells and many experiments were obtained for all experimental conditions presented. The total number of gold particles, total area imaged, and gold-labeled densities for samples analyzed in this study are summarized in Table 3.1.

Labeling Controls:

Gold labeling of A488-IgE-FcεRI and Lyn is observed in the presence of specific primary antibodies and species-specific gold-conjugated secondary antibodies. As illustrated by representative BSD-SEM images shown in Figure 3A.1 (Appendix), non-specific background binding of gold-conjugated secondary antibodies is not significant in the absence of specific primary antibodies (Figure 3A.1A and 3A.1B) or in the presence of irrelevant primary (Figure 3A.1C) or non species-specific secondary antibodies (Figure 3A.1D). In the absence of 0.1% TX-100 we do not detect gold labeling of inner leaflet proteins (Figure 3A.1E), and we determined that IgE-FcεRI distributions are independent of the presence or absence of TX-100 during the labeling step (not shown). We also confirmed that gold labeling of Lyn is independent of whether or not cells are sensitized with IgE (Figure 3A.1F). We compared the distribution of A488-IgE-FcεRI and FITC-IgE-FcεRI, labeled with anti-A488 pAb and anti-FITC mAb, respectively, and we determined that gold particle distributions are similarly obtained regardless of which specific primary

antibody or gold particle size was used (data not shown). Similarly, labeling of Lyn with either monoclonal or polyclonal anti-Lyn antibodies followed by species-specific gold-conjugated secondary antibodies were compared and found to be similar (data not shown).

Tabulation of Correlation Functions:

Pair auto- and cross- correlation functions were tabulated in Matlab (Mathworks, Natick, MA) using Fast Fourier Transforms (FFTs) as follows:

$$g(\vec{r}) = \frac{FFT^{-1}(\left|FFT(1)^2\right|)}{\rho_{gold}{}^2 N(\vec{r})}$$

where FFT^{-1} is an inverse Fast Fourier Transform, I is a binary image where pixels have a value of 1 at gold particle centers and all other pixels have a value of 0, and $N(\vec{r})$ is a normalization that accounts for the finite size of the acquired image. The image I is padded with zeros in both directions out to a distance larger than the range of the desired correlation function (maximally the size of the original image) to avoid artifactual correlations due to the periodic nature of FFT functions. The normalization factor N is the autocorrelation of a window function W that has the value of 1 inside the measurement area, and is also padded by an equal number of zeros.

$$N(\vec{r}) = FFT^{-1}(\left|FFT(W)\right|^2)$$

This Normalization corrects for the fact that there are fewer possible pairs separated by large distances due to the finite image size.

Cross-correlation functions between images of 5 nm and 10 nm particle centers (I_{5nm} and I_{10nm} respectively) are tabulated in a similar manner:

$$c(\vec{r}) = \mathrm{Re}\left\{\frac{FFT^{-1}(FFT(I_{5nm})) \times conj(FFT(I_{10nm}))}{\rho_{5nm}\rho_{10nm}N(\vec{r})}\right\}$$

Here conj() indicates a complex conjugate, ρ_{5nm} and ρ_{10nm} are the average surface densities of 5 nm and 10 nm particles respectively, and Re{} indicates the real part. This computation method of tabulating pair auto- and cross-correlations is mathematically identical to brute force averaging methods.

Correlation functions were angularly averaged by first converting to polar coordinates using the Matlab command cart2pol, and then binning by radius. *g(r)* values are obtained by averaging $g(\vec{r})$ values that correspond to the assigned bins in radius. Errors in *g(r)* are standard errors of the mean.

3.3 RESULTS

SEM Images are Analyzed using Correlation Functions.

We used standard procedures to prepare samples for SEM: cells are fixed with 4% paraformaldehyde and 0.1% gluteraldehyde, and target proteins are labeled with primary and gold-conjugated secondary antibodies, followed by second fixation with 4% paraformaldehyde and 1% gluteraldehyde (details provided in Materials and Methods). In the SEM micrographs, flat regions of the intact cell are determined with SED, and gold labels in flat regions are imaged with BSD. As represented in Figure 3.1 we implemented automated image processing algorithms to identify the locations

of gold particle centers with high fidelity, enabling the processing of large data-sets with high particle densities to quantify experimental results with low error bounds. Total cell surface areas and total numbers of gold particles are reported in Table 3.1. Raw images (Figure 3.1A) undergo background subtraction and median filtering, and potential particles are identified by locating local maxima in the processed image (Figure 3.1B). Histograms of particle centroid intensity and total (integrated) intensity are assembled for all potential particles within a set of images of the same condition (typically 10 images) and are used to create objective criteria for further culling the entire data-set (Figure 3.1C). Very low intensity points of centroid intensity histograms (identified as noise) are fit to a Gaussian shape (blue line in Figure 3.1C, left panel) to define a low intensity cutoff. In single label experiments, all objects with centroid intensities larger than this cut-off value are returned. In double label experiments, the remaining objects are further culled into two categories that meet criteria for both centroid intensity and total intensity (Figure 3.1C). By this method, some ambiguous particles will be missed, but very few will be miscategorized.

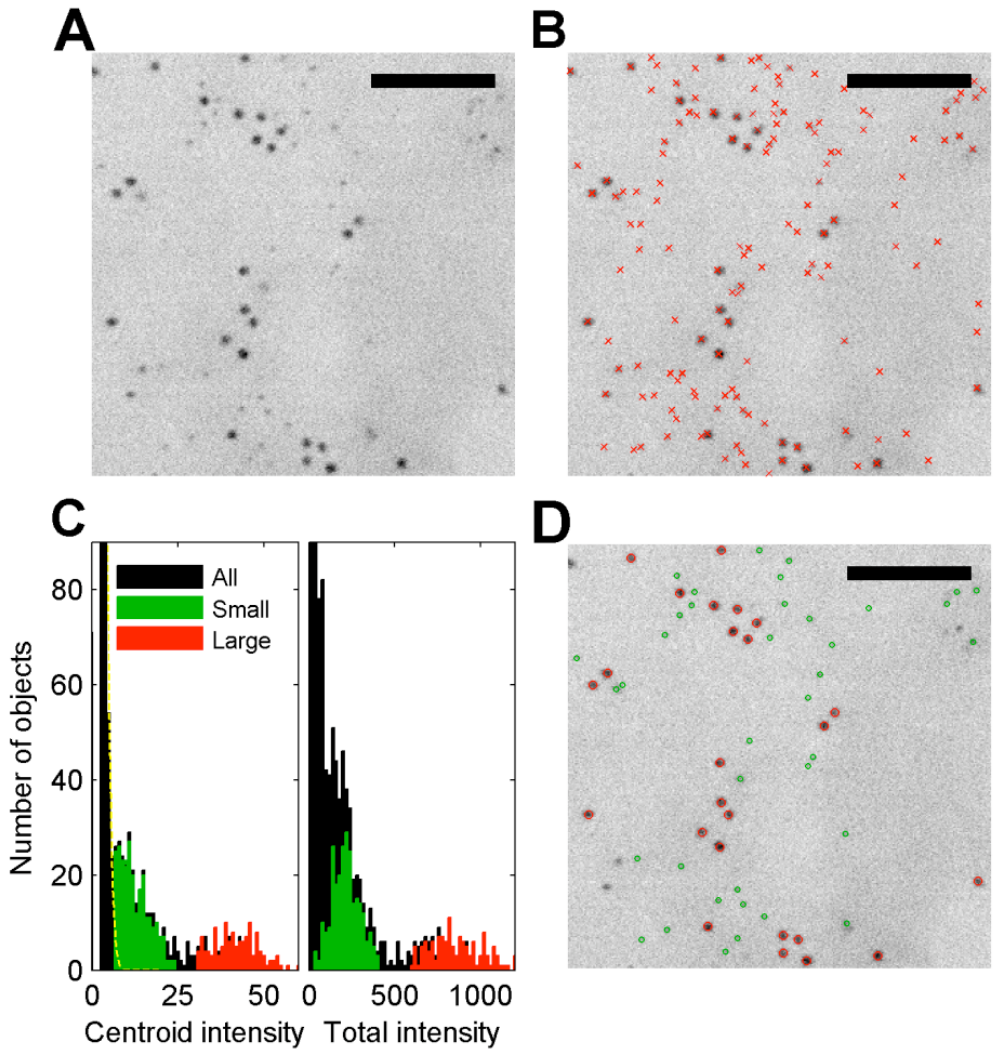

Figure 3.1: In SEM images of immuno-gold labeled membrane proteins, locations of the gold particles are identified using automated image processing algorithms. A) Raw SEM (BSD) image showing 5 nm and 10 nm gold particles from a double label experiment (10 nm Lyn and 5 nm IgE-FcεRI). B) Raw images are filtered, thresholded, and possible objects (gold particles) are identified by detecting local maxima (red crosses). C) Statistics are recorded on object intensities (centroid and total) for high fidelity identification. Objects with low centroid intensities are culled to remove contributions from noise (blue line, left panel), and small (green) and large (red) particles are distinguished through cutoffs in both centroid and total intensity. D) Computationally identified objects (red, large; green, small) are superimposed on the raw image for visual comparison. Scale bar is 200 nm.

Table 3.1: Measurement statistics and extracted fit parameters from single label experiments. N_{gold} is the total number of gold particles analyzed, Area is the total cell surface area imaged, *LE* (labeling efficiency) and σ (half-width of the Gaussian-shaped clusters, ρ_{gold} is the average surface density of gold particles, and $\rho_{protein}$ is the average protein density.

	N_{gold}	Area (μm^2)	LE	σ (nm)	ρ_{gold} (μm^{-2})	$\rho_{protein}$ (μm^{-2})
Surface	16621	149.1	0.91±0.05	9.5±0.5	110±14	120±23
GT46 (5 nm)	14597	44.5	2.1±0.09	7.6±0.1	330±35	156±23
GPI (5 nm)	12041	44.5	1.8±0.06	7.8±0.1	270±41	150±28
FcεRI (10 nm)	185054	710.6	1.6±0.03	9.1±0.2	260±11	166±10
Lyn (10 nm)	10558	386.0	1.1±0.05	8.5±0.4	27±2	24±2.5
CTxB (10 nm)	76312	105.3	1.59±0.15	10.3±0.6	720±9	460±49
Thy-1 (5nm)	7095	386.0	1.8±0.08	6.5±0.1	120±3	64±5

Following image processing to identify the location of the gold labels (Figure 3.1D), pair auto- or cross-correlation functions are evaluated for each acquired image to quantify their spatial distribution. Pair correlation functions measure the increased probability of finding a second gold particle a distance r away from a given gold particle, and are conventionally defined as:

$$g(\vec{r}) = \frac{<\rho(\vec{r})\rho(\vec{r}+\vec{R})>}{<\rho(\vec{R})>^2}$$

$$c(\vec{r}) = \frac{<\rho_{big}(\vec{r})\rho_{small}(\vec{r}+\vec{R})>}{<\rho_{big}(\vec{R})><\rho_{small}(\vec{R})>}$$

where $g(\vec{r})$ is the pair auto-correlation function, $c(\vec{r})$ is the pair cross-correlation function for distinctive (*big* and *small*) particles, $\rho(\vec{r})$ is the density of gold particles at position $\vec{r}$, and the angle brackets denote an ensemble average over all positions in the image $(\vec{R})$. There is no preferred direction in these measurements, and $g(\vec{r})$ or $c(\vec{r})$ are further averaged over all angles to produce *g(r)* or *c(r)* with improved signal to noise ratio. Values of *g(r)* or *c(r)* = 1 correspond to a random distribution. In practice, we evaluate correlation functions using Fourier Transforms, and a detailed procedure is provided in Materials and Materials. The local density a distance r away from a given particle is given by $\rho_{gold} g(r)$, where ρ_{gold} is the average surface density of gold particles as measured over a large total areas (>40 μm^2).

The statistical significance of clustering can also be determined using the Ripley's K function, which measures the increased density of particles within a circle of radius r and is related to the pair correlation function

through integration, where $K(r) = \int_0^r g(r')2\pi r' dr'$

Frequently, Ripley's K function is restated when plotting the results from electron microscopy studies:

$$L(r) - r = \sqrt{K(r)/\pi} - r = \sqrt{2\int_0^r g(r')r' dr'} - r \quad (1)$$

Furthermore, *L(r) – r* curves reported in the literature are typically normalized to a confidence interval, so that the amplitudes of normalized *L(r) –r* traces indicate the statistical significance of clustering within a radius r. Confidence intervals of *L(r) –r* are calculated by propagating the statistical errors of *g(r)* through Eqn 1. Errors in *g(r)* are dominated by counting statistics that vary inversely with the square root of the number of particles found at a given distance.

Gold Particles Labeling a Variety of Plasma Membrane Proteins are Clustered.

We imaged gold particles labeling a wide variety of plasma membrane proteins in unstimulated RBL mast cells: IgE bound to endogenous FcεRI, cholera toxin subunit B (CTxB) bound to endogenous GM_1, endogenous GPI-linked Thy-1, endogenous inner leaflet anchored Lyn, and transiently expressed YFP-GPI and transmembrane protein YFP-GT46. SEM images of all of these immuno-gold labeled membrane proteins show clustered distributions in intact cells, and IgE immobilized on bare silicon has a similar appearance (Figure 3.2).

Figure 3.2: Gold particles that label target proteins on cell and silicon surfaces are clustered. All target proteins are labeled using the standard immuno-gold procedure: primary antibodies specific for protein, followed by gold-conjugated secondary antibodies. A) Clustering is evident in representative reconstructed BSD-SEM images of gold particles that label plasma membrane proteins (A488-IgE-FcεRI, YFP-GT46, CTxB bound to ganglioside GM_1), as well as A488-IgE covalently conjugated to a silicon surface. B) Pair correlation analysis of gold particle distributions from many images quantify immuno-gold labeled IgE-FcεRI in the plasma membrane. C) Data sets over many images of specified target proteins (Table 3.1) are evaluated with correlation functions, *g(r) vs.* r (left) and Ripley's functions *L(r)-r vs* r (right). The correlation curves in the left panel are fit for r >10 nm by Gaussian functions centered at r=0 (Eqn 3, solid lines), and the amplitude of correlations for Lyn (blue diamonds) are larger than for other proteins investigated. The Ripleys' functions in the right panel are generated from correlation functions using Eqn 1.

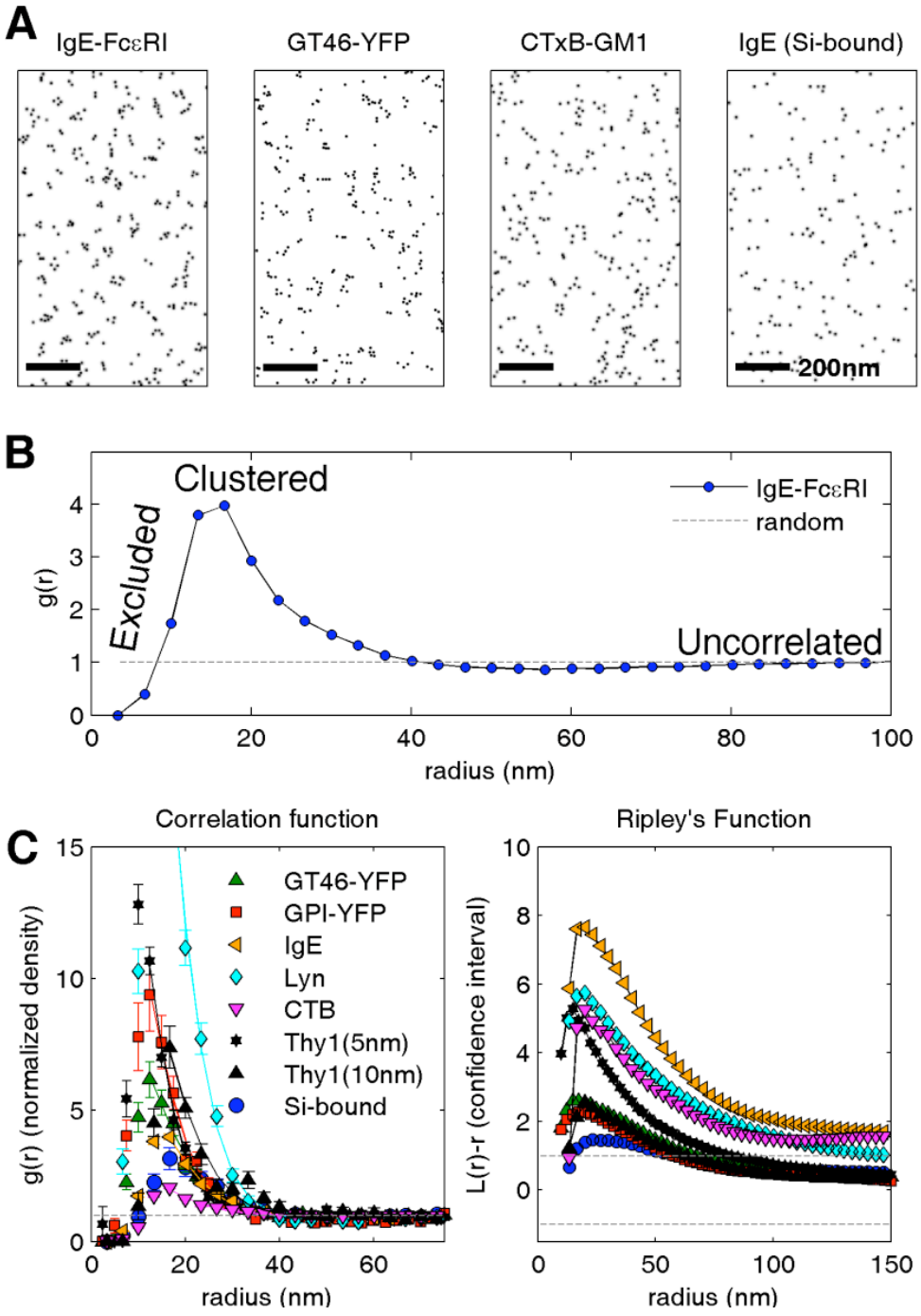
A
IgE-FcεRI
GT46-YFP
CTxB-GM1
IgE (Si-bound)
200nm
B
Clustered
Excluded
Uncorrelated
IgE-FcεRI
random
g(r)
radius (nm)
C
Correlation function
Ripley's Function
GT46-YFP
GPI-YFP
IgE
Lyn
CTB
Thy1(5nm)
Thy1(10nm)
Si-bound
g(r) (normalized density)
L(r)-r (confidence interval)
radius (nm)
radius (nm)

The pair auto-correlation curve derived from many (80) images of gold particles labeling cell surface IgE-FcεRI is typical of all membrane proteins studied, and is shown in Figure 3.2B. We found the shape of this curve to be typical of all membrane components we examined: *G(r)* values trend towards 1 at long radii (r>40 nm) indicating that these gold labels are not correlated at these distances. At very short radii (r<10 nm), *g(r)* values fall below 1 because gold particles cannot pack more tightly than their hard sphere radius and are excluded. The *g(r)* values are greater than 1 for radii between ~10 and ~40 nm, indicating that there is an increased probability of finding pairs of particles separated by these distance than would be expected in a random distribution (*g(r)-1*, dashed line in Figure 3.2B). For example, *g(*20 nm*)* ≈ 4 means that it is roughly four times more likely to find two gold particles separated by 20 nm than is expected from a random distribution. This also means that the average density of gold particles 20 nm away from any given particles if four times greater than the overall average surface density.

Correlation functions for gold particles labeling IgE-FcεRI and other other plasma membrane proteins (Table 3.1) all show significant clustering over short distances (~10 nm <r<~40 nm) as summarized in Figure 3.2C, left panel. In general, we find that the descending curves of the measured correlation functions are well fit by Gaussian line-shapes centered at r=0, with varying amplitude but with relatively constant half-width (10-15 nm). The correlation function for each species deviates from this Gaussian shape at short radii due to the finite size of the gold particles used (either 5 nm or 10

nm). Significant clustering is also evident for all plasma membrane proteins we examined through calculation of *L(r)-r* functions (Eqn 1). For the example of IgE-FcεRI, the curve has a maximum at r~20 nm and *L(r)-r*>1 at r exceeding 100 nm (Figure 3.2C, right panel).

Correlation Functions Provide Advantages over Ripley's Functions.

Several advantages of using correlation functions to quantify SEM data are revealed by comparing the correlation functions and *L(r)-r* functions in Figure 3.2C. Because correlation functions measure increased densities as a function of distance away from an average particle, they provide direct measures of cluster size and particle number. The size of clusters is given by the decay of the curve (i.e., how rapidly *g(r)* decreases with r), and the composition of the average cluster is given by $N = \int_0^\infty (g(r)-1)\rho_{gold} 2\pi r dr$. In contrast, it is more difficult to extract reliable physical properties of domains from Ripley's functions [30]. This is because Ripley's functions are generated by integrating correlation functions (Eqn 1), and therefore short-radius effects are propagated to long radii (e.g., steric limitations of finite sized gold particles).

For an example of some potential problems extracting cluster properties with Ripley's functions, the radius at the maximum of the Ripley's curve is frequently interpreted to be the cluster size [11]. The Ripley's curves peak at radii between 17 and 22 nm for the different proteins we examined, and these values are significantly larger than the radii of clusters obtained by

fitting correlation functions to Gaussian lineshapes (half-width at half-maximum = 8-12 nm; Figure 3.2C, left panel). This is not surprising because the maximum of the Ripley's curve is related to both the size of the gold particle and the size of clusters. This is explicitly demonstrated for the case of Thy-1 where we have obtained images from proteins labeled with both 5 nm and 10 nm gold particles (Figure 3.2C). In this case, the radius of maximum *L(r)-r* value shifts from 15 nm to 20 nm when Thy-1 is labeled with 5 nm and 10 nm particles, respectively. Furthermore, the maximum value of *L(r)-r* vs. r curves is often taken as the relative number of particles per cluster. Comparing the peak values of correlation functions and Ripley's functions for the several proteins we examined (Figure 3.2C) shows that these values do not always trend together (e.g., compare CTxB and Thy-1). Because Ripley's curves are normalized to produce units of statistical confidence intervals, even low levels of clustering in systems with good counting statistics (large average surface densities – see Table 3.1) will produce Ripley's curves with high values, as is the case for CTxB. In contrast, highly clustered objects with poor statistics (low average surface densities) will not appear as clustered. In sum, Ripley's functions provide a useful means to determine the statistical significance of clustering from particle distributions, but it is difficult to extract measures of cluster size and particle number per cluster from this type of analysis.

To assess the significance of clusters of gold particles specifically bound to plasma membrane proteins, we also imaged IgE proteins covalently conjugated to a silicon surface that were labeled with the same primary and

gold-conjugated secondary antibodies. We found that these gold particle distributions are also significantly clustered when their average density is similar to that observed in the cell surface measurements. Just as for cell surface labeled IgE-FcεRI, reconstructed images of gold particles labeling IgE bound to a silicon surface are visually clustered (Figure 3.2A), and both correlation functions and Ripley's functions indicate that clustering is statistically significant (Figure 3.2C). This result raised our concern because it is generally assumed that surface conjugated proteins are randomly distributed, and led us to investigate if the observed clustering is due to multivalent binding of gold particles to single target proteins.

Clustering of Gold is Dominated by Multivalent Labeling.

We surmised that clustering of gold particles is due to either clustering of target proteins on the cell surface (Figure 3.3A), or to multiple gold particles binding to single target proteins through multivalent interactions (Figure 3.3B). To distinguish these two possibilities, we conducted double label experiments and measured cross-correlations between two distinguishable but functionally identical pools of the same protein on the cell surface. In one experiment, two separate pools of FcεRI were created by pre-incubating the cells with a mixture of IgE labeled with either the fluorophore Alexa488 or the fluorophore FITC prior to fixation in our standard procedure. These were distinctively labeled with fluorophore-specific primary antibodies of different species followed by species-specific secondary antibodies conjugated to gold particles of different sizes (Figure 3.3C).

By this scheme, small and large gold particles cannot bind to the same FcεRI protein because only a single IgE antibody binds to each FcεRI protein [31]. If the clustered gold observed for IgE-FcεRI in single label experiments arises from the clustering of multiple FcεRI on the cell surface, then cross-correlation functions in the double label experiment will be similar to the auto-correlation functions obtained in single label experiments (red points in Figure 3.3D). In contrast, we find that cross-correlation functions (black points in Figure 3.3D) indicate random distributions within experimental error bounds ($c(r)$=1). This comparison shows that the appearance of clustering in single label experiments is due to multiple gold particles binding to single target proteins. A similar result is obtained with a mixture of CTxB proteins that are labeled with either Alexa488 or FITC and bind to separate GM_1 gangliosides, prior to cell fixation and gold labeling with distinctive primary and secondary antibodies (Figure 3.3E,F).

Our consistent findings from double label experiments with these two different plasma membrane components (IgE-FcεRI and CTxB-GM_1) suggest the result is general: Clustering observed in single label experiments is dominated by an artifact caused by multiple labels on individual target proteins using the standard immuno-gold labeling procedure. It is usually not practical to perform experiments using this double label scheme, therefore we devised a model to correct single label experiments for artifactual clustering due to multiple binding to single target proteins.

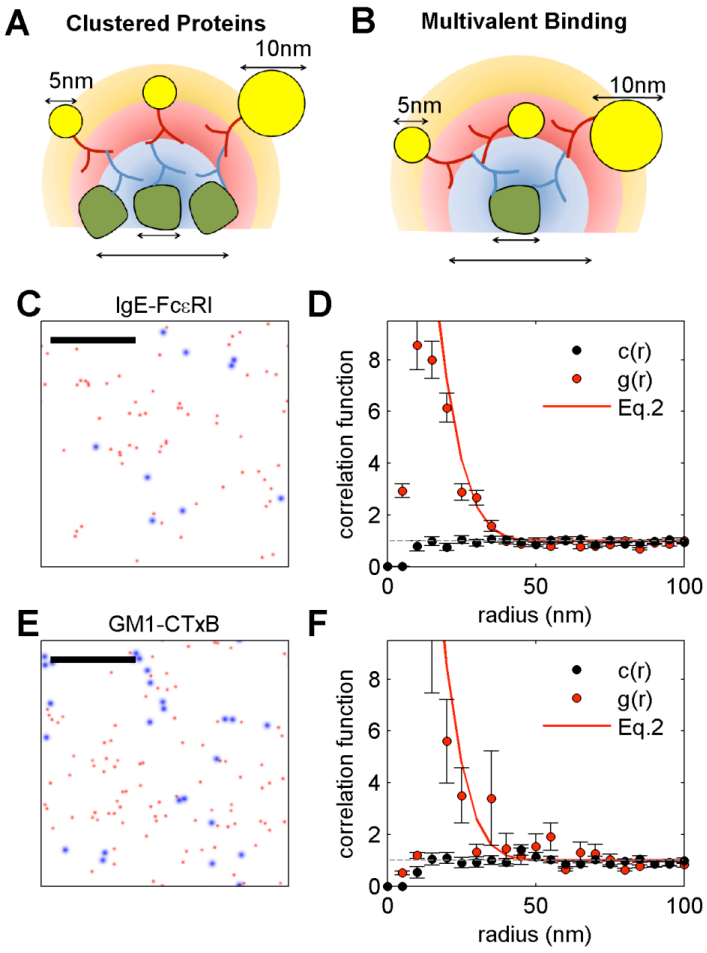

Figure 3.3: Double label experiments verify that apparent IgE-FcεRI and CTxB-GM_1 clustering is due to multiple gold particles labeling single target proteins. Possible models for observed images of clustered gold are that the target proteins are clustered (A), or that multiple gold particles bind to single target proteins through multivalent interactions of labeling antibodies (B). C) Images of A488- or FITC-conjugated IgE-FcεRI that are distinctively immuno-labeled with 5 nm (red) and 10 nm (blue) gold particles, respectively. D) Auto-correlation function of pooled particles (5 nm and 10 nm; red points) indicate clustering of gold particles, and Eqn 3 provides a good fit (red line). The cross-correlation function for the 5 nm vs. 10 nm particles is ~1 at all r (black points), showing no evidence for significant clustering of the target proteins. E, F) The same results are obtained from a similar experiment with A488- and FITC-conjugated CTxB bound to GM_1. Images with distinctive 5 nm (red) and 10 nm (black) immuno-gold labels (E) are evaluated with auto-correlation (red points and line) and cross-correlation (black points) (F).

A Simple Model of Multiple Binding in Single Label Experiments

Our experiments represented by Figure 3.2 show that the gold particles are bound in clusters with descending ($g(r)$>15 nm) curves that can be approximated with Gaussian shaped probability distributions centered at r=0. This means that a gold particle has the highest probability of being located at the center of a target protein, and decreasing probability of being located at positions away from the protein center. Our model assumes that proteins have Gaussian shaped binding surfaces for convenience because the auto-correlation of a Gaussian shape is also a Gaussian with an increased half width $\sqrt{2\sigma}$. If target proteins are represented as delta functions $\delta(\bar{r} - \bar{r}_c)$ located at their centers $\bar{r}_c$ then the correlation function of protein centers will be $\frac{1}{\rho_{avg}}\delta(r) + g'(r > 0)$, where ρ_{avg} is the average surface density of the protein and $g'(r>0)$ describes how the protein is distributed on a surface. In this case the pair auto-correlation function $g(r)$ for the multiply labeling gold particles will take the form:

$$g(r) = \frac{LE}{4\pi\sigma^2\rho_{gold}}\exp\left\{-r^2/4\sigma^2\right\} + \frac{1}{4\pi\sigma^2}\exp\left\{-r^2/4\sigma^2\right\} * g'(r) \qquad (2)$$

where ρ_{gold} is the average surface density of gold particles as defined above, LE is the labeling efficiency (average number of gold particles per target protein), σ is the half-width of the Gaussian-shaped cluster (roughly the radius of the target protein and bound labeling antibodies), and * is a convolution. The first term describes correlations that arise from the individual clusters of multiply

bound gold particles and is inversely proportional to the average surface density of target proteins ($\rho_{avg}=\rho_{gold}/LE$). The second term is independent of ρ_{gold} and is the correlation function of the target proteins ($g'(r>0)$) convoluted (filtered) by the correlation function of the average target protein with its labeling antibodies. This second term is analogous to the correlation function of a fluorescently labeled protein being blurred by the point spread function of an optical microscope. In the special case where the target proteins are randomly distributed, $g'(r>0)=1$ and the second term of Eqn 2 becomes unity:

$$g(r) = \frac{LE}{4\pi\sigma^2\rho_{gold}} \exp\left[-r^2 \Big/ 4\sigma^2\right] + 1 \qquad (3)$$

Below we first demonstrate that all of our experimental results are consistent with this simple model by assuming a random distribution of target proteins (Eqn 3) and obtaining reasonable and consistent values for the parameters LE and σ over a wide range of gold surface densities. Furthermore, we check the assumption of a random distribution of target proteins for experimental cases by evaluating deviations from 1 in the second term of Eqn 2.

We evaluated correlation functions from individual BSD images for each of the labeled membrane proteins, and the descending portion of each of these curves is well fit by Eqn 3 by adjusting the two free parameters of LE and σ. The best fit values for both LE and σ are summarized in Figures 3.4A and 3.4B for each target protein as a function of ρ_{gold}. We find that both parameters are largely independent of ρ_{gold}, and they lie within a close range for different target proteins. Figure 3.4A shows that LE ranges between 0.5

and 2.5 gold particles per cluster (i.e., per target protein) and remains largely constant even when the same target protein is examined over roughly two decades in ρ_{gold}, as is the case for transiently expressed proteins (YFP-GT46, YFP-GPI) where a broad range of surface densities can be examined. Generally, we find larger values for *LE* when smaller gold particles are used (e.g., compare GPI-YFP to IgE). Also, *LE* decreases slightly with increasing ρ_{gold} for the same protein (most evident for YFP-GPI). Both observations are likely due to constraints in the packing of gold particles and the accessibility of binding sites. Figure 3.4B shows that the size of gold particle clusters is remarkably constant over a wide range of expression levels. For most proteins investigated, σ is close to 8 nm. This roughly corresponds to the expected radius of the target protein plus labeling antibodies. Not surprisingly, the σ value obtained depends on the specific labeling scheme: We find smaller clusters in the case of Thy-1, which is labeled with a monoclonal primary antibody, and larger cluster sizes for FcεRI and CTxB where fluorescently modified proteins (IgE or CTxB) present numerous potential binding sites for primary anti-fluorophore antibodies.

In our simple model, deviations of experimental correlation functions from Eqn 3 would indicate clustering of target proteins on the cell surface. Figure 3.4C shows correlation functions that are "corrected" by subtracting the multiple gold binding (first) term of Eqn 3 from experimental correlation functions using the average parameter values from Figure 3.4A-B. We find that these "corrected" correlation functions do not deviate significantly from $g'(r>0)=1$, indicating that the proteins investigated are not significantly

clustered in resting cells within the error bounds of our experiments. Error bounds at large radii are dominated by counting statistics, while errors at short radii are dominated by uncertainty in the size and labeling efficiency of the labeled protein-antibody complexes. A similar conclusion can be drawn by examining Ripley's functions evaluated from correlation functions "corrected" as above and using Eqn 1 (Figure 3.4D). Normalized *L(r)-r* curves do not reach values greater than 1 that would indicate statistically significant clustering.

IgE-FcεRI and Lyn are Significantly Co-clustered.

Even though we find that neither IgE-FcεRI nor Lyn kinase is significantly self-clustered in unstimulated RBL mast cells (Figure 3.4C), we do find significant cross-correlation between transmembrane IgE-FcεRI and Lyn that is anchored to the inner leaflet of the plasma membrane (Figure 3.5). With double label experiments we measured cross-correlation functions between different protein pairs (Figure 3.5A). We find that IgE-FcεRI and the GPI-linked protein Thy-1 are uncorrelated. In contrast, IgE-FcεRI and actin are mildly correlated, and IgE-FcεRI is significantly correlated with its signaling partner Lyn. This observation that IgE-FcεRI and Lyn co-localize more strongly than IgE-FcεRI with itself or with GPI-linked Thy-1 suggests that their interaction is not simply driven predominately by co-association with ordered lipid regions in the plasma membrane, as GPI-linked proteins are known to strongly partition into ordered domains using a variety of different assays.

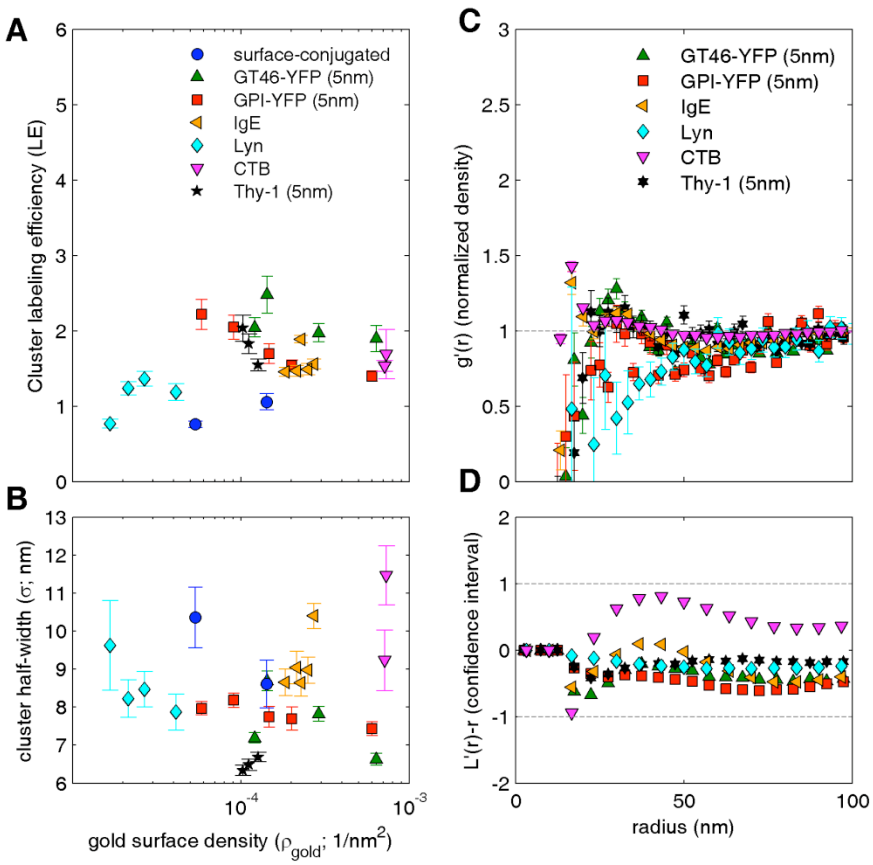

Figure 3.4: Measured single-label correlation functions are well described by a simple model of multiple binding. A, B) Correlation functions evaluated from many images of specified membrane proteins are fit to Eqn 3 to extract parameters: the average number of gold particles per target protein (labeling efficiency, *LE*) (A); half-with (σ) of the target protein as represented by the clustered gold particles (B). These parameters are plotted as a function of the average surface density of gold particles (ρ_{gold}) to test the simplification of Eqn 2 to Eqn 3. Results obtained from images of the same protein with similar gold surface densities are pooled to simplify the presentation, and error bars are extracted from the fitting procedure. C) The residual correlation functions after fitting the points for specified target proteins to Eqn 3 would represent correlations in the target protein distributions given by the second term of Eqn 2 ($g'(r)$). Error bounds denote standard deviations of the measurement and do not include systematic errors that could arise from deviations of the gold binding surface from a Gaussian shape which are likely significant. D) Ripley's *L(r)-r* functions are tabulated from residual correlation functions. *L(r)*-r values are normalized to 95% confidence intervals. Imaging statistics, fit parameters, and average target protein surface densities are reported in Table 3.1.

Measured cross-correlation functions between distinctively labeled FcεRI and Lyn proteins are expected to be the actual cross-correlation function between these two proteins, convoluted (filtered) by the shape of the average gold binding surface, just as in the case of the single label experiments. If we assume that FcεRI-Lyn co-clustering arises from direct binding, then we would expect the true protein-protein cross-correlation function to approximate $c'(r)=1+A\delta(r-r_o)$, where r_o is the distance between protein centers in a bound co-cluster. As long as the distance r_o is smaller than the size of the proteins plus labeling antibodies (σ), then we expect the measured cross-correlation function between 5 nm and 10 nm gold particles labeling FcεRI and Lyn proteins respectively will be as follows:

$$c(r) = 1 + \frac{A}{r\pi\sigma^2}\exp\left[-r^2/4\sigma^2\right] \quad (4)$$

Fitting Eqn 4 to the descending points of the measured FcεRI-Lyn cross-correlation function ($c(r) > 25$ nm) yields $\sigma = 10 \pm 1$ nm (Figure 3.5A). This value for σ is consistent with the combined sizes of FcεRI and Lyn binding surfaces reported in Figure 3.4. Thus, the observed range of cross-correlation of FcεRI and Lyn can be accounted for by the finite size of the antibodies labeling these two proteins that have some tendency to associate, without implying long-range interactions between them.

The integrated intensity of the cross-correlation function is not affected by the finite size of labeling antibodies because the convolution preserves total intensity, and therefore provides information about the stoichiometry of Lyn-

FcεRI co-localization. The average number of FcεRI proteins per cluster is given by $N_{Fc\varepsilon RI} = \rho_{Fc\varepsilon RI} \sum_{0}^{r_{\max}} (c(r) - 1) 2\pi \Delta r$, where *c(r)* is represented by the points measured for FcεRI-Lyn in Figure 3.5A, Δr is the short distance interval between adjacent points, and $\rho_{Fc\varepsilon RI}$ is the average surface density of FcεRI proteins reported in Table 3.1. To minimize errors at large r, we have included *c(r)*-1 points measured over the range of significant correlations (from r=0 through r_{max}=40 nm). This summation yields an average number of FcεRI receptors per cluster, $N_{Fc\varepsilon RI} = 0.44 \pm 0.13$. Because both FcεRI and Lyn are not self-clustered, we deduce that when associated, FcεRI and Lyn bind in a 1:1 complex. This means that there are on average 0.44 of FcεRI receptors per Lyn, or 44% of Lyn proteins are co-clustered with the receptor. If we instead evaluate the number of Lyn proteins per cluster, $N_{Lyn} = \rho_{Lyn} \sum_{0}^{r_{\max}} (c(r) - 1) 2\pi \Delta r = 0.06 \pm 0.02$, then we deduce that 6% of FcεRI proteins are co-clustered with Lyn. These values are reported in Table 3.2

We further investigated the physical basis of IgE-FcεRI and Lyn co-localization by modulating membrane cholesterol concentration using MβCD (Figure 3.5B). We find that co-clustering is moderately decreased when membrane cholesterol is lowered by incubating cells with 10 mM MβCD for 5 min at 37° C prior to fixation and immuno-gold labeling. In contrast, IgE-FcεRI and Lyn co-clustering remains largely unchanged when plasma membrane cholesterol levels are increased by the same treatment with MβCD-cholesterol complexes. The reduction in cross-correlation intensity upon

cholesterol depletion indicates that the effective binding energy between IgE-FcεRI and Lyn proteins is sensitive to membrane cholesterol concentration. The lower binding energy between IgE-FcεRI and Lyn in cholesterol depleted cells results in a reduction in the percentage of FcεRI receptors co-clustered with Lyn (5±2%) and the percentage of Lyn proteins associated with FcεRI receptors (34±14%) (Table 3.2).

3.4 DISCUSSION

Our report describes pair correlation analysis of SEM images and presents two significant findings regarding the lateral organization of plasma membrane proteins in unstimulated RBL mast cells. First, we provide several lines of evidence supporting the conclusion that the self-clustering of gold particles commonly observed in single label electron microscopy experiments is dominated by a labeling artifact of multiple gold particles bound via antibodies to single target proteins. Second, we find significant co-localization of IgE-FcεRI and Lyn kinase in resting cells, which decreases with reduction of plasma membrane cholesterol. The implications of both these findings are discussed below.

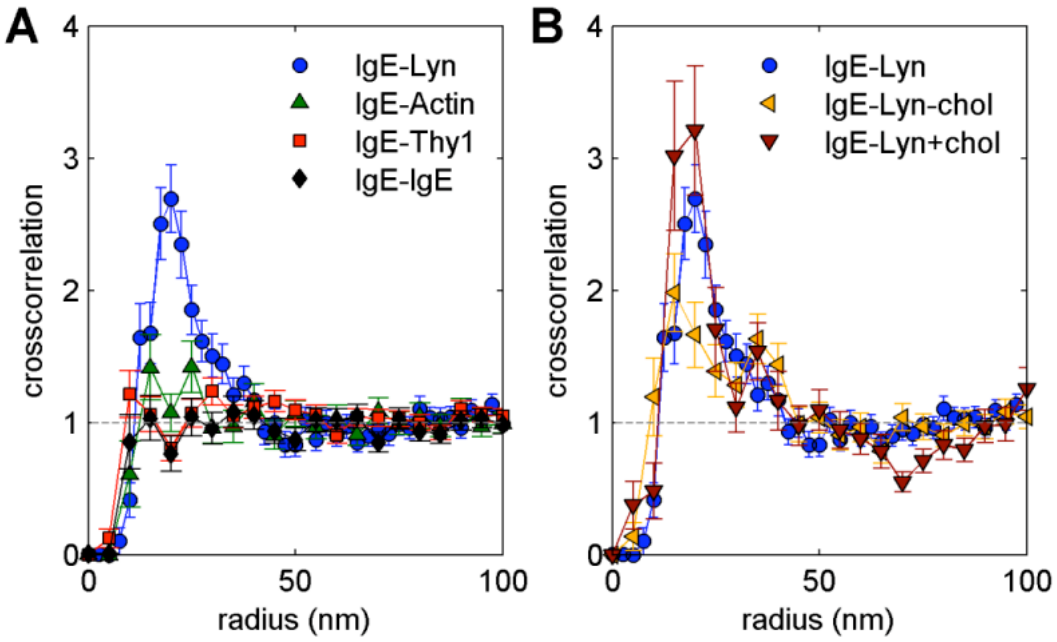

Figure 3.5: IgE-FcεRI and Lyn are significantly co-clustered in resting cells with some dependence on cholesterol. A) Cross-correlation functions between IgE-FcεRI and other specified proteins are evaluated from double label experiments where species were distinguished by differently sized immuno-gold particles. B) Cross-correlation functions evaluated for distinctively labeled FcεRI and Lyn in samples treated with MβCD (or not) as specified to modulate levels of cholesterol. The integral under the cross-correlation curve is related to the number of proteins in co-clusters as reported in Table 3.2. Total areas and particle numbers are also reported in Table 3.2.

Table 3.2: Measurement statistics and FcεRI-Lyn binding ratios from double label experiments. N_{10nm} is the total number of 10 nm gold particles (labeling Lyn) analyzed and N_{5nm} is the total number of 5 nm gold particles (labeling FcεRI) analyzed in double label experiments described in Figure 3.5. The % of Lyn bound to FcεRI and vice versa is determined by measuring cross-correlations between the two proteins and calculating the average number of Lyn and FcεRI in co-clusters.

	N_{10nm}	N_{5nm}	Area (μm^2)	% of Lyn bound to FcεRI	% of FcεRI bound to Lyn
Lyn-FcεRI -Chol	422	5163	24.7	34±14	5±2
Lyn-FcεRI	1053	11632	38.0	44±13	6±2
Lyn-FcεRI +Chol	379	4250	24.7	44±19	6±3

Plasma Membrane Proteins are Not Substantially Self-Clustered in Resting Cells.

We directly demonstrate that immuno-gold particles labeling two distinct membrane proteins (IgE-FcεRI and CTxB-GM_1) are clustered in single label experiments simply because multiple gold particles can bind to single target proteins using the standard labeling strategy of primary and secondary antibodies. Furthermore, we demonstrate that the observed clustering of gold particles labeling a variety of plasma membrane proteins is well described by a minimal model of multiple binding. This same model explains the observed clustering of immuno-gold particles that label proteins covalently conjugated to a silicon surface at a density similar to that of target membrane proteins. Based on this evidence, we conclude that these membrane proteins themselves are not self-clustered within the error bounds and resolution limits inherent in these measurements.

We expect that multiple gold particles binding to single target proteins is a general artifact of standard immuno-gold labeling procedures. In particular, one or both of the primary and secondary antibodies can bind to their target at multiple locations. In this case, we expect gold pair correlation functions to take a form similar to the expression given in Eqns 2 and 3 even when average gold labeling efficiencies are ≤ 1 gold particles per protein. The range of correlations we observe (Figure 3.4B) corresponds to the approximate size of the target proteins plus labeling antibodies (6-12 nm). The magnitude of correlations (Figure 3.2C) is inversely proportional to the surface density of target proteins (25 - 460 proteins/μm^2) (Table 3.1). By including these

expected values for protein density and size into Eqns 2 and 3, it is apparent that multiple gold particles binding to single target proteins can easily dominate measurements of clustering. This is particularly true in resting cells, where correlations between proteins are expected to be subtle and short-ranged. In our current experiments, we cannot rule out that the proteins examined in single label experiments are self-clustered at length-scales below the resolution limit dictated by the size of the target protein plus labeling antibodies (6-12 nm). In our double label experiments, we cannot rule out co-localization with a magnitude less than the sensitivity dictated by our limited counting statistics ($c(r)$<~1.25).

Numerous previous studies have suggested that proteins labeled with immuno-gold particles are organized into discrete nano-clusters in resting cells [7, 9-12, 15-17, 32], and several of the same plasma membrane proteins have been examined in this work. We expect that these previous findings may have overestimated the degree of self-clustering of resting protein distributions, because there was no explicit correction for multivalent gold binding to single target proteins. There are some reported cases where the clustering of gold particles labeling some membrane proteins is altered after cells are exposed to biochemical treatments such as cholesterol depletion or actin destabilization. Based on our proposed model of multivalent gold binding, we would expect that artifactual clustering would be affected by membrane perturbations if they led to changes in the density of target proteins at the cell surface, since the first term of Eqn 2 varies inversely with the average surface density of target proteins. There are some examples where

membrane perturbations have led to altered expression levels of plasma membrane proteins [24]. This same multivalent binding artifact is expected to be present in other super-resolution methods that utilize immuno-labeling (such as STORM and STED). Fortunately, this artifact is easily accounted for when the distance range of protein-protein clustering exceeds this resolution limit imposed by multiple immuno-gold binding. In Chapter Four, we use this method to characterize the large-scale clustering of signaling components in RBL cells after stimulation with multivalent antigen.

IgE-FcεRI-Lyn Interactions Depend on Cholesterol Levels.

We took advantage of the increased sensitivity of cross-correlations to investigate co-clustering between several plasma membrane associated proteins. We find significant cross-correlation between IgE-FcεRI and its signaling partner Lyn, even though IgE-FcεRI and Lyn do not appear to be significantly self-clustered in resting cells. This strongly suggests that FcεRI and Lyn interact primarily through specific protein-protein interactions that are stronger than typical protein-lipid or lipid-lipid interaction energies.

Individual Lyn kinase proteins exist in either active or inactive states in the plasma membrane, and these are dynamically regulated by segregation and recruitment of phosphatases and kinases [2]. When Lyn is in an active state, it is capable of phosphorylating the FcεRI at tyrosine residues in cytoplasmic ITAM sequences [33]. Active Lyn can then bind to a phosphorylated ITAM in the β subunit, accounting for the amplifying function of this subunit [34]. There is also evidence that Lyn binds weakly to the

unphosphorylated β subunit of FcεRI via Lyn's N-terminal unique domain [33, 35-37]. In this transphosphorylation hypothesis, pre-association of FcεRI with Lyn facilitates receptor phosphorylation after clustering by antigen [33].

We find that roughly 40% of Lyn proteins co-localize with FcεRI in resting cells, and that this ratio decreases when cholesterol levels are lowered in the plasma membrane. If co-clustering is due to binding between inactive Lyn and the β subunit of FcεRI, then this implies that the interaction is not weak but strong enough that roughly half of labeled Lyn are associated with receptors over many images. Our results also imply that that the effective binding energy between FcεRI-β and Lyn is somehow modulated by cholesterol levels, either through direct binding of cholesterol to one or both proteins, or through indirect interactions.

Another possibility is that co-clustering is driven by activated Lyn bound to a phosphorylated FcεRI. This would imply that the ~5% of total plasma membrane FcεRI population is phosphorylated in unstimulated cells at a given time, although this state could be short-lived. It is difficult to rule out this small amount of phosphorylation, but we note that the FcεRI-β phosphorylation difference in stimulated compared to unstimulated cells is ~100 fold (see, for example, [24]). This possibility also implies that the magnitude of FcεRI -Lyn co-clustering will be controlled at least in part through the dynamic equilibrium between the active and inactive states of Lyn. It is conceivable that this equilibrium could be shifted by changing membrane cholesterol content through changes in membrane organization.

There is evidence that Lyn proteins localized in ordered lipid regions of the membrane have substantially higher specific activity, and that this arises because Lyn in these regions are sequestered from deactivating phosphatases [38]. If ordered lipid regions are destabilized with cholesterol depletion, then it is possible that the total fraction of active Lyn would decrease and consequently the fraction of total Lyn associated with the receptor would also decrease in a manner consistent with our experimental observations.

Several factors could influence our quantification of FcεRI -Lyn co-clustering. First, it is possible that our labeling scheme preferentially samples a subset of the total target protein being investigated. For example, if our labeling antibodies bind more efficiently to activated Lyn, then we would be overestimating the fraction of total Lyn co-clustered with FcεRI. We also would be overstating co-clustering if we occasionally mistake a Lyn protein for a receptor or vice versa. This could happen either if labeling antibodies do not bind specifically to their target proteins, or if 5 nm and 10 nm are not properly distinguished in our image processing algorithms. Both effects would necessarily lead to overestimates of clustering due to the multiple immuno-gold binding artifact described above. Our significant efforts to minimize possible errors in labeling and particle identification are reflected in the quality of our labeling controls (Figure 3A.1 in Appendix) and the fact that we do not observe artifactual co-clustering in double label experiments of the same target protein, even when individual single labels are significantly clustered (Figure 3.3).

In conclusion, we have demonstrated that quantitative correlation functions are useful for extracting substantial information from electron microscopy studies. Using this analytical method, we clearly demonstrate that self-clustering of gold particles in single label experiments commonly arises from multiple gold-antibody conjugates binding to single target proteins. Furthermore, we show that this method yields reliable values for average surface densities for a variety of plasma membrane proteins, and provides strong evidence that Lyn and FcεRI co-cluster to a quantifiable degree in unstimulated cells. Our analytical approach can be applied to a range of scientific problems that involve quantifying high resolution images obtained by electron microscopy and emerging super-resolution fluorescence microscopy imaging techniques (e.g. STED, PALM, and STORM). Our results, together with work ongoing in other laboratories, make us optimistic that high resolution measurements along with careful quantification will allow the physical basis of heterogeneity in cell plasma membranes to be deciphered.

APPENDIX

Evaluation of Correlation Functions:

Automatic image processing algorithms are employed to identify the location of particle centers as described in the main text, and centers are used to evaluate pair correlation functions. The pair auto-correlation function (*g(r)*) and pair cross-correlation function (*c(r)*) are defined as follows:

$$g(\vec{r}) = \frac{<\rho(\vec{r})\rho(\vec{r}+\vec{R})>}{<\rho(\vec{R})>^2} \text{ and } c(\vec{r}) = \frac{<\rho_1(\vec{r})\rho_2(\vec{r}+\vec{R})>}{<\rho_1(\vec{R})><\rho_2(\vec{R})>}$$

where the angle brackets denote an average is over all positions in the image, and over multiple images. In this study, correlation functions are evaluated using Fast Fourier Transforms (FFTs) to decrease computation times. First, an image I is constructed to have a values of 1 at the location of particle centers and zeros elsewhere. N_G is the number of gold particles in a given image, and A is the area of the image.

$$g(\vec{r}) = \left(\frac{A}{N_G}\right)^2 FFT^{-1}(\left|FFT(I)\right|^2)/Norm$$

The image is padded with zeros to remove correlations due to the periodicity of FFT functions, and the Normalization *Norm* needed to account for the finite size of the image. The Window function W is the same size as I but has the value 1 everywhere, and the FFT is also padded with the same number of zeros as the image I.

$$Norm = FFT^{-1}(\left|FFT(W)\right|^2)$$

Cross-correlation functions are computed from images constructed for each type of gold particle (*I1* and *I2*) in a similar manner:

$$c(\vec{r}) = \left(\frac{A^2}{N_{G1}N_{G2}}\right) FFT^{-1}(FFT(I1)xFFT(I2)^*)/Norm$$

Where N_{G1} and N_{G2} are the number of gold particles of each type, * is a complex conjugate and the Normalization is the same as above for g(r).

Derivations of Correlation Function for an Assembly of Point Particles:

As stated above, the correlation function is defined as:

$$g(\vec{r}) = \frac{<\rho(R)\rho(\vec{r}+R)>}{<\rho(\vec{R})>^2}$$

If the density is for an assembly of point particles, $\rho(\vec{r}) = \sum_{i=1}^{N}\delta(\vec{r}-\vec{r}_i)$, the correlation function becomes:

$$g(\vec{r}) = \left(\frac{A}{N}\right)^2 \frac{1}{A}\int d\vec{R}\sum_{i,j=1}^{N}\delta(\vec{R}-\vec{r}_i)\delta(\vec{r}+\vec{R}-\vec{r}_j)$$

$$g(\vec{r}) = \left(\frac{A}{N}\right)^2 \frac{1}{A}\sum_{i,j=1}^{N}\delta(\vec{r}+\vec{r}_i-\vec{r}_j)$$

$$g(\vec{r}) = \left(\frac{A}{N}\right)^2 \frac{1}{A}\sum_{i=1}^{N}\delta(\vec{r}) + \left(\frac{A}{N}\right)^2 \frac{1}{A}\sum_{i\neq j=1}^{N}\delta(\vec{r}+\vec{r}_i-\vec{r}_j)$$

$$g(\vec{r}) = \left(\frac{A}{N}\right)^2 \frac{N}{A}\delta(\vec{r}) + \left(\frac{A}{N}\right)^2 \frac{1}{A}\sum_{i\neq j=1}^{N}\delta(\vec{r} + \vec{r}_i - \vec{r}_j)$$

$$g(\vec{r}) = \frac{A}{N}\delta(\vec{r}) + g(\vec{r} \neq 0)$$

For the case of a random distribution (white noise) then $g(\vec{r} \neq 0) = 1$, meaning that the correlation function is one everywhere away from the origin. Typically, the correlation value at r=0 is ignored and not plotted.

Correlation Function for a Distribution of Uniformly Shaped Objects:

Replacing our distribution of point particles with the same distribution of finite sized objects is equivalent to convoluting (or filtering) the original distribution of delta functions with the average shape of the objects $(f(\vec{r}))$:

$\rho'(\vec{r}) = \rho(\vec{r}) * f(\vec{r}) = FT^{-1}(FT(\rho(\vec{r}))xFT(f(\vec{r}))$, or

$$FT(\rho'(\vec{r})) = FT(\rho(\vec{r})xFT(f(\vec{r}))$$

g′(r) can be computed from $\rho'(\vec{r})$ using Fourier Transforms (FTs):

$$g'(\vec{r}) = FT^{-1}(\left|FT\rho'(\vec{r})\right|^2)$$

$$g'(\vec{r}) = FT^{-1}(\left|FT(\rho(\vec{r})) \times FT(f(\vec{r}))\right|^2)$$

$$g'(\vec{r}) = FT^{-1}(\left|FT(\rho(\vec{r}))\right|^2 \times \left|FT(f(\vec{r}))\right|^2)$$

$$g'(\vec{r}) = g(\vec{r}) * F(\vec{r})$$

Here, $F(r) = FT^{-1}(|FT(f(\vec{r}))|^2)$ is the autocorrelation of the object shape.

Plugging in g(r) for a distribution of point particles:

$$g'(\vec{r}) = \frac{A}{N}\delta(\vec{r}) * F(\vec{r}) + g(\vec{r} \neq 0) * F(\vec{r})$$

$$g'(\vec{r}) = \frac{A}{N}F(\vec{r}) + g(\vec{r} \neq 0) * F(\vec{r})$$

Correlation Function for a Distribution of Gaussian Shaped Objects:

When objects have Gaussian shapes, then:

$$f(\vec{r}) = \frac{1}{2\pi\sigma^2}e^{-r^2/2\sigma^2} \text{ and } F(\vec{r}) = \frac{1}{4\pi\sigma^2}e^{-r^2/4\sigma^2}.$$

Plugging this into the above equation for g':

$$g'(\vec{r}) = \frac{A}{N}\frac{1}{4\pi\sigma^2}e^{-r^2/4\sigma^2} + g(\vec{r} \neq 0) * \left(\frac{1}{4\pi\sigma^2}e^{-r^2/4\sigma^2}\right).$$

For the case where where $g(\vec{r} \neq 0) = 1$, this is the relation recorded in Equation 2 of the main text.

$$g'(\vec{r}) = \frac{1}{4\pi\sigma^2\rho}e^{-r^2/4\sigma^2} + 1$$

In the more general case where $g(\vec{r} \neq 0) \neq 1$, then $g(\vec{r} \neq 0)$ or the object-object correlation function is convolved or filtered by the Gaussian shape.

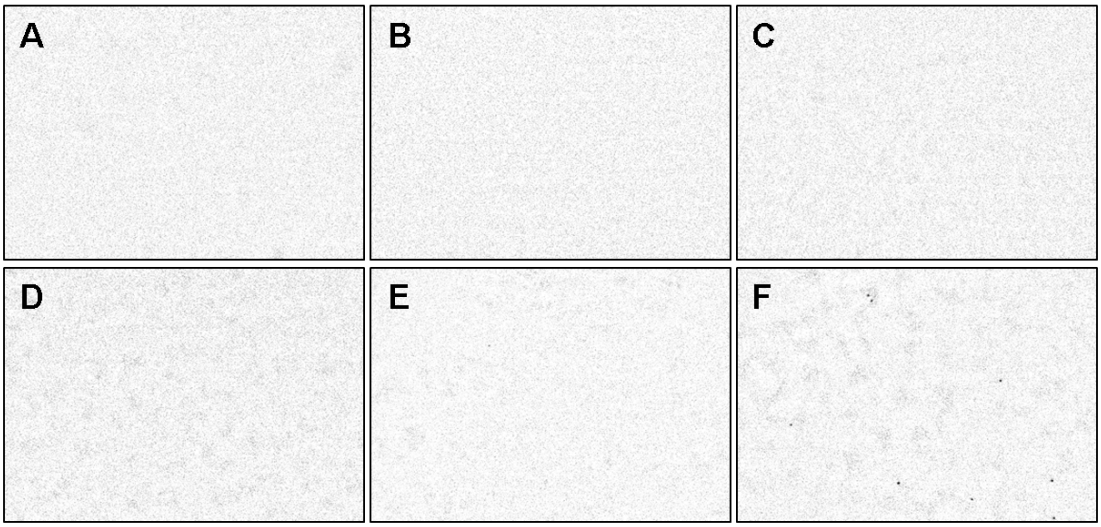

	Sensitized with IgE?	Primary Antibody	Secondary Antibody
A	Yes	None	Goat anti-mouse 10nm gold + 0.1% Tx100
B	Yes	None	Goat anti-mouse 10nm gold + 0.1% Tx100
C	Yes	Rabbit anti-A488 + .01 Tx100	Goat anti-mouse 10nm gold + 0.1% Tx100
D	Yes	Rabbit anti-Lyn + 0.1% Tx100	Goat anti-mouse 10nm gold + 0.1% Tx100
E	Yes	Rabbit anti-Lyn	Goat anti-mouse 10nm gold
F	No	Rabbit anti-Lyn + 0.1% Tx100	Goat anti-mouse 10nm gold + 0.1% Tx100

Figure 3A.1: Gold labeling of proteins is specific. In the absence of specific primary antibodies (A-B), in the absence of A488 on IgE (C), or in the presence of gold-conjugated secondary antibodies with incorrect species specificity (D), there is little to no background gold particle binding. In the absence of 0.1% TX-100, we do not detect gold labeling of inner leaflet proteins (E), and IgE-FcεRI distributions are independent of the presence or absence of TX-100 (not shown). Gold labeling of Lyn is independent of sensitization with IgE (F). Scale bar is 200 nm. Raw BSD images are band pass filtered and inverted for display purposes.

REFERENCES

1. Brown, D.A. and J.K. Rose, *Sorting of GPI-anchored proteins to glycolipid-enriched membrane subdomains during transport to the apical cell surface.* Cell, 1992. **68**(3): p. 533-44.
2. Holowka, D., et al., *Lipid segregation and IgE receptor signaling: a decade of progress.* Biochim Biophys Acta, 2005. **1746**(3): p. 252-9.
3. Simons, K. and E. Ikonen, *Functional rafts in cell membranes.* Nature, 1997. **387**(6633): p. 569-72.
4. Anderson, R.G. and K. Jacobson, *A role for lipid shells in targeting proteins to caveolae, rafts, and other lipid domains.* Science, 2002. **296**(5574): p. 1821-5.
5. Goswami, D., et al., *Nanoclusters of GPI-anchored proteins are formed by cortical actin-driven activity.* Cell, 2008. **135**(6): p. 1085-97.
6. Lingwood, D. and K. Simons, *Lipid rafts as a membrane-organizing principle.* Science, 2010. **327**(5961): p. 46-50.
7. Fujita, A., et al., *Gangliosides GM1 and GM3 in the living cell membrane form clusters susceptible to cholesterol depletion and chilling.* Mol Biol Cell, 2007. **18**(6): p. 2112-22.
8. Heneberg, P., et al., *Topography of plasma membrane microdomains and its consequences for mast cell signaling.* Eur J Immunol, 2006. **36**(10): p. 2795-806.
9. Hess, S.T., et al., *Quantitative electron microscopy and fluorescence spectroscopy of the membrane distribution of influenza hemagglutinin.* J Cell Biol, 2005. **169**(6): p. 965-76.

10. Lillemeier, B.F., et al., *TCR and Lat are expressed on separate protein islands on T cell membranes and concatenate during activation.* Nat Immunol, 2010. **11**(1): p. 90-6.

11. Plowman, S.J., et al., *H-ras, K-ras, and inner plasma membrane raft proteins operate in nanoclusters with differential dependence on the actin cytoskeleton.* Proc Natl Acad Sci U S A, 2005. **102**(43): p. 15500-5.

12. Prior, I.A., et al., *Direct visualization of Ras proteins in spatially distinct cell surface microdomains.* J Cell Biol, 2003. **160**(2): p. 165-70.

13. Seagrave, J., et al., *Relationship of IgE receptor topography to secretion in RBL-2H3 mast cells.* J Cell Physiol, 1991. **148**(1): p. 139-51.

14. Stump, R.F., et al., *Mapping gold-labeled IgE receptors on mast cells by scanning electron microscopy: receptor distributions revealed by silver enhancement, backscattered electron imaging, and digital image analysis.* J Histochem Cytochem, 1988. **36**(5): p. 493-502.

15. Wilson, B.S., J.R. Pfeiffer, and J.M. Oliver, *Observing FcepsilonRI signaling from the inside of the mast cell membrane.* J Cell Biol, 2000. **149**(5): p. 1131-42.

16. Wilson, B.S., et al., *High resolution mapping of mast cell membranes reveals primary and secondary domains of Fc(epsilon)RI and LAT.* J Cell Biol, 2001. **154**(3): p. 645-58.

17. Wilson, B.S., et al., *Markers for detergent-resistant lipid rafts occupy distinct and dynamic domains in native membranes.* Mol Biol Cell, 2004. **15**(6): p. 2580-92.

18. Sanan, D.A. and R.G. Anderson, *Simultaneous visualization of LDL receptor distribution and clathrin lattices on membranes torn from the upper surface of cultured cells.* J Histochem Cytochem, 1991. **39**(8): p. 1017-24.

19. Hancock, J.F., *Lipid rafts: contentious only from simplistic standpoints.* Nat Rev Mol Cell Biol, 2006. **7**(6): p. 456-62.

20. Mayor, S. and M. Rao, *Rafts: scale-dependent, active lipid organization at the cell surface.* Traffic, 2004. **5**(4): p. 231-40.

21. Tian, T., et al., *Plasma membrane nanoswitches generate high-fidelity Ras signal transduction.* Nat Cell Biol, 2007. **9**(8): p. 905-14.

22. Gidwani, A., et al., *Disruption of lipid order by short-chain ceramides correlates with inhibition of phospholipase D and downstream signaling by FcepsilonRI.* J Cell Sci, 2003. **116**(Pt 15): p. 3177-87.

23. Sengupta, P., D. Holowka, and B. Baird, *Fluorescence resonance energy transfer between lipid probes detects nanoscopic heterogeneity in the plasma membrane of live cells.* Biophys J, 2007. **92**(10): p. 3564-74.

24. Sheets, E.D., D. Holowka, and B. Baird, *Critical role for cholesterol in Lyn-mediated tyrosine phosphorylation of FcepsilonRI and their association with detergent-resistant membranes.* J Cell Biol, 1999. **145**(4): p. 877-87.

25. Gosse, J.A., et al., *Transmembrane sequences are determinants of immunoreceptor signaling.* J Immunol, 2005. **175**(4): p. 2123-31.

26. Larson, D.R., et al., *Temporally resolved interactions between antigen-stimulated IgE receptors and Lyn kinase on living cells.* J Cell Biol, 2005. **171**(3): p. 527-36.

27. Zacharias, D.A., et al., *Partitioning of lipid-modified monomeric GFPs into membrane microdomains of live cells.* Science, 2002. **296**(5569): p. 913-6.

28. Sengupta, P., et al., *Structural determinants for partitioning of lipids and proteins between coexisting fluid phases in giant plasma membrane vesicles.* Biochim Biophys Acta, 2008. **1778**(1): p. 20-32.

29. Wu, M., et al., *Visualization of plasma membrane compartmentalization with patterned lipid bilayers.* Proc Natl Acad Sci U S A, 2004. **101**(38): p. 13798-803.

30. Kiskowski, M.A., J.F. Hancock, and A.K. Kenworthy, *On the use of Ripley's K-function and its derivatives to analyze domain size.* Biophys J, 2009. **97**(4): p. 1095-103.

31. Mendoza, G. and H. Metzger, *Distribution and valency of receptor for IgE on rodent mast cells and related tumour cells.* Nature, 1976. **264**(5586): p. 548-50.

32. Fujita, A., J. Cheng, and T. Fujimoto, *Segregation of GM1 and GM3 clusters in the cell membrane depends on the intact actin cytoskeleton.* Biochim Biophys Acta, 2009. **1791**(5): p. 388-96.

33. Pribluda, V.S., C. Pribluda, and H. Metzger, *Transphosphorylation as the mechanism by which the high-affinity receptor for IgE is phosphorylated upon aggregation.* Proc Natl Acad Sci U S A, 1994. **91**(23): p. 11246-50.

34. Dombrowicz, D., et al., *Allergy-associated FcRbeta is a molecular amplifier of IgE- and IgG-mediated in vivo responses.* Immunity, 1998. **8**(4): p. 517-29.

35. Vonakis, B.M., et al., *Interaction between the unphosphorylated receptor with high affinity for IgE and Lyn kinase.* J Biol Chem, 2001. **276**(2): p. 1041-50.

36. Yamashita, T., S.Y. Mao, and H. Metzger, *Aggregation of the high-affinity IgE receptor and enhanced activity of p53/56lyn protein-tyrosine kinase.* Proc Natl Acad Sci U S A, 1994. **91**(23): p. 11251-5.

37. Vonakis, B.M., et al., *Regulation of rat basophilic leukemia-2H3 mast cell secretion by a constitutive Lyn kinase interaction with the high affinity IgE receptor (Fc epsilon RI).* J Immunol, 2005. **175**(7): p. 4543-54.

38. Young, R.M., D. Holowka, and B. Baird, *A lipid raft environment enhances Lyn kinase activity by protecting the active site tyrosine from dephosphorylation.* J Biol Chem, 2003. **278**(23): p. 20746-52.

39. Young, R.M., et al., *Reconstitution of regulated phosphorylation of FcepsilonRI by a lipid raft-excluded protein-tyrosine phosphatase.* J Biol Chem, 2005. **280**(2): p. 1230-5.

CHAPTER FOUR

Quantitative Nano-scale Analysis of IgE-FcεRI Clustering and Coupling to Intracellular Signaling Proteins*

Summary

We use high resolution scanning electron microscopy (SEM) to visualize inner and outer leaflet gold-labeled IgE-FcεRI, Lyn, Syk, and LAT on the top surface of intact RBL-2H3 cells before and after stimulation with multivalent antigen at 37˚C. Previous studies using ripped-off plasma membrane sheets have reported that each of these signaling proteins are self-clustered prior to stimulation and redistribute into large domains (~100 nm in size) after 1-2 min stimulation with multivalent antigen at 37˚C. However, interpretation of these results has been challenging due to 1) recent findings that suggest protein self-clustering is an artifact of gold labeling, 2) new sample preparations that do not require detachment of the plasma membrane from its underlying cytoskeleton, 3) conflicting reports on the physical basis for interactions between IgE-FcεRI and its associated signaling partners, and 4) new analytical tools that better describe cluster properties. Here we demonstrate the ability to detect inner and outer leaflet gold-labeled proteins, as well as membrane structure, in intact cells using a combination of secondary electron detection (SED) and backscattered detection (BSD) SEM.

* This work was done in collaboration with Sarah Veatch, who developed the computational and statistical tools necessary to accurately and robustly quantify gold-labeled protein distributions.

We use measured pair auto- and cross-correlation functions to report useful protein cluster properties such as the average number of proteins per cluster and cluster size. We find that IgE-FcεRI, Lyn, Syk, and LAT are unclustered in unstimulated cells and redistribute into large clusters (after 1 min stimulation) that decrease in size over a stimulation time-course (5, 10, and 20 min). We also find that IgE-FcεRI and Lyn co-redistribute within the same clusters after 1 min of stimulation with sustained co-clustering at long stimulation times. Lastly, we demonstrate that both plasma membrane cholesterol levels and Src tyrosine kinase-dependent protein-protein interactions contribute to IgE-FcεRI and Lyn interactions, and we conclude that these interactions contribute to early IgE-mediated signaling events. These experimental and analytical methods provide new tools to map the nano-scale lateral organization of plasma membrane proteins, as well as probe the physical and functional basis of protein nano- and microdomains involved in immune cell signaling.

4.1 INTRODUCTION

Crosslinking of IgE bound to its high affinity IgE receptor, FcεRI, by multivalent antigen initiates a tyrosine kinase signaling cascade in mast cells that activates more downstream signaling processes, including Ca^{2+} mobilization and exocytosis of secretory granules containing histamine and other mediators of the allergic response [1]. In response to IgE-FcεRI crosslinking, the Src family kinase Lyn rapidly phosphorylates immunoreceptor tyrosine-based activation motifs (ITAMs) on the β and γ subunits of FcεRI. These provide docking sites for the recruitment of Lyn and

Syk, respectfully, which facilitate Syk kinase activation and consequent signal propagation [2, 3]. Although receptor phosphorylation by Lyn is well established as the first detectable biochemical event following receptor aggregation [4, 5], the structural basis for interactions that facilitate this process at the plasma membrane are only partly understood [6, 7].

Interactions between FcεRI and Lyn have been detected biochemically in several different studies, and a two-hybrid study provided evidence that the unique domain of Lyn kinase can bind weakly to the cytoplasmic segment of FcεRIβ in the absence of receptor phosphorylation [8-10]. Previous studies have also established that the SH2 domain of Lyn can bind to the phosphorylated ITAM of FcεRIβ to amplify FcεRI signaling [11-13]. In addition, crosslink-dependent association of IgE-FcεRI with detergent-resistant membranes (DRMs) has been shown to mediate the initiation of the tyrosine phosphorylation cascade by active Lyn in these cholesterol-dependent membrane domains that are characterized by lipids with ordered acyl chains [14-16].

Despite this biochemical evidence for antigen-dependent interactions between Lyn and FcεRI, it has been difficult to detect co-redistribution of Lyn with clustered IgE-FcεRI using confocal fluorescence microscopy under standard conditions for cell activation [17, 18]. Fluorescence cross-correlation spectroscopy, as well as IgE-FcεRI engagement with patterned ligands, reveal stimulated interaction between Lyn and IgE-FcεRI that are dependent on F-actin polymerization, but this occurs on a time-scale that is slower than the

initiation of the tyrosine phosphorylation cascade [18, 19]. Similarly, interactions between IgE-FcεRI and Syk or the key adaptor protein, LAT [20], have been difficult to detect by fluorescence imaging methods under physiologically relevant conditions of antigen stimulation [21].

Nanometer-scale resolution is needed to further elucidate these interactions. Until recently, optical resolution of sub-micron protein heterogeneity has been limited by the wavelength of light; higher resolution imaging has depended primarily on the use of electron microscopy to visualize gold-labeled protein distributions. Early studies from the Oliver laboratory used scanning electron microscopy (SEM) with backscatter detection (BSD) of immuno-gold labeled particles to characterize the time dependent clustering of IgE-FcεRI in response to IgE-specific crosslinking on intact, RBL mast cells [22, 23]. More recently, Wilson, Oliver, and colleagues have used transmission electron microscopic analysis of ripped-off plasma membrane sheets from these same cells to characterize changes in the distributions of outer and inner leaflet proteins in response to IgE-FcεRI crosslinking [24, 25]. Based on Ripley's K Function analysis, they report that IgE-FcεRI, Lyn, Syk, and LAT are self-clustered in these membrane sheets (derived from unstimulated cells) and redistribute into larger clusters that only partly overlap in response to IgE-FcεRI crosslinking by antigen.

Here, we visualize gold-labeled antibodies bound to IgE-FcεRI and other proteins at both the outer and inner leaflets of the plasma membrane of the dorsal surface of intact RBL mast cells with nanometer resolution using

secondary electron detection (SED) to image cell surface topology, together with BSD to image gold particle distributions. By quantifying measured gold particle distributions with pair auto- and cross-correlation functions, we extract useful physical properties to describe protein clusters in the membrane, including average number of proteins per cluster and cluster size. Using this approach, we find that IgE-FcεRI, Lyn, Syk, and LAT are unclustered in unstimulated cells but redistribute into large domains within 1 min of stimulation by multivalent antigen at 37˚C. Cluster size is maximal after 1 min of stimulation, and gradually decreases by 20 min of stimulation due to receptor internalization. We further demonstrate that IgE-FcεRI and Lyn co-redistribute within the same clusters after 1 min of stimulation and remain co-clustered at long stimulation times. Importantly, we show that clustering of Lyn with IgE-FcεRI depends on cholesterol and tyrosine kinase activity, indicating roles for both membrane lipid composition and kinase-dependent protein-protein interactions during early cell signaling events. These new experimental and analytical approaches provide new insights into the interactions of important signaling proteins and the role of plasma membrane structure during the earliest steps of immune cell signaling.

4.2 MATERIALS and METHODS

Chemicals and Reagents:

Rabbit anti-Alexa Fluor 488 (A488) was purchased from Invitrogen (Eugene, OR). Rabbit anti-LAT was purchased from Upstate Biotechnology (Lake Placid, NY). Mouse anti-Lyn (H-6), rabbit anti-Lyn (44), and rabbit anti-Syk

(N-19) were purchased from Santa Cruz Biotechnology (Santa Cruz, CA). Mouse mAb OX-7 (anti-Thy-1) was purchased from BDPharmingen (San Diego, CA). Glutaraldehyde (25% stock) was purchased from Ted Pella (Redding, CA). Paraformaldeyde was purchased from Electron Microscopy Services (Hatfield, PA). Mouse anti-FITC, 3-Aminopropyltriethoxysilane (APTES), 10 nm gold-conjugated anti-rabbit IgG (whole molecule), 10 nm gold-conjugated anti-mouse IgG (whole molecule), and methyl-β-cyclodextran (MβCD) were purchased from Sigma (St. Louis, MO). 10 nm gold-conjugated anti-mouse IgG (whole molecule) was purchased from GE Healthcare (Piscataway, NJ). Protein Phosphatase 1 (PP1) was purchased from Biomol (Plymouth Meeting, PA). A488-IgE was prepared by modification of purified mouse monoclonal anti-2,4-dinitrophenyl (DNP) IgE with Alexafluor 488 (Invitrogen) as previously described [14, 18].

Cell Culture and SEM Sample Preparation:

RBL-2H3 mast cells were grown overnight to ~50% confluency on 2 mm x 2 mm silicon chips at 37˚C under standard cell culture conditions [19] and high affinity IgE receptors (FcεRI) were labeled with A488-IgE (1μg/mL) for 2-3 hrs prior to the experiment. To stimulate cells, IgE-FcεRI was crosslinked with multivalent antigen (DNP-BSA, 1μg/mL) at 37 ˚C in culture medium for specified times, washed quickly in phosphate buffered saline (PBS), and immediately fixed in 4% (w/v) paraformaldehyde and 0.1% (w/v) gluteraldehyde for 10 min at room temperature in PBS. For some experiments, cells were pre-incubated for 5 min at 37˚ C with either 10 mM

MβCD or 4 μM PP1 prior to addition of antigen. Fixed cell samples were washed in blocking solution (2 mg/mL BSA and 2% (v/v) fish gelatin in PBS) and labeled sequentially with primary antibody and secondary antibody-gold conjugates (5 or 10 nm diameter) in the presence (usual) or absence (control) of 0.1% Triton X-100 (TX-100) in blocking solution for 1 hr at room temperature. Cell samples were washed in blocking solution after incubation with the primary antibody, as well as after incubation with the secondary antibody-gold conjugates. For labeling with two differently sized gold particles, samples were labeled first with 10 nm and then 5 nm gold antibody conjugates. The immuno-gold labeled cell samples were further fixed in 4% paraformaldehyde and 1% glutaraldehyde for 5 min at room temperature, and then thoroughly washed in distilled water. Following dehydration through a series of graded ethanol washing steps, samples were critical point dried, mounted on round aluminum SEM stubs, and sputtered with carbon to prevent charging.

Electron Microscopy and Imaging Statistics:

Mounted samples were imaged with a Schottky field emission scanning electron microscope (LEO 1550) at 20KeV. The dorsal (top) surfaces of intact, adherent cells were imaged using secondary electron detection (SED) and backscattered detection (BSD) at high magnification. Flat membrane regions were selected for imaging. For single label experiments, 10 nm gold particles were used, and individual micrographs were obtained at 35K magnification, typically imaging 2.4 μm^2 of the cell surface. For double label experiments, 10

and 5 nm gold particles were used, and micrographs were obtained at 75K-100K magnification. Gold-labeled protein distributions for many different cells and many experiments were obtained for all experimental conditions presented. The total number of gold particles and gold-labeled densities for samples analyzed in this study are summarized in Table 4.1.

Automated Image Processing and Pair Correlation Function Analysis:

The locations of gold particle centers are identified from raw BSD-SEM images using automated image processing algorithms that are described in Chapter Three. In single label experiments, pair auto-correlation functions, $g(\vec{r})$, are evaluated according to the relation:

$$g(\vec{r}) = \frac{\left\langle \rho(\vec{r})\rho(\vec{r}+\vec{R}) \right\rangle}{\left\langle \rho(\vec{R}) \right\rangle^2},$$

where $\rho(\vec{r})$ is the density at position $\vec{r}$, and the ensemble average is over all positions in the image (all $\vec{R}$) as well as over multiple images. In double label experiments, two differently sized particles are resolved, and the pair cross-correlation function, $c(\vec{r})$, is evaluated:

$$c(\vec{r}) = \frac{\left\langle \rho_1(\vec{r})\rho_2(\vec{r}+\vec{R}) \right\rangle}{\left\langle \rho_1(\vec{R}) \right\rangle \left\langle \rho_2(\vec{R}) \right\rangle}$$

where $\rho_1(\vec{r})$ and $\rho_2(\vec{r})$ are the densities of the two distinguishable labels. Since there is no preferred direction, we further average over all angles to obtain *g(r)* and *c(r)*. By this definition, correlation functions quantify the probability of finding a second particle a distance *r* away from a given particle and a value of 1 indicates that particles are randomly distributed at that distance. This

probability, *g(r)*, can be converted to an average density of gold particles within a ring of radius *r* and width *dr* from a given particle by multiplying by the gold particle density averaged over all images, such that:

$$\vec{\rho}_{gold} = \left\langle \rho(\vec{R}) \right\rangle \rho_{gold} = \left\langle \rho(\vec{R}) \right\rangle$$

We recently documented that clustered gold particle distributions in unstimulated cells using our labeling protocols arise primarily from multiple binding sites for gold-antibody conjugates on a single target protein (Chapter Three). In stimulated cells, we correct for this multiple binding artifact by subtracting expected contributions from multiple binding. One benefit of properly characterizing this artifact is that we determine the labeling efficiency (*LE* = the average number of gold particles per accessible protein) and the approximate size and shape of the binding surface (well fit by a Gaussian function). The size of the binding surface is greater than the image pixel resolution and depends on the size of target proteins and the valency of labeling antibodies (typically half-widths are 5-9 nm). The finite size of the binding surface limits our true lateral resolution because the center of a gold particle is not necessarily the center of the target protein. As a consequence we fit correlation curves to single filtered exponentials with

$g(r) = 1 + A\exp\left\{-r/\xi\right\}$ for r >20 nm.

The amplitude of that value for r is related to the increased density of proteins within clusters and the correlation length (ξ) characterizes the size (radius) of protein-rich clusters. The average number of proteins per cluster is given by: $N = \rho_{avg} \int_0^\infty (g(r) - 1) \times 2\pi r dr \approx 2\pi A \xi^2 \rho_{avg}$

Table 4.1: Summary of gold particle analysis. An extensive dataset of cell membrane-bound gold particles is used to compute the correlation functions presented in this study. N_{tot} is the total number, and ρ_{gold} is the average density of gold particles identified for each experimental condition. Note that the protein density reported in Figure 4.4 (ρ_{avg}) is not equivalent to the gold density (ρ_{gold}) shown here due to multiple gold binding to single target proteins as described in Materials and Methods. Typically, labeling efficiency is reduced in double labeling experiments, especially for the 10 nm gold, which labels Lyn in these studies.

	-Ag		+Ag 1 min		+Ag 5min		+Ag 10 min		+Ag 20 min	
Single label	N_{tot}	ρ_{gold} ($N/\mu m^2$)	N_{tot}	ρ_{gold} ($N/\mu m^2$)	N_{tot}	ρ_{gold} ($N/\mu m^2$)	N_{tot}	ρ_{gold} ($N/\mu m^2$)	N_{tot}	ρ_{gold} ($N/\mu m^2$)
IgE-FcεRI (10nm)	185054	281	105159	138	23979	155	13331	86	3430	26
Lyn (10nm)	10558	30	23664	28	2180	30	5419	27	4200	25
Syk (10nm)	9500	29	14874	32	4240	33	1816	8	2454	10
LAT (10nm)	6556	19	7240	20	2982	17	3963	16	2394	12
Double label										
IgE-FcεRI (5nm)	11632	214	7966	7966	1566	80	297	42	230	20
Lyn (10nm)	1053	19	991	991	356	18	42	6	96	9

where ρ_{avg} is the average protein density $\left(\vec{\rho}_{gold}/LE\right)$. We define the increased protein density in clusters to be:

$$\rho_{cl}/\rho_{avg} = N/\pi\xi^2\rho_{gold} \approx 2A.$$

Labeling Controls:

We previously demonstrated the specificity of our primary and gold conjugated secondary antibody reagents and procedures with labeling controls in Chapter Three. Briefly, gold labeling of A488-IgE-FcεRI, Lyn, Syk, and LAT are observed only in the presence of specific primary antibodies and species-specific gold-secondary antibody conjugates. In the absence of 0.1% TX-100 we do not detect gold labeling of inner leaflet proteins, and we determined that IgE-FcεRI distributions are independent of the presence or absence of TX-100 during the labeling step. We also confirmed that gold labeling of Lyn is independent of whether or not cells are sensitized with IgE. We showed for IgE-FcεRI that gold particle distributions in unstimulated and stimulated cells are independent of both the type of primary antibody and gold particle size on the secondary antibody. Similarly, we compared labeling of Lyn with either monoclonal or polyclonal anti-Lyn antibodies followed by species-specific secondary gold antibody conjugates, and found them to be similar (Chapter Three).

4.3 RESULTS

Visualizing Plasma Membrane Lateral Heterogeneity by SEM.

We directly visualize membrane topography and protein heterogeneity on the dorsal surface of intact RBL cells using high resolution SEM with both secondary electron detection (SED) and backscattered detection (BSD) as illustrated in Figure 4.1. SED is sensitive to topography and allows identification of flat cell surfaces to avoid membrane structures that can alter protein organization (compare Figures 4.1B and 4.1C). Cell surface protein distributions are determined by imaging distributions of specific gold labels with BSD at high magnification. Automated image processing and gold particle identification algorithms are used to determine particle coordinates for reconstructed images, as described in Chapter Three and Materials and Methods, and illustrated in Figures 4.1E-G.

Our SEM method can detect both outer and inner leaflet gold-labeled proteins following fixation with 4% paraformaldehyde and 0.1% glutaraldehye and labeling in the presence of TX-100. Plasma membrane-associated proteins are specifically labeled with primary antibodies followed by secondary gold-conjugated antibodies, and little to no background binding occurs on the bare silicon surface (Figure 4.1D). Sample preparation and controls are described in Materials and Methods.

Figure 4.1 shows reconstructed SEM images that specify cell surface distributions of 10 nm gold-labeled IgE-FcεRI. For efficient labeling post-

fixation, we use A488-conjugated IgE pre-bound to FcεRI and rabbit anti-Alexa488 antibody as the primary antibody. We find average surface densities (ρ_{gold}) of ~280 gold particles/μm^2 (Table 4.1). This value is consistent with previous measurements of FcεRI surface density in live RBL cells [26] and indicates a high average labeling efficiency (*LE*) of about 1 gold particle per IgE-FcεRI (see also Chapter Three).

Protein Redistribution during Signaling

To probe the lateral organization of IgE-FcεRI and other proteins implicated in early signaling events, we imaged the distributions of IgE-FcεRI, Lyn kinase, Syk kinase, and LAT before and after stimulation with multivalent antigen at 37˚C (Figure 4.2A). The transmembrane receptor complex A488-IgE-FcεRI was labeled with rabbit anti-A488 and gold-conjugated goat anti-rabbit antibodies on the extracellular dorsal surface. The signaling proteins Lyn, Syk, and LAT were labeled with antibodies specific for cytoplasmic epitopes at the same dorsal membrane. As represented by single label images in Figure 4.2A (left panel), immuno-gold labeled IgE-FcεRI, Lyn, Syk, and LAT appear to be distributed in small clusters at the plasma membrane in unstimulated cells. In Chapter Three we showed that the clustered appearance of protein distributions in unstimulated cells is explained by multiple gold particles binding to single target proteins. With an average labeling efficiency of ~1, statistical variation of none to several particles per protein is expected; we correct for this artifactual clustering in our analysis of protein distributions using a simple model described in Chapter Three.

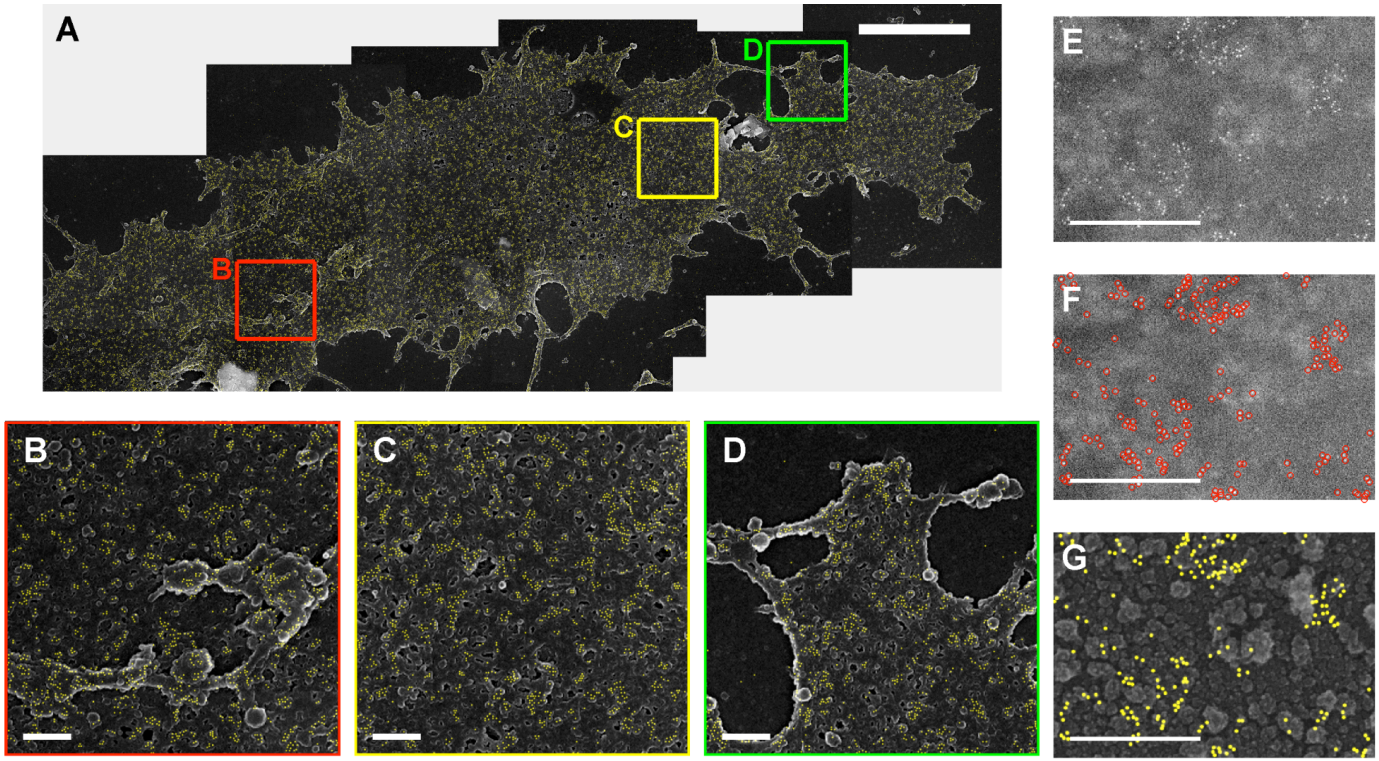

Figure 4.1. Cell surface topology and immuno-gold distribution is visualized with SEM. A) Composite SED image of the dorsal surface on intact RBL cells. Immuno-gold particles (10 nm) labeling FcεRI-IgE are superimposed in yellow; particle centers are determined using BSD in conjunction with automated image processing. Images are acquired at 15K magnification, and scale bar is 5 μm. B-D) Higher magnification images from (A) in areas indicated; scale bars are 500 nm. E-G) SEM images are acquired at higher magnification (35K) for increased lateral resolution and for automated identification of gold particle locations; scale bars are 500 nm. E) Raw BSD image. F) Gold particle centers identified from BSD micrographs with automated image processing. G) Reconstructed particle centers overlaid on SED image. Apparent topology in (E-G) arises from carbon coating and is uncorrelated with gold distributions.

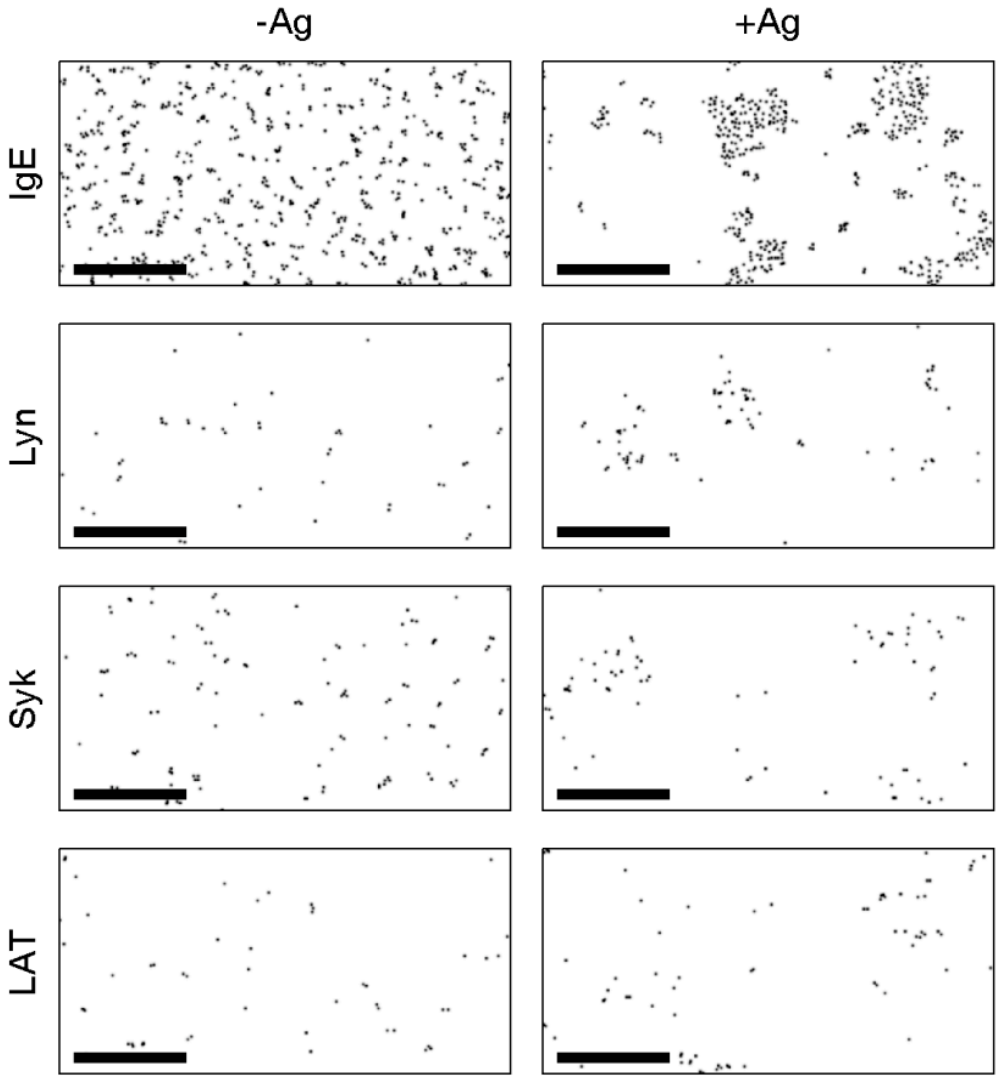

Figure 4.2: IgE-FcεRI, Lyn, Syk, and LAT rapidly redistribute into large clusters after addition of antigen to crosslink IgE-FcεRI. Representative reconstructed BSD-SEM images of plasma membrane with immuno-gold labeling of specified target proteins (10 nm gold particles). Left panels: SEM samples prepared from cells incubated at 37° C in the absence of stimulus; right panels: SEM images prepared from cells stimulated with multivalent antigen for 1 min at 37° C. Scale bars are 500 nm.

Following cell stimulation by antigen crosslinking for 1 min, labeled IgE-FcεRI complexes appear to be tightly packed within large (~100 nm) membrane clusters, consistent with previous SEM studies [23]. Interestingly, the signaling proteins Lyn, Syk, and LAT also redistribute into clusters of similar dimensions shortly after antigen stimulation, and these clusters are similar in appearance to those formed by IgE-FcεRI (Figure 4.2, right panel). Many images of the single label protein distributions for samples represented in Figure 4.2, and also for longer stimulation times (5, 10, and 20 min), were evaluated with pair auto-correlations functions *g(r)* to quantify the protein distributions (Figure 4.3).

In brief, *g(r)* quantifies the probability of finding a second labeled protein a distance r (radius) away from a given protein with the same label. *G(r)* values of 1 indicate that proteins are randomly distributed, and values greater than 1 indicate that proteins are clustered at that corresponding radius value. The magnitude of the *g(r)* value is a measure of clustering of the labeled proteins. For example, *g*(20 nm)=5 means that it is five times more likely to find two particles separated by a distance of 20 nm than is expected from a random distribution. This method of quantifying particle clustering over many individual images is independent of protein expression levels (Chapter Three), and it has distinct advantages over other, more commonly used methods, such as the modified Ripley's function (see Discussion).

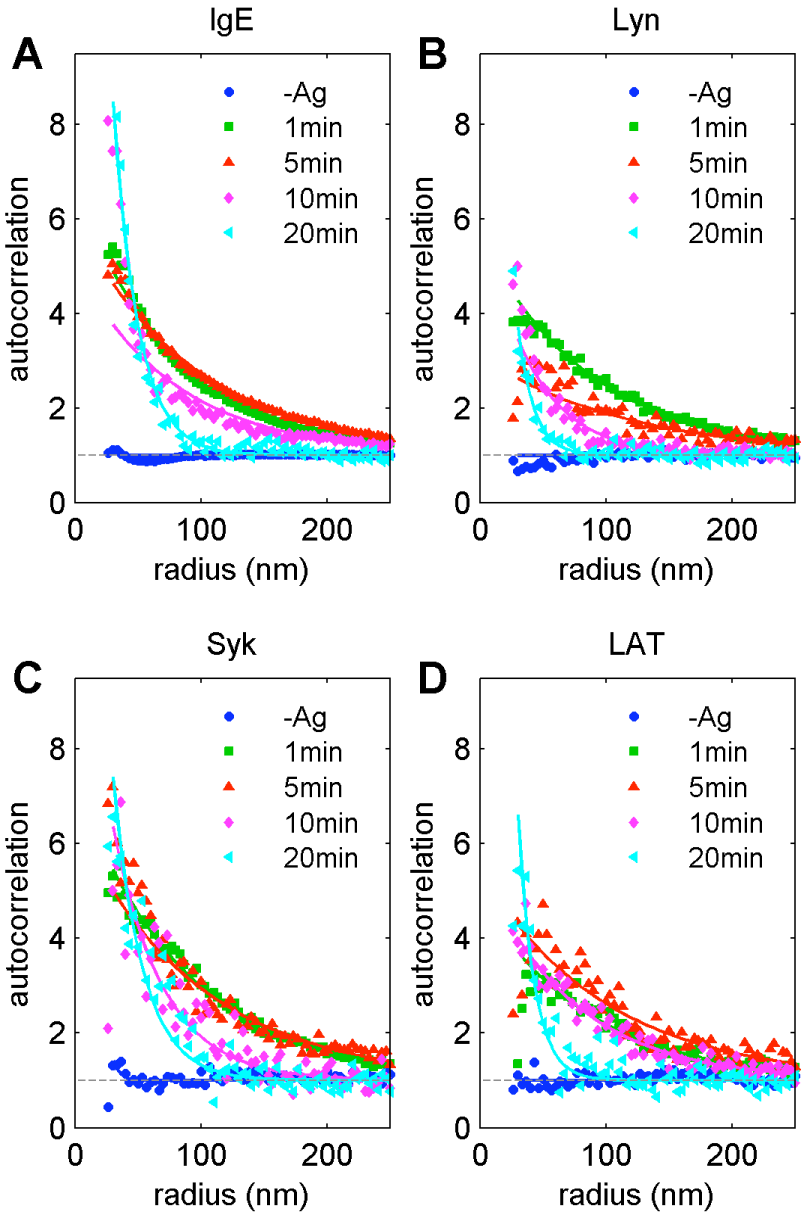

Figure 4.3: (A-D) IgE-FcεRI, Lyn, Syk, and LAT quickly redistribute into large clusters after stimulation, and clusters decrease in size over 20 min. Target proteins are labeled as specified with immuno-gold (10 nm) after cells are stimulated with antigen for times indicated. Gold particle distributions are quantified for multiple images (N>100) using pair auto-correlation functions. Correlation curves are well fit by a single filtered exponential: $g'(r)=1+A\exp\{-r/\xi\}$ for r>20 nm (Eqn 2).

The data points in Figure 4.3 represent a large number of multiple experiments as compiled in Table 4.1. The $g(r)$ curves shown here are corrected to account for artifactual clustering due to multiple gold binding to single target proteins and are fit well by a single filtered exponential. The amplitude of that value for r is related to the increased density of proteins within clusters, and the correlation length (ξ) characterizes the size (radius) of protein-rich clusters. The quality of the fits is shown in Figure 4.3.

For unstimulated cells, the pair auto-correlation functions indicate that IgE-FcεRI, Lyn, Syk, and LAT are randomly distributed over all distances ($g(r) \approx 1$) as indicated by the dark blue circles in Fig 4.3A-D. However, after stimulation with multivalent antigen for 1 min at 37 ˚C, all of these proteins become highly auto-correlated at long distances ($g(r)>1$ for r<~250 nm) (Figure 4.3, green squares). This verifies the visual observations represented in Figure 4.2 that clusters range in size, but can be as large as 250 nm in diameter. Auto-correlation curves evaluated from experiments with longer periods of stimulation (5, 10, and 20 min) indicate that IgE-FcεRI and the three signaling proteins investigated show sustained clustering for more than 10 min. Also, clusters become smaller with longer stimulation time. At 20 min of stimulation, auto-correlation curves decay more quickly such that $g(r)\sim1$ for r≥~75 nm, meaning that the largest persistent clusters have diameters of about 75 nm. In contrast, the GPI-linked protein Thy-1 does not exhibit significant clustering either before or after crosslinking IgE-FcεRI with multivalent antigen under the same conditions (see below, Figure 4.4).

Several parameters that characterize the properties of the clustered distributions are extracted from the exponential fits to the auto-correlation curves as described in Materials and Methods. Values for these properties are plotted in Figure 4.4 for the experiments described in Figure 4.3 and for parallel experiments carried out with 10 nm gold labeled Thy-1. Figure 4.4A shows cluster radius, represented by the correlation length, ξ, as a function of stimulation time.

Within 1 min of antigen addition, all of IgE-FcεRI, Lyn, Syk, and LAT form large clusters (ξ = 70-90 nm) that gradually reduce in size (ξ ~20 nm) during 20 min of stimulation. Thy-1 proteins have a random distribution before and after stimulation. As shown in Figure 4.4B, the average number of IgE-FcεRI, Lyn, Syk, and LAT proteins per cluster (N_{cl}) follows similar trends in time: N_{cl} increases rapidly during the first 1-5 min of antigen stimulation and is reduced at longer stimulation times. If we assume that these proteins are co-clustering, the relative values of N_{cl} for these proteins indicate their corresponding stoichiometries.

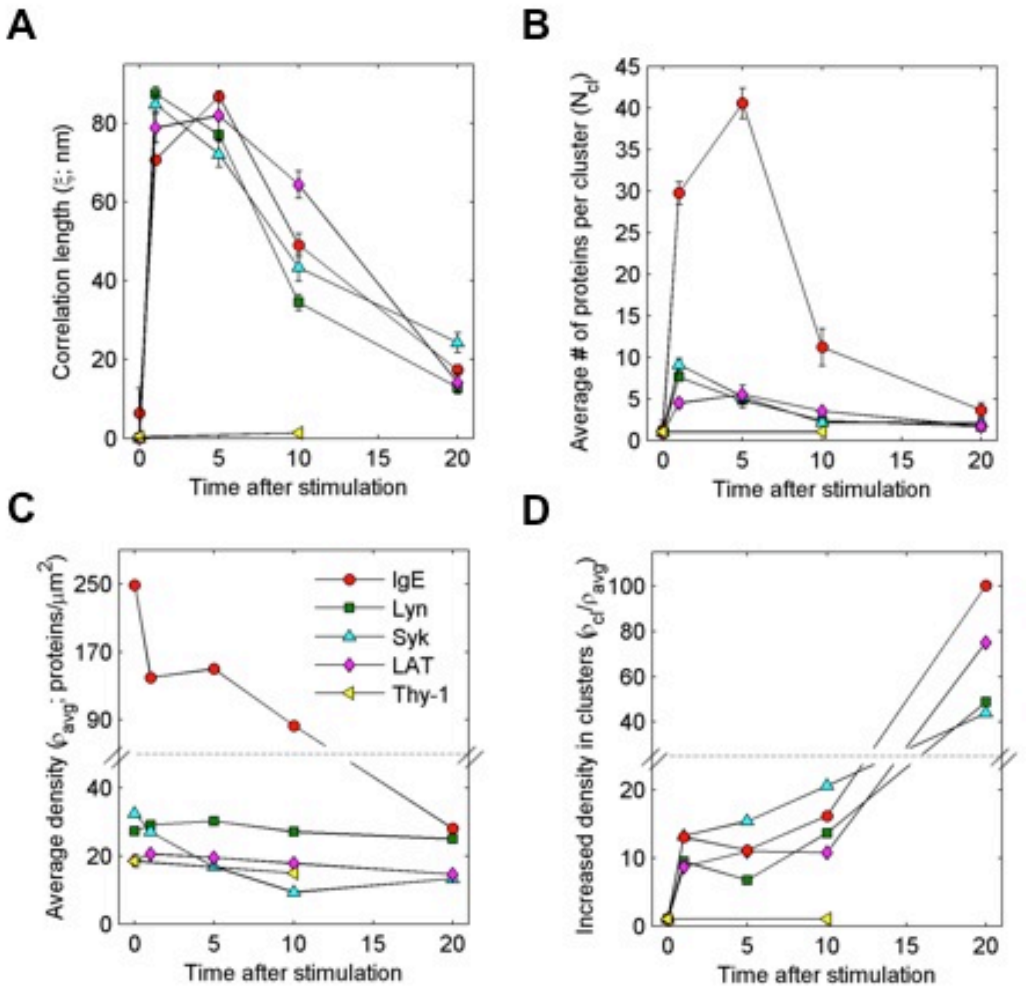

Figure 4.4: Physical properties of clustered target proteins as a function of stimulation time are measured or extracted from correlation functions. Auto-correlation functions determined from many images of specified target proteins are well fit with $g'(r)=1+A\exp\{-r/\xi\}$ for r>20 nm (Eqn 2) as shown in Figure 4.3, and parameters are determined as described in the text: correlation length, ξ (A), average number of proteins per cluster, N_{cl} (B), average protein density, ρ_{avg} (C), and increased density of proteins within clusters, ρ_{cl}/ρ_{avg} (D). These parameters are also tabulated in Table 4A.1 (Appendix).

The average protein density (ρ_{avg}) is obtained by dividing the total surface density of gold particles by the labeling efficiency, *LE*, (described in Materials and Methods). As shown in Figure 4.4C, ρ_{avg} for IgE-FcεRI declines by ~60% during the first 10 min of stimulation consistent with crosslink-dependent internalization [27, 28]. The average density of Syk also declines during this initial stimulation period, consistent with stimulation-dependent internalization and/or degradation of Syk [29]. Alternatively, Syk may dissociate and return to the cytoplasm as IgE internalizes. In contrast, ρ_{avg} for Lyn, LAT, and Thy-1 remains constant throughout the time-course of stimulation, suggesting that these do not co-internalize with crosslinked IgE-FcεRI. The parameter ρ_{cl}/ρ_{avg} provides a measure for the locally enhanced density of proteins within clusters. For IgE-FcεRI, Lyn, Syk, and LAT (but not Thy-1), ρ_{cl}/ρ_{avg} increases ~10-fold during the first min of stimulation, then continues to increase more gradually throughout the subsequent 20 min stimulation time-course (Figure 4.4D). These results reveal that the protein composition within signaling clusters continues to change as stimulation progresses. Our findings that cluster sizes and enhanced densities change in parallel (with the exception of Thy-1), suggest that the signaling proteins examined may be clustered within the same membrane domains. The fit parameters plotted in Figure 4.4 are tabulated in Table 4A.1 (Appendix).

Co-localization of IgE-FcεRI and Lyn Kinase in Double Label Experiments.

To determine whether Lyn co-redistributes with crosslinked IgE-FcεRI domains or segregates to form secondary signaling platforms, we double

labeled IgE-FcεRI and Lyn with distinguishable (5 nm and 10 nm, respectfully) gold particles before and after stimulation with multivalent antigen at 37˚C. As represented in Figure 4.5B, we find that Lyn is visibly co-clustered with crosslinked IgE-FcεRI after 1 min of stimulation with antigen. Additional double label experiments showed that IgE and Lyn remain co-clustered at longer stimulation times (Figure 4.5C-E). Double label experiments were also conducted with IgE-FcεRI (10 nm gold) and Thy-1 (5 nm gold). In contrast to co-clustered IgE-FcεRI and Lyn, Thy-1 does not visibly co-redistribute with crosslinked IgE-FcεRI clusters under these conditions (Figure 4.5F).

Cross-correlation analysis of IgE-FcεRI with Lyn and IgE-FcεRI with Thy-1 are shown in Figure 4.5G. Similar to the auto-correlation *g(r)*, cross-correlation *c(r)* quantifies the probability of finding a protein with a distinguishable second label a distance r away from a given protein with the first label. Just like auto-correlation functions, cross-correlation functions are fit well by single filtered exponentials, where ξ_c corresponds to the correlation length of the co-cluster. Although the individual proteins IgE-FcεRI and Lyn appear unclustered (not auto-correlated) in unstimulated cells (dark blue circles in Figure 4.3), these two proteins are cross-correlated to some extent at short distances (ξ_c = 5 nm; Figure 4.5F), indicating some tendency to pre-associate in the absence of crosslinking by antigen, described in greater detail in Chapter Three. After as little as 1 min stimulation at 37° C with antigen, IgE-FcεRI and Lyn become highly cross-correlated extending to long distances (ξ_c = 150 nm), indicating that these proteins strongly co-cluster under these

conditions (Figure 4.5F). The size of these co-clusters decreases with time, consistent with the decreasing cluster size observed in single label experiments with IgE-FcεRI and Lyn (Figure 4.4A). Consistent with the visual impression in Figure 4.5A, IgE-FcεRI and Thy-1 do not significantly cross-correlate in unstimulated (not shown) or stimulated cells (Figure 4.5F). Cross-correlation lengths for these clusters are tabulated in Table 4A.2 (Appendix).

Stimulated Co-clustering of IgE-FcεRI and Lyn Depends on Tyrosine Kinase Activity and Cholesterol.

To understand the structural basis for the extensive co-clustering of Lyn with antigen-crosslinked IgE-FcεRI, we investigated the effects of treatments known to perturb structure and function. In one set of experiments we evaluated the role of phosphorylation-dependent protein-protein interactions between IgE-FcεRI and Lyn using the Src-family tyrosine kinase inhibitor PP1 [30] to inhibit Lyn kinase activity. Figure 4.6A shows representative SEM images of singly labeled IgE-FcεRI and Lyn after 1 min of antigen stimulation at 37° C both with and without 4 μm PP1 (or other treatments described below). Many images of these samples from multiple experiments were evaluated with auto-correlation functions (Figure 4.6B) that are well fit in all cases by single filtered exponentials (solid lines in Figure 4.6B) to yield characteristic parameters: auto-correlation length (ξ), number of proteins per cluster (N_{cl}), and ratio of protein density in clusters to average density (ρ_{cl}/ρ_{avg}) (Figure 4.6C). These parameters are also tabulated in Table 4A.3 (Appendix).

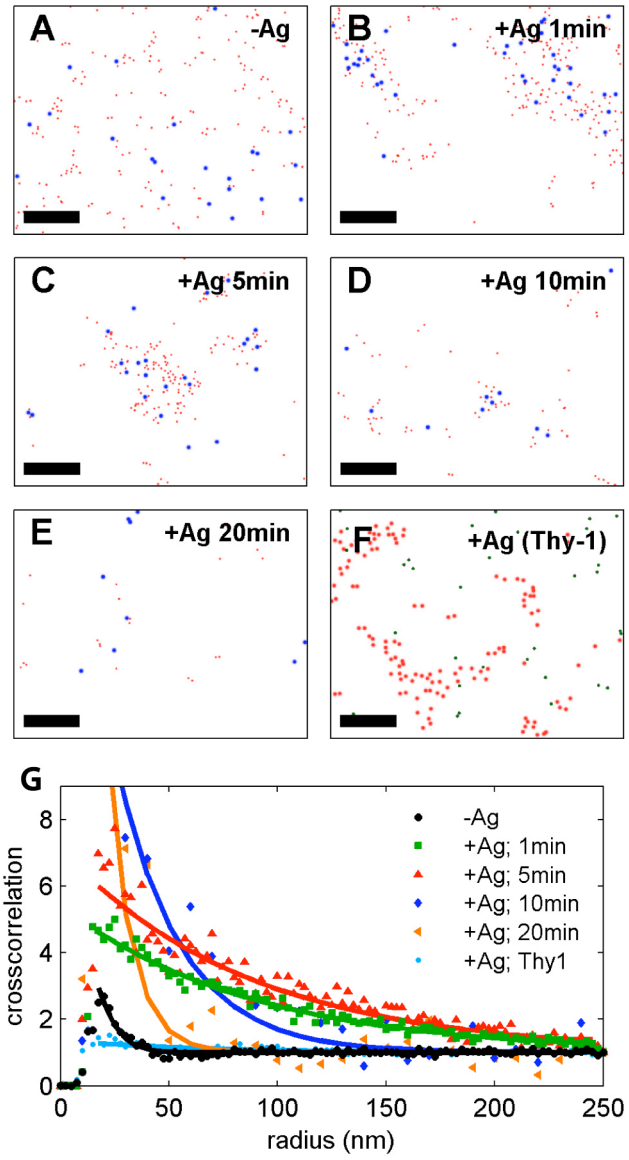

Figure 4.5: Double label experiments reveal that Lyn, but not Thy-1, co-redistributes with IgE-FcεRI after cells are stimulated with antigen and co-clusters decrease in size with time. A-E) Representative reconstructed BSD-SEM images from cells that were stimulated (or not) for times indicated; specified target proteins were immuno-gold labeled. IgE-FcεRI (5 nm gold particles) and Lyn (10 nm gold particles) were double labeled (A-E), or IgE-FcεRI (10 nm gold particles) and Thy-1 (5 nm gold particles) were double labeled (F). Scale bars are 200 nm. G) Gold particle distributions for many images from double label experiments are quantified using cross-correlation functions, and curves are well fit by a filtered exponential $c'(r) \approx 1+A\exp\{-r/\xi_c\}$ (Eqn 2). Extracted fit parameters are tabulated in Table 4A.2 (Appendix).

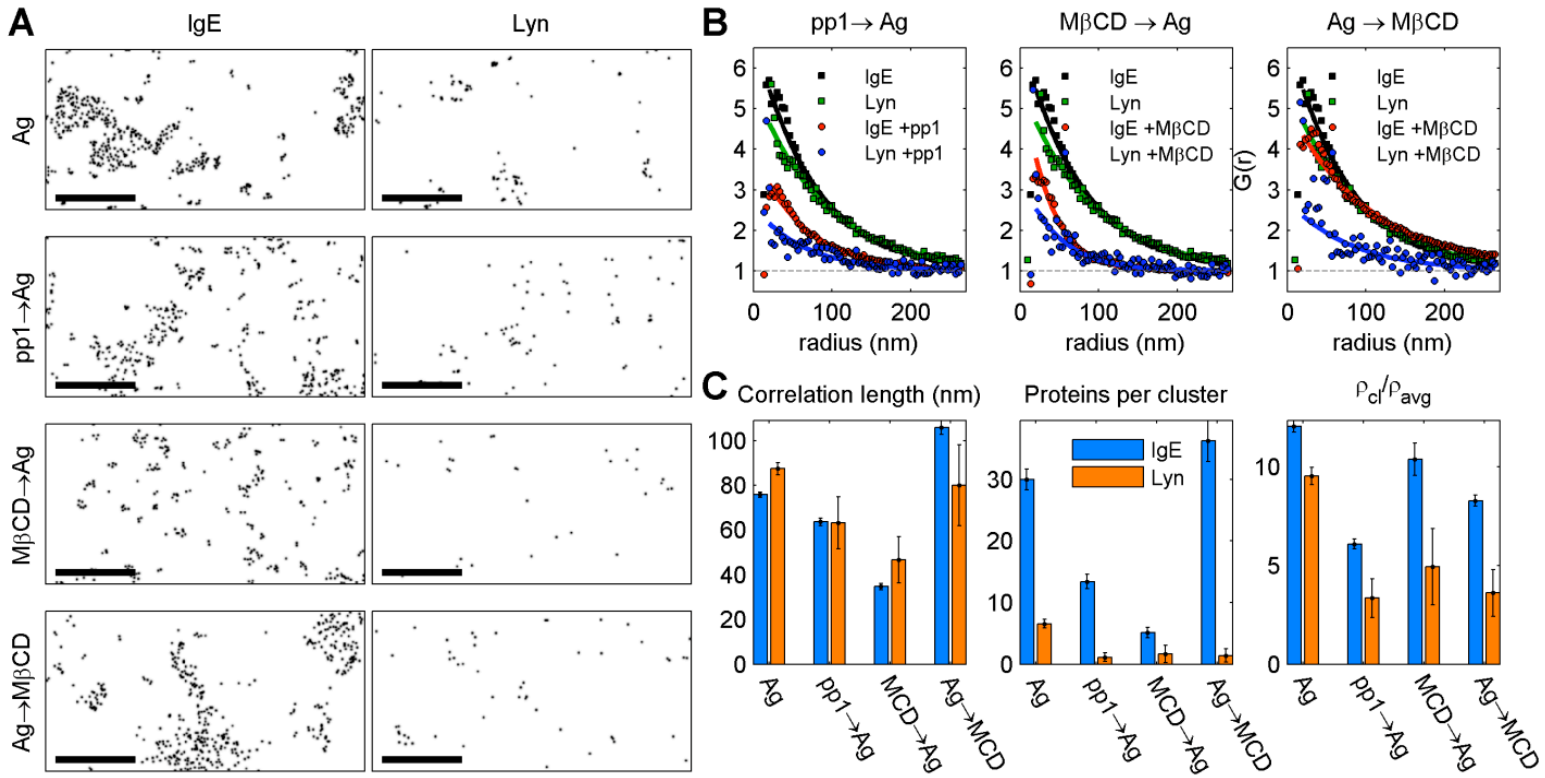

Figure 4.6: Co-redistribution of Lyn with crosslinked IgE-FcεRI is sensitive to Src kinase activity and plasma membrane cholesterol levels. A) Representative reconstructed BSD-SEM images of immuno-gold labeled IgE-FcεRI and Lyn in antigen stimulated cells treated with PP1 prior to simulation or with MβCD either before or after stimulation. B) Auto-correlations quantify particle distributions from many experiments represented in (A), and curves are fit to filtered exponentials as in Figure 4.5 (solid lines). C) Parameters describing ξ, N_{cl}, and ρ_{cl}/ρ_{avg} are extracted from fits shown in (B); values are tabulated in Table 4A.3 (Appendix).

When the kinase inhibitor PP1 is added to cells prior to stimulation, large clusters of both IgE-FcεRI and Lyn still result from antigen crosslinking of IgE-FcεRI (correlation lengths decrease by less than 30% compared to no PP1). However, the numbers of labeled proteins in these clusters decrease substantially in the presence of PP1: For IgE, N_{cl} decreases by ~55%; for Lyn, N_{cl} decreases by ~80% (Figure 4.6C, middle panel). Consistent with this, the ρ_{cl}/ρ_{avg} for both IgE-FcεRI and Lyn in clusters decreases after PP1 treatment (Figure 4.6C, right panel). This indicates that tyrosine kinase activity of Lyn, including phosphorylation of FcεRI, evidently plays a significant role in the accumulation of both IgE-FcεRI and Lyn in these antigen induced clusters.

We investigated the role of plasma membrane cholesterol in modulating IgE-FcεRI and Lyn protein distributions by depleting cellular cholesterol with 10 mM MβCD for 5 min at 37˚C either before or after addition of antigen. As visualized in Figure 4.6A and quantified with auto-correlation functions for many images in Figures 4.6B-C, addition of MβCD prior to antigen crosslinking results in cluster size reduction for both IgE-FcεRI and Lyn (ξ decreases by ~ 50% for both; Figure 4.6C, left panel), and the N_{cl} are decreased by even larger amounts (~80% reduction for both; Figure 4.6C, middle panel). These results suggest that cholesterol-dependent membrane structure facilitates antigen crosslinking of IgE-FcεRI, and this membrane structure also facilitates co-clustering of IgE-FcεRI and Lyn.

If cells are treated with MβCD for 5 min after addition of multivalent antigen for 1 min, the cluster sizes determined for IgE-FcεRI and Lyn do not change dramatically compared to 5 min stimulation in the absence of MβCD (Figure 4.6C, left panel). However, the N_{cl} decreases much more for Lyn (~70%) than for IgE-FcεRI (~10%; Figure 4.6C, middle panel). Cholesterol depletion also reduces the ρ_{cl}/ρ_{avg} for both IgE-FcεRI and Lyn when MβCD is added either before or after multivalent antigen (Figure 4.6C, right panel). These effects of cholesterol depletion reveal a role for this lipid, and possibly the ordered lipid membrane domains it promotes, both in the structural organization of antigen-induced IgE-FcεRI clustering, and in the coupling of crosslinked IgE-FcεRI with Lyn kinase during initial stages of signal transduction.

4.4 DISCUSSION

In this study, we demonstrate that SEM with SED and BSD is useful for investigating distributions of immuno-gold labeled signaling proteins on both the outer and inner leaflets of plasma membranes of fixed, intact cells. Using pair correlation functions, with corrections for multiple gold particle labeling of the same target protein, we find that all proteins investigated have random distributions in unstimulated cells, with no evidence for homotypic clustering (see also Chapter Three). Single label experiments show that IgE-FcεRI, Lyn, Syk, and LAT all redistribute into clusters within 1 min of stimulation by multivalent antigen at 37˚C (Figure 4.2-4.4). Double label experiments show that IgE-FcεRI and Lyn co-redistribute into clusters that are similar in size and

persistence to those visualized in single label experiments over the same time-course (Figure 4.5). Both single label and double label experiments show that these protein clusters are largest 1 min after stimulation with antigen and gradually decrease in size over 20 min as IgE-FcεRI internalize. We also demonstrate that antigen-induced IgE-FcεRI and Lyn co-clustering is sensitive to inhibition of tyrosine kinase activity and to changes in membrane physical state caused by cholesterol depletion (Figure 4.6).

Previous transmission electron microscopy studies have used ripped-off plasma membrane sheets to visualize inner leaflet gold-labeled protein distributions. These studies suggested that IgE-FcεRI, Lyn, Syk, and LAT are self-clustered to a limited extent in unstimulated cells, and antigen crosslinking of IgE-FcεRI causes only limited association of Lyn with larger IgE-FcεRI clusters [24, 25]. Results from these studies were not corrected for multiple antibody binding effects, which may account for apparent self-clustering (Chapter Three). These previous results may also be affected during the membrane ripping process that is done prior to fixation, and by the lighter fixation conditions used subsequent to membrane detachment and prior to labeling with primary and gold-conjugated secondary antibodies. Our study used a combination of SED and BSD in SEM images to characterize redistributions of both outer and inner leaflet signaling proteins that are immuno-gold labeled following strong fixation (4% paraformaldehyde, 0.1% gluteraldehyde) to prevent antibody-induced protein redistributions. SED evaluates membrane topography and provides a check on apparent

heterogeneity of gold particles that may be due to morphological irregularities.

Our experiments show high gold particle labeling efficiencies with an average of ~1 gold particles per target protein (Chapter Three). This provides confidence in our statistical sampling of each protein distribution. We observe specific gold labeling for all proteins analyzed in our SEM experiments: Gold particles are only observed in the presence of target protein-specific primary and species-specific secondary antibodies (Chapter Three). Additionally, we have developed robust algorithms to 1) rigorously identify gold locations (Figure 4.1) and 2) quantify large data sets of particle coordinates using pair auto- and cross-correlation functions with a high degree of statistical confidence (Table 4.1). These correlation functions are useful analytical tools that easily account for the finite size of gold particles and multiply targeted gold-labeled proteins (Chapter Three). Moreover these functions provide relevant information regarding protein cluster size (ξ), number of proteins per cluster (N_{cl}), and other physical parameters. Collectively, these methodological differences and improvements are likely responsible for differences between our results and those reported in previous studies.

Randomly dispersed in unstimulated cells, IgE-FcεRI, Lyn, Syk, and LAT all redistribute into large clusters after 1 min of stimulation with multivalent antigen at 37˚C. Each of these stimulated clusters have ξ values in the range of 70-90 nm (Figure 4.4A), consistent with cluster sizes reported for IgE-FcεRI, Lyn, Syk, and LAT in stimulated membrane sheets [24, 25]. In

double label experiments, we find that that IgE-FcεRI and Lyn show some pre-association in unstimulated cells (Chapter Three), and they co-redistribute within the same large clusters (ξ_c~85 nm) after 1 min of antigen stimulation (Figure 4.5A). One model to explain this finding suggests that Lyn first phosphorylates crosslinked IgE-FcεRI within ordered membrane domains (see below) and then associates through binding interactions between its SH2 domain and phosphorylated receptor ITAMs [6]. Our observations of crosslinked IgE-FcεRI and Lyn co-clustering contrasts with previous results in which Lyn was observed to be largely segregated and/or peripheral from crosslinked IgE-FcεRI that co-clusters with Syk [24]. We investigated the possibility that Lyn might segregate away from IgE-FcεRI at longer stimulation times (5, 10, and 20 min), but we observed that robust co-clustering persists even after 20 min of stimulation (Figure 4.5).

Our single label experiments showed that the large clusters of IgE-FcεRI, Lyn, Syk, and LAT formed after 1 min stimulation (ξ=70-90 nm) gradually decrease in size after 20 min of stimulation (ξ=15-20 nm) (Figure 4.4A). Whereas the ρ_{cl}/ρ_{avg} for Lyn and LAT remains relatively constant throughout the stimulation time-course (Figure 4.4C), we detect a marked reduction in IgE-FcεRI labeling that is consistent with previous observations of receptor internalization [27]. Interestingly, ρ_{avg} for Syk decreases with increasing stimulation time, suggesting that Syk is either co-internalized with IgE-FcεRI, or it dissociates and is degraded as receptors are endocytosed [29]. Additionally, we find that whereas ρ_{avg} for IgE-FcεRI decreases with

stimulation time, ρ_{cl}/ρ_{avg} increases substantially, as does that of Lyn, Syk, and LAT (Figure 4.4D). This time-dependent enhancement in the relative concentration of signaling proteins within clusters may reflect the capacity of the cell to undergo localized remodeling to promote sustained signal propagation as receptors internalize. The strong similarities of these single label time-courses and the co-localization of Lyn with IgE-FcεRI in double label experiments (Figure 4.5) suggest that Syk and LAT also co-cluster with IgE-FcεRI, although we did not evaluate this directly.

Previous biochemical studies have suggested possible roles for cholesterol-dependent ordered lipid membrane structure [15] and stimulated tyrosine phosphorylation of IgE-FcεRI β [12] for interactions between crosslinked IgE-FcεRI and Lyn. We examined the effects of membrane perturbation by cholesterol depletion and the inhibition of Lyn-mediated tyrosine phosphorylation by PP1 on antigen-stimulated redistributions of IgE-FcεRI and Lyn. As summarized in Figure 4.6, we found that reducing plasma membrane levels of cholesterol prior to multivalent antigen stimulation causes a reduction in the size (ξ) of Lyn and crosslinked IgE-FcεRI clusters, as well as a reduction in the number of both proteins in clusters (N_{cl}). Interestingly, cholesterol depletion after stimulation does not significantly change the size of IgE-FcεRI and Lyn clusters, but rather the number of Lyn proteins present in stimulated clusters is substantially reduced. Similarly, we found that cholesterol depletion in unstimulated cells reduces the small amount of cross-

correlation between IgE-FcεRI and Lyn under these conditions (Chapter Three).

Consistent with these results, we previously showed that cholesterol depletion reduces association of both Lyn and crosslinked IgE-FcεRI with detergent membranes, and this correlates with inhibition of stimulated tyrosine phosphorylation, indicating a role for cholesterol-dependent orderd lipid membrane structure in these functional interactions [31]. In the present study, the conditions of cholesterol depletion by MβCD are more moderate (5 min with 10 mM MβCD vs. 60 min in the previous study), and we do not expect that functional coupling between these proteins is completely prevented under present conditions. Our finding that cholesterol depletion after antigen crosslinking does not affect the size of IgE-FcεRI clusters, but rather reduces Lyn co-clustering, provides additional evidence that antigen crosslinking mediates the interaction of IgE-FcεRI with ordered microdomains independent of its interaction with Lyn kinase. Our findings further indicate that cholesterol has a structural role in the organization of antigen-stimulated IgE-FcεRI crosslinking.

Pre-treatment of cells with the Src-family kinase inhibitor, PP1, has only a small effect on cluster sizes of crosslinked IgE-FcεRI and Lyn under stimulation conditions, but the N_{cl} and the ρ_{cl}/ρ_{avg} for both IgE-FcεRI and Lyn are significantly decreased due to this treatment (Figure 4.6C). Stimulated phosphorylation of ITAM tyrosine residues in the β subunit of FcεRI provides binding sites for Lyn SH2 domains, but in the absence of this phosphorylation,

residual co-clustering of Lyn with IgE-FcεRI depends on interactions with ordered lipid domains (Chapter Three) and possibly on direct protein-protein interactions [9]. More surprising is the reduction in crosslinked IgE-FcεRI cluster density by PP1, because this suggests that IgE-FcεRI clustering is not simply a passive consequence of crosslinking by antigen. Thus, an active role by Lyn kinase is implicated in IgE-FcεRI clustering from these results.

Collectively, these findings indicate that both membrane physical state and protein-protein interactions are important mediators of protein organization and the consequent IgE-FcεRI signaling response. They are consistent with the hypothesis that plasma membrane lipids provide an environment that facilitates selective protein clustering and stabilizes protein-protein interactions. Inhibition of receptor phosphorylation (by PP1) may also result in the loss of membrane-cytoskeletal interactions that regulate stimulation-dependent co-clustering of IgE-FcεRI and Lyn. Crosslinking of IgE-FcεRI by multivalent antigen causes a redistribution of actin binding focal adhesion proteins to crosslinked receptors to provide a mechanism for co-clustering of phosphorylated receptor clusters with the actin cytoskeleton [32]. This interaction contributes to restricted diffusion of crosslinked IgE-FcεRI, and may negatively regulate FcεRI signaling [33].

In summary, our results show that crosslinking of IgE-FcεRI by multivalent antigen results in the rapid formation of large signaling platforms rich in Lyn and most likely in other proteins that couple the initial stimulus to early and more sustained signaling events. IgE-FcεRI crosslinking and the

consequent recruitment of Lyn depend on both cholesterol and tyrosine kinase-mediated protein-protein interactions, and they promote clustering of additional downstream signaling proteins Syk and LAT. These studies provide new insights into the mechanism of stimulation-dependent reorganization of IgE-FcεRI and associated signaling proteins, but key issues remain to be addressed. Mechanisms by which membrane-cytoskeleton interactions play an active role in regulating IgE-FcεRI signaling and plasma membrane protein heterogeneity represent important unanswered questions.

APPENDIX

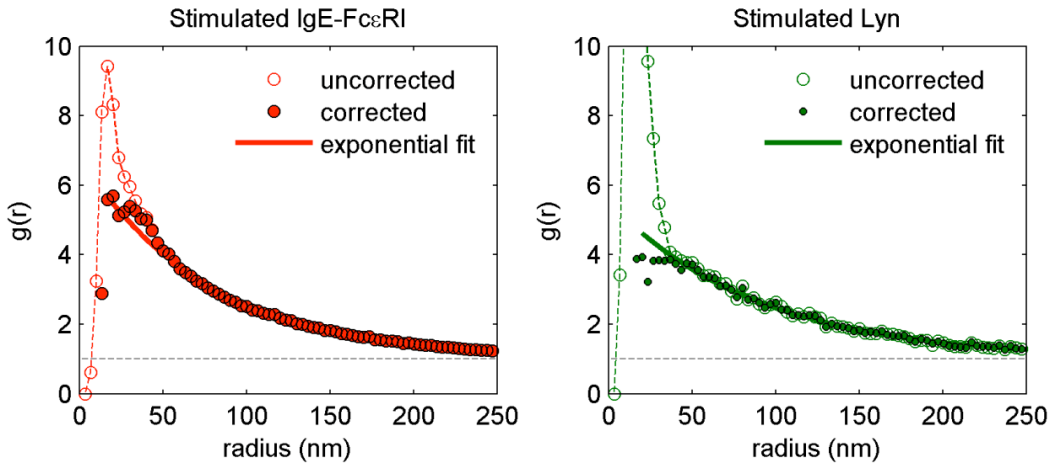

Figure 4A.1: Correcting raw correlation functions for multiple gold particles binding to single target proteins in cells stimulated for 1 min with multivalent antigen. Raw *g(r)* curves (open circles) for clustered distributions of IgE-FcεRI (left) and Lyn (right) contain contributions from multiple gold binding to single target proteins at short radii (r<~30 nm). Corrected correlation functions (solid symbols) are obtained by first fitting the extra intensity at short radii to the first term of Eqn 1, and subsequently subtracting these contributions. The extra intensity at low radii is more substantial in the case of Lyn because Lyn has lower expression levels than FcεRI and the amplitude of the multiple binding term is inversely proportional to protein surface density. After correcting for contributions from multiple binding, we fit residual correlations to a single exponential that is filtered by a Gaussian with the same half width determined from fitting the multiple binding term (solid line). This indicates that the correlation function of the target protein (IgE-FcεRI or Lyn; called $g'(r)$ in the text) decays as a single exponential: $g'(r)=1+A\exp\{-r/\xi\}$ for r>20 nm.

Table 4A.1: Tabulation of values plotted in Figure 4.4: Correlation length (ξ), number of proteins per cluster (N_{cl}), and protein density ratio within clusters (ρ_{cl}/ρ_{avg}).

	+Ag 1 min		+Ag 5 min		+Ag 10 min		+Ag 20 min	
	IgE	Lyn	IgE	Lyn	IgE	Lyn	IgE	Lyn
Correlation Length (nm)	75.8±1.2	87±2.7	86.8±1.3	77±6	49±3	34.5±2	17±1.3	12.8±1.5
Proteins per Cluster	30±2	6.6±0.7	41±2	5±1	11±2	2.3±0.3	4±1	1.6±0.4
Density ratio	12±0.3	9.5±0.4	11.1±0.2	6.8±0.7	16.2±1.6	14±2	100±18	49±17

Table 4A.2: Tabulation of fit parameters from Figure 4.5F. The cross-correlation length (ξ_c) characterizes the size of the IgE-FcεRI-Lyn co-clusters, and the amplitude (A) is related to the increased density of both proteins with co-clusters.

	ξ_c (nm)	A
+Ag 1min	86±2	4.5±0.1
+Ag 5min	85±3	6.3±0.3
+Ag 10min	29±5	27±10
+Ag 20min	10±4	97±50

Table 4A.3: Tabulation of values plotted in Figure 4.6: Correlation length (ξ), number of proteins per cluster (N_{cl}), and protein density ratio within clusters (ρ_{cl}/ρ_{avg})

	+Ag 1 min		PP1→ +Ag		MβCD → +Ag		+Ag → MβCD	
	IgE	Lyn	IgE	Lyn	IgE	Lyn	IgE	Lyn
Correlation Length (nm)	75.8±1.2	87±2.7	63.6±1.6	63±12	34.7±1.5	47±10	106±3	80±18
Proteins per Cluster	30±2	6.6±0.7	13.4±1	1.1±0.7	5.1±0.8	1.6±1	36±3	1.4±1
Density ratio	12±0.3	9.5±0.4	6.1±0.2	3.3±1	10±0.8	4.9±2	8.3±0.3	3.6±1

REFERENCES

1. Blank, U. and J. Rivera, *The ins and outs of IgE-dependent mast-cell exocytosis.* Trends Immunol, 2004. **25**(5): p. 266-73.
2. Kraft, S. and J.P. Kinet, *New developments in FcepsilonRI regulation, function and inhibition.* Nat Rev Immunol, 2007. **7**(5): p. 365-78.
3. Siraganian, R.P., et al., *Protein tyrosine kinase Syk in mast cell signaling.* Mol Immunol, 2002. **38**(16-18): p. 1229-33.
4. Odom, S., et al., *Negative regulation of immunoglobulin E-dependent allergic responses by Lyn kinase.* J Exp Med, 2004. **199**(11): p. 1491-502.
5. Paolini, R., M.H. Jouvin, and J.P. Kinet, *Phosphorylation and dephosphorylation of the high-affinity receptor for immunoglobulin E immediately after receptor engagement and disengagement.* Nature, 1991. **353**(6347): p. 855-8.
6. Holowka, D., et al., *Insights into immunoglobulin E receptor signaling from structurally defined ligands.* Immunol Rev, 2007. **217**: p. 269-79.
7. Sil, D., et al., *Trivalent ligands with rigid DNA spacers reveal structural requirements for IgE receptor signaling in RBL mast cells.* ACS Chem Biol, 2007. **2**(10): p. 674-84.
8. Pribluda, V.S., C. Pribluda, and H. Metzger, *Transphosphorylation as the mechanism by which the high-affinity receptor for IgE is phosphorylated upon aggregation.* Proc Natl Acad Sci U S A, 1994. **91**(23): p. 11246-50.

9. Vonakis, B.M., et al., *The unique domain as the site on Lyn kinase for its constitutive association with the high affinity receptor for IgE.* J Biol Chem, 1997. **272**(38): p. 24072-80.

10. Yamashita, T., S.Y. Mao, and H. Metzger, *Aggregation of the high-affinity IgE receptor and enhanced activity of p53/56lyn protein-tyrosine kinase.* Proc Natl Acad Sci U S A, 1994. **91**(23): p. 11251-5.

11. Furumoto, Y., et al., *The FcepsilonRIbeta immunoreceptor tyrosine-based activation motif exerts inhibitory control on MAPK and IkappaB kinase phosphorylation and mast cell cytokine production.* J Biol Chem, 2004. **279**(47): p. 49177-87.

12. On, M., et al., *Molecular dissection of the FcRbeta signaling amplifier.* J Biol Chem, 2004. **279**(44): p. 45782-90.

13. Dombrowicz, D., et al., *Allergy-associated FcRbeta is a molecular amplifier of IgE- and IgG-mediated in vivo responses.* Immunity, 1998. **8**(4): p. 517-29.

14. Gosse, J.A., et al., *Transmembrane sequences are determinants of immunoreceptor signaling.* J Immunol, 2005. **175**(4): p. 2123-31.

15. Holowka, D., et al., *Lipid segregation and IgE receptor signaling: a decade of progress.* Biochim Biophys Acta, 2005. **1746**(3): p. 252-9.

16. Young, R.M., et al., *Reconstitution of regulated phosphorylation of FcepsilonRI by a lipid raft-excluded protein-tyrosine phosphatase.* J Biol Chem, 2005. **280**(2): p. 1230-5.

17. Holowka, D., E.D. Sheets, and B. Baird, *Interactions between Fc(epsilon)RI and lipid raft components are regulated by the actin cytoskeleton.* J Cell Sci, 2000. **113 (Pt 6)**: p. 1009-19.

18. Larson, D.R., et al., *Temporally resolved interactions between antigen-stimulated IgE receptors and Lyn kinase on living cells.* J Cell Biol, 2005. **171**(3): p. 527-36.

19. Wu, M., et al., *Visualization of plasma membrane compartmentalization with patterned lipid bilayers.* Proc Natl Acad Sci U S A, 2004. **101**(38): p. 13798-803.

20. Saitoh, S., et al., *LAT is essential for Fc(epsilon)RI-mediated mast cell activation.* Immunity, 2000. **12**(5): p. 525-35.

21. Das, R., et al., *Real-time cross-correlation image analysis of early events in IgE receptor signaling.* Biophys J, 2008. **94**(12): p. 4996-5008.

22. Seagrave, J., et al., *Relationship of IgE receptor topography to secretion in RBL-2H3 mast cells.* J Cell Physiol, 1991. **148**(1): p. 139-51.

23. Stump, R.F., et al., *Mapping gold-labeled IgE receptors on mast cells by scanning electron microscopy: receptor distributions revealed by silver enhancement, backscattered electron imaging, and digital image analysis.* J Histochem Cytochem, 1988. **36**(5): p. 493-502.

24. Wilson, B.S., J.R. Pfeiffer, and J.M. Oliver, *Observing FcepsilonRI signaling from the inside of the mast cell membrane.* J Cell Biol, 2000. **149**(5): p. 1131-42.

25. Wilson, B.S., et al., *High resolution mapping of mast cell membranes reveals primary and secondary domains of Fc(epsilon)RI and LAT.* J Cell Biol, 2001. **154**(3): p. 645-58.

26. Carson, D.A., A. Kulczycki, Jr., and H. Metzger, *Interaction of IgE with rat basophilic leukemia cells. III. Release of intact receptors on cell-free particles.* J Immunol, 1975. **114**(1 Pt 1): p. 158-60.

27. Furuichi, K., J. Rivera, and C. Isersky, *The fate of IgE bound to rat basophilic leukemia cells. III. Relationship between antigen-induced endocytosis and serotonin release.* J Immunol, 1984. **133**(3): p. 1513-20.

28. Isersky, C., et al., *The fate of IgE bound to rat basophilic leukemia cells.* J Immunol, 1979. **122**(5): p. 1926-36.

29. Paolini, R., et al., *Activation of Syk tyrosine kinase is required for c-Cbl-mediated ubiquitination of Fcepsilon RI and Syk in RBL cells.* J Biol Chem, 2002. **277**(40): p. 36940-7.

30. Amoui, M., P. Draber, and L. Draberova, *Src family-selective tyrosine kinase inhibitor, PP1, inhibits both Fc epsilonRI- and Thy-1-mediated activation of rat basophilic leukemia cells.* Eur J Immunol, 1997. **27**(8): p. 1881-6.

31. Sheets, E.D., D. Holowka, and B. Baird, *Critical role for cholesterol in Lyn-mediated tyrosine phosphorylation of FcepsilonRI and their association with detergent-resistant membranes.* J Cell Biol, 1999. **145**(4): p. 877-87.

32. Torres, A.J., et al., *Focal adhesion proteins connect IgE receptors to the cytoskeleton as revealed by micropatterned ligand arrays.* Proc Natl Acad Sci U S A, 2008. **105**(45): p. 17238-44.

33. Andrews, N.L., et al., *Actin restricts FcepsilonRI diffusion and facilitates antigen-induced receptor immobilization.* Nat Cell Biol, 2008. **10**(8): p. 955-63.

CHAPTER FIVE

Summary and Conclusions

The plasma membrane is a dynamic and complex structure that is highly organized at many different length-scales. At the micro-scale, the plasma membrane can be visualized as a structurally and biochemically heterogeneous landscape that readily interacts with its surrounding environment. At the nano-scale, plasma membrane heterogeneity arises from protein-protein, protein-lipid, and lipid-lipid interactions. In this work, we have investigated micron-scale plasma membrane organization at the cell-surface interface using patterned poly(acrylic acid) (PAA) polymer brush surfaces. We also studied the nano-scale heterogeneity of multiple plasma membrane associated proteins in intact cells before and after stimulation with multivalent antigen using high resolution SEM.

5.1 Plasma Membrane Reorganization using Patterned PAA Arrays

Understanding how to manipulate and promote favorable interactions at the bio-materials interface is of crucial importance in the fields of tissue engineering. Successful incorporation of a materials device into a biological system often requires surface modifications, which can be `cell-repellent' (i.e., using hydrophilic or charged coatings) or `adhesion-promoting' (i.e., using ridged or grooved surfaces). We have explored both of these strategies to investigate membrane organization and cellular response at the cell-surface interface using micro-patterned PAA polymer brush arrays.

Consistent with previous observations, PAA brushes (30 nm thick) are extremely cell-repellent. However, our studies demonstrate that cell-repellent PAA brushes can be `tuned' to become cell-adhesive by varying PAA brush thickness and incorporating micron-scale patterned PAA regions to the surface (unpatterned regions are bare silicon). When the dimensions of patterned PAA features were larger than those of a typical cell (20 μm squares and larger), cells completely avoided the PAA brush regions and selectively adhered to unpatterned silicon regions. However, as patterned features were reduced in size (2 μm squares), cells robustly spread over patterned PAA brush regions. Additionally, we found that significant plasma membrane reorganization occurs at the brush-membrane interface, due to fibronectin-mediated integrin receptor engagement and subsequent cytoskeletal remodeling. Reducing the thickness of these PAA arrays mitigated, and ultimately prevented, this membrane re-organization, while remaining an adhesion-promoting surface.

While cell adhesion is a useful metric for qualifying a material's biocompatibility, these findings clearly demonstrate that surfaces, which are chemically modified to promote cell adhesion, can induce a range of cellular responses beyond passive adhesion. As these effects may negatively impact biocompatibility, careful consideration must be given to the macro, micro, and nano-scale design of engineered materials and devices that interface with cellular environments. Not only is membrane structure sensitive to its extracellular environment, but topographical and biochemical cell-surface

interactions can induce robust cellular responses that influence membrane heterogeneity.

Because PAA brushes are easily modified with different bio-molecules, these arrays have many potential applications, such as quantifying antibody binding or mapping cell surface protein distributions. We explored the latter by functionalizing PAA arrays with ligands that specifically crosslink IgE-bound FcεRI, and we observed specific enrichment of IgE-FcεRI over these micron-sized surface patterns. In addition to IgE-FcεRI localization, future experiments could monitor the distribution of other associated signaling proteins, such as Lyn, Syk, and LAT. High-resolution fluorescence imaging techniques, such as STORM or PALM [1], may also prove useful for probing protein heterogeneity within these micron and sub-micron antigen-restricted patterned regions.

5.2 Plasma Membrane Microdomains and Nano-scale Protein Heterogeneity

Since it was first proposed that selected GPI-anchored proteins and glycosphingolipids are compartmentalized in the Golgi for directed trafficking to the plasma membrane of polarized epithelial cells [2], the mechanism by which proteins and lipids organize into discrete membrane microdomains has been ardently pursued. Studies monitoring the lateral diffusion of cell surface proteins at high spatial and temporal resolution have suggested that these lipid raft domains are small, dynamic structures [3, 4], and these structures have been implicated with functional roles in many cellular processes, including signal transduction during immune cell activation.

Based on early DRM studies, lipid raft proponents have proposed that antigen stimulation results in stable association of crosslinked receptors with cholesterol-dependent and Src family kinase-rich microdomains from which chemical signals are propagated. However, concerns about detergent-induced artifacts, inconsistent reports on raft structure and composition, and experimental difficulties in visualizing what are likely to be small and transiently lived structures, have led to skepticism on the nature, function, and existence of lipid rafts in general. To dissect the mechanisms that drive early signaling events in IgE-FcεRI activation, we visualized gold-labeled IgE-FcεRI, as well as proteins involved in early receptor-mediated signaling events, before and after stimulation in intact cells under many different experimental conditions.

5.3 Re-examination of Self-Clustered Protein Distributions in Resting Cells

Recent electron microscopy studies in unstimulated cells have suggested proteins have self-clustered distributions within distinct membrane microdomains in resting cells [5]. Given the experimental difficulty in resolving the size and composition of putative `rafts' in resting cells, these findings have been popularly interpreted as evidence for the direct visualization of nano-sized lipid rafts. While these nano-clusters provide an intriguing model to describe nano-scale membrane heterogeneity, careful consideration must be given to the physical basis and physiological relevance of self-clustered protein distributions at the plasma membrane in resting cells.

Using SED and BSD-SEM, we visualized distributions of many different gold-labeled proteins in intact resting cells. Consistent with previous reports, we found that all proteins examined, including proteins immobilized on silicon surfaces, which are expected to have random distributions, appear to be self-clustered. We demonstrate that these self-clustered protein distributions are an artifact of multiple gold particles binding to single target proteins by: imaging proteins conjugated to a silicon surface, comparing correlation functions for a wide range of cell surface labels with varying surface densities, and measuring cross-correlations between functionally identical but distinguishably labeled pools (two differently sized gold particles) of either IgE-FcεRI or GM1-CTxB. After correcting for this artifact, we found that all proteins we examined (A4880-IgE, Thy-1, GT46-YFP, GPI-YFP, Lyn, Syk, and LAT) have random, uncorrelated distributions in unstimulated cells, suggesting that previous studies have overestimated the degree of self-clustering in resting cells.

It is important to note that most previous reports of gold-labeled protein distributions utilize 'ripped-off' membrane sheets. Given the large perturbation that may arise from detaching the plasma membrane from living cells, including the loss of integral membrane-cytoskeleton interactions, we believe SED and BSD-SEM of proteins at the top surface of intact cells better preserves native protein organization. Additionally, our sample preparation protocols use stronger fixation conditions to prevent antibody-induced protein redistributions. In addition to potential gold-labeling artifacts, these differences in experimental sample preparation are likely to account for

discrepancies in previous reports of self-clustered protein distributions. For example, while we have shown that LAT has a random, uncorrelated distribution prior to antigen stimulation, Wilson et al. report clustered distributions of LAT in resting cells, above what can be attributed to multivalent gold binding alone [6].

We also measured cross-correlations between IgE-FcεRI and Lyn in resting cells and showed that both proteins are significantly cross-correlated even though neither protein is self-clustered in single and double label experiments. This suggests that IgE-FcεRI and Lyn interact through specific protein-protein interactions that are stronger than typical protein-lipid or lipid-lipid interaction energies. We calculate that ~44% of Lyn proteins co-cluster with IgE-FcεRI, and ~6% of IgE-FcεRI co-cluster with Lyn in resting cells. If co-clustering between IgE-FcεRI and Lyn is due to binding of inactive Lyn to the β subunit of FcεRI, then these protein-protein interactions are not weak, but strong enough that approximately half of labeled Lyn proteins are associated with IgE-FcεRI. Further, our results suggest that plasma membrane cholesterol levels can modulate the effective binding energy between IgE-FcεRI and Lyn, either through direct binding of cholesterol to one or both proteins, or through indirect interactions.

Alternatively, co-clustering of IgE-FcεRI and Lyn could be driven by the binding of activated Lyn to phosphorylated FcεRI. This would imply that ~6% of IgE-FcεRI is phosphorylated in resting cells at any time and the magnitude of IgE-FcεRI and Lyn co-clustering results from the dynamic

equilibrium between the active and inactive states of Lyn. Changes in plasma membrane cholesterol levels could cause a reorganization of the membrane that favors one state of Lyn over the other, thereby influencing IgE-FcεRI and Lyn co-clustering. Previous studies have also demonstrated that Lyn proteins localized in cholesterol-dependent ordered lipid regions of the membrane have substantially higher specific activity, and that this arises because Lyn in these regions are sequestered from deactivating phosphatases [7]. Cholesterol destabilization of these ordered membrane structures could reduce the total fraction of active Lyn; this would also reduce the total fraction of Lyn co-clustered with IgE-FcεRI in a manner that is consistent with our experimental observations.

5.4 Crosslinked IgE-FcεRI Clusters Form Stable Signaling Platforms

In RBL-2H3 cells, one of the first biochemically detectable steps following IgE-FcεRI crosslinking is receptor phosphorylation by Lyn. The mechanism for the recruitment of Lyn to crosslinked receptors, as well as the activation and mobilization of other proteins involved in early signaling events like Syk and LAT, has yet to be fully elucidated. A significant number of studies have suggested that these early signaling events occur within specialized membrane microdomains, termed lipid rafts. Using high resolution SEM with SED and BSD, we visualized distributions of inner and outer leaflet gold-labeled IgE-FcεRI, Lyn, Syk, and LAT before and after stimulation with multivalent antigen at 37° C.

Consistent with biochemical studies of DRMs in activated RBL cells, pair correlation function analyses of gold-labeled protein distributions revealed that stimulation with multivalent antigen causes IgE-FcεRI, Lyn, Syk, and LAT to rapidly redistribute from a random distribution into large clusters that may represent stable signaling platforms, which gradually reduce in size and composition at longer stimulation times. In agreement with previous electron microscopy studies, cross-correlation analysis revealed that IgE-FcεRI and Lyn are co-clustered to a small extent in resting cells. However, unlike studies that have suggested crosslinked receptors segregate away from Lyn [8], we found that Lyn rapidly associates with crosslinked IgE-FcεRI to a large extent, and these membrane proteins remain co-clustered at long stimulation times (up to 20 min) when the clustered IgE-FcεRI is in the process of internalizing.

The physical basis for interactions between IgE-FcεRI and Lyn before and after receptor crosslinking has been suggested to occur as the result of cholesterol-dependent microdomains [9], as well as direct protein-protein binding interactions [10]. In resting cells we found that cholesterol depletion causes a reduction in the size of IgE-FcεRI and Lyn clusters, as well as a reduction in the number of both proteins in clusters. Similarly, we found that cholesterol depletion in stimulated cells, either before or after stimulation, significantly reduces the association of Lyn with crosslinked IgE-FcεRI clusters. In an effort to evaluate the importance of protein-protein interactions, we demonstrated that treatment with PP1 prior to stimulation

(i.e., to prevent receptor phosphorylation) significantly reduces the association of Lyn with crosslinked IgE-FcεRI. Interestingly, these results do not explicitly distinguish between a raft-only or protein-protein-only model to describe Lyn's recruitment and sustained co-clustering with crosslinked IgE-FcεRI.

One possible interpretation of these findings is that cholesterol depletion prior to stimulation disrupts cholesterol-dependent and Lyn-rich microdomains, hence reducing the propensity of crosslinked IgE-FcεRI to coalesce with raft environments that promote its stable phosphorylation by Lyn. Similarly, cholesterol depletion post stimulation may reduce the cholesterol-stabilized association of crosslinked IgE-FcεRI with Lyn. Further, dissolution of protected raft environments could then result in receptor de-activation by means of transmembrane phosphatases and subsequent loss of protein-protein binding interactions between Lyn and phosphorylated receptor residues.

It is important to note that cholesterol depletion before and after stimulation significantly, but not wholly, reduces Lyn association with crosslinked receptor clusters. Our finding that IgE-FcεRI and Lyn co-clustering is also partially reduced by Src tyrosine kinase inhibition (i.e., inhibition of receptor phosphorylation, which prevents binding of Lyn to phosphorylated receptor residues) indicates that protein-protein binding alone cannot fully account for interactions between IgE-FcεRI and Lyn. Thus, it is likely that the stimulation-induced recruitment of Lyn to crosslinked IgE-FcεRI depends on both raft-mediated and protein-protein interactions.

Of particular relevance to our findings is a re-interpretation of the transphosphophorylation model [11]. According to one version of this model, receptor phosphorylation by Lyn does not require co-residence within cholesterol-dependent microdomains, but rather is dependent on the constitutive association of Lyn and IgE-FcεRI in resting cells by means of a weak binding site [10]. In agreement with previous studies, we find that Lyn is associated with IgE-FcεRI to a small, but significant extent prior to stimulation [8, 10]. Using cross-correlation analysis, we find that cholesterol depletion before and after stimulation reduces this association. Thus, a cholesterol depletion-induced dissociation of co-clustered IgE-FcεRI and Lyn in resting cells would significantly reduce the propensity for Lyn to transphosphorylate nearby receptors after stimulation.

Collectively, these findings indicate that both membrane physical state and protein –protein interactions are important mediators of protein organization. This is consistent with the hypothesis that membrane domains rich in cholesterol and other lipids can provide an environment that facilitates selective protein clustering and stable protein-protein and protein-lipid interactions. Inhibition of receptor phosphorylation by PP1 may not only reduce protein-protein interactions between IgE-FcεRI and Lyn, but also result in a loss of crucial membrane-cytoskeletal interactions that initiate and sustain the stimulation-dependent clustering of IgE-FcεRI and its associated signaling proteins.

Lastly, these perturbations with MβCD and PP1 provide several lines of evidence indicate that IgE-FcεRI clustering is not simply a passive consequence of crosslinking by multivalent antigen: cholesterol depletion pre-stimulation reduces the size of IgE-FcεRI clusters; cholesterol depletion post-stimulation reduces the density but not size of IgE-FcεRI clusters; and inhibition of receptor phosophorylation pre-stimulation significantly reduces the density of IgE-FcεRI clusters.

5.5 Imposing Structural Constraints on IgE-FcεRI Crosslinking

It has previously been suggested that the physical crosslinking of receptors alone may not fully account for the micron-scale clustering observed by fluorescence microscopy. For example, stimulation of cells with small oligomers of IgE, expected to form only small receptor clusters, resulted in micron-scale clustering at the plasma membrane [12]. Recently, trivalent Y-shaped DNA ligands, which crosslink receptors in a spatially regulated manner, were used to explore the structural basis that drives receptor clustering [13]. In this work, Sil et al. showed that changes in the geometry (i.e., how far apart receptors are held from one another) of crosslinked receptor complexes significant influenced early signaling events, such as receptor phosphorylation.

In our studies, we monitored 10 nm immuno-gold labeled IgE-FcεRI distributions before and after stimulation with structurally unique Y-shaped DNP-DNA ligands. Interestingly, we find that stimulation with two different trivalent ligands, which have geometries that only differ by ~ 7 nm in DNP

spacer length, yields dramatically different receptor clusters (Appendix B). While the longer spaced DNP-DNA ligands show significantly reduced nano-scale clustering (~ 5 fold reduction in cluster size) after 10 min of stimulation, both ligands induce nearly indistinguishable micron-scale redistributions at the plasma membrane as visualized by fluorescence microscopy. Not only does this suggest that cellular processes, such as cytoskeletal remodeling, may drive micron-scale IgE-FcεRI clustering, but it also illustrates the resolving power of SEM to detect nano-scale protein heterogeneity that is otherwise obscured by fluorescence microscopy.

5.6 Cytoskeletal Interactions during IgE-mediated Signaling

Considerable evidence supports the view that the cytoskeleton plays a distinct role in regulating lateral membrane heterogeneity. For example, early studies of crosslinked GPI-anchored protein clusters demonstrated an enrichment of actin and actin-associated proteins [3, 14]. In RBL cells, antigen stimulation induces a significant increase in filamentous actin that is coupled with a dramatic remodeling of the cytoskeleton [15]. One suggestion is that membrane-cytoskeleton interactions are highly regulated and tuned such that macroscopic plasma membrane phase separation does not readily occur under physiological conditions. This is evidenced by the observation that giant plasma membrane vesicles (GPMVs), which lack cytoskeletal membrane components, readily undergo macroscopic liquid-liquid immiscibility at room temperature and below [16].

Recent work by Lidke et al. suggests the cytoskeleton regulates both the long-range mobility of IgE-FcεRI at the plasma membrane, as well as influences the dynamics of receptor crosslinking [17]. Additionally, Torres et al. showed that multivalent antigen stimulation causes a redistribution of actin binding focal adhesion proteins to crosslinked IgE-FcεRI clusters [18]. Consistent with these findings, we demonstrated with SEM that actin co-redistributes with crosslinked IgE-FcεRI after stimulation with multivalent antigen (Appendix A). Further, multiple perturbations to the cytoskeleton reveal a dramatic dependence of actin reorganization on the redistribution of signaling proteins involved during early signaling events.

There are still many questions that need to be addressed. In addition to cross-correlation analysis of double labeled IgE-FcεRI and Lyn experiments, other protein pairs, like IgE-FcεRI and Syk, IgE-FcεRI and LAT, and Syk and LAT should be monitored. While we have demonstrated co-redistribution of double labeled IgE-FcεRI and actin after 1 min of multivalent antigen stimulation, both proteins need to be monitored at longer stimulation times to determine whether prolonged actin aggregation is required for the formation of sustained signaling complexes.

Thus far, we have monitored IgE-FcεRI distributions in cells stimulated with Y-shaped DNP-DNA ligands and shown that ligands differing by only 7 nm in DNP spacer length reveal unique nano-scale IgE-FcεRI heterogeneity. Distributions of Lyn, Syk, and LAT will also need to be monitored, in single and double label experiments, after receptor crosslinking with these ligands

(Y16-DNP_3-DNA and Y46-DNP_3-DNA) at multiple stimulation times. Subsequent studies may also take advantage of DNP_3-DNA ligands that possess diverse geometries and flexibilities. For example, X-shaped DNP_3-DNA ligands functionalized with three DNP groups and one gold particle could provide an alternative strategy for directly labeling crosslinked IgE-FcεRI without additional antibodies.

Lastly, recent preliminary work has suggested that IgE receptors, which are not directly crosslinked by multivalent antigen, may form nano-clusters due to nearby crosslinked IgE-FcεRI (unpublished results). In these experiments, cells were (1) sensitized with anti-DNP-IgE and anti-dansyl-A488-IgE (1:1; 2 μg/mL total concentration) for 1 hour at 37° C, (2) stimulated for 1 min at 37° C with DNP-BSA (1μg/mL), and 3) anti-dansyl-A488-IgE-FcεRI was labeled sequentially with primary anti-A488 pAb and secondary 10 nm gold-conjugated pAb. Pair correlation function analysis indicated that these uncrosslinked IgE receptors were clustered at small length-scales, above a random distribution. Further studies are required to explore the physical basis (i.e., actin-based or lipid-based interactions) for this clustered distribution that underscores the subtle nature of membrane heterogeneity.

Through our experimental findings, we have discovered that the stimulation-induced redistribution of crosslinked receptor clusters is due to many different contributions, including ligand structure, membrane cholesterol, Src tyrosine kinase activity, and membrane-cytoskeleton interactions. Collectively, these findings suggest a new framework for

describing the mechanism by which receptor organization is coupled to the recruitment of important signaling proteins during early signaling events, and potentially to downstream signaling events such as calcium mobilization and degranulation.

REFERENCES

1. *Henriques, R. and M.M. Mhlanga, PALM and STORM: what hides beyond the Rayleigh limit? Biotechnol J, 2009.* ***4****(6): p. 846-57.*
2. *Simons, K. and G. van Meer, Lipid sorting in epithelial cells. Biochemistry, 1988.* ***27****(17): p. 6197-202.*
3. *Suzuki, K. and M.P. Sheetz, Binding of cross-linked glycosylphosphatidylinositol-anchored proteins to discrete actin-associated sites and cholesterol-dependent domains. Biophys J, 2001.* ***81****(4): p. 2181-9.*
4. *Subczynski, W.K. and A. Kusumi, Dynamics of raft molecules in the cell and artificial membranes: approaches by pulse EPR spin labeling and single molecule optical microscopy. Biochim Biophys Acta, 2003.* ***1610****(2): p. 231-43.*
5. *Prior, I.A., et al., Direct visualization of Ras proteins in spatially distinct cell surface microdomains. J Cell Biol, 2003.* ***160****(2): p. 165-70.*
6. *Wilson, B.S., et al., High resolution mapping of mast cell membranes reveals primary and secondary domains of Fc(epsilon)RI and LAT. J Cell Biol, 2001.* ***154****(3): p. 645-58.*
7. *Young, R.M., D. Holowka, and B. Baird, A lipid raft environment enhances Lyn kinase activity by protecting the active site tyrosine from dephosphorylation. J Biol Chem, 2003.* ***278****(23): p. 20746-52.*
8. *Wilson, B.S., J.R. Pfeiffer, and J.M. Oliver, Observing FcepsilonRI signaling from the inside of the mast cell membrane. J Cell Biol, 2000.* ***149****(5): p. 1131-42.*
9. *Holowka, D., et al., Lipid segregation and IgE receptor signaling: a decade of progress. Biochim Biophys Acta, 2005.* ***1746****(3): p. 252-9.*

10. *Vonakis, B.M., et al., Interaction between the unphosphorylated receptor with high affinity for IgE and Lyn kinase. J Biol Chem, 2001.* ***276****(2): p. 1041-50.*

11. *Pribluda, V.S., C. Pribluda, and H. Metzger, Transphosphorylation as the mechanism by which the high-affinity receptor for IgE is phosphorylated upon aggregation. Proc Natl Acad Sci U S A, 1994.* ***91****(23): p. 11246-50.*

12. *Menon, A.K., D. Holowka, and B. Baird, Small oligomers of immunoglobulin E (IgE) cause large-scale clustering of IgE receptors on the surface of rat basophilic leukemia cells. J Cell Biol, 1984.* ***98****(2): p. 577-83.*

13. *Sil, D., et al., Trivalent ligands with rigid DNA spacers reveal structural requirements for IgE receptor signaling in RBL mast cells. ACS Chem Biol, 2007.* ***2****(10): p. 674-84.*

14. *Harder, T. and K. Simons, Clusters of glycolipid and glycosylphosphatidylinositol-anchored proteins in lymphoid cells: accumulation of actin regulated by local tyrosine phosphorylation. Eur J Immunol, 1999.* ***29****(2): p. 556-62.*

15. *Oliver, J.M., et al., Signal transduction and cellular response in RBL-2H3 mast cells. Prog Allergy, 1988.* ***42****: p. 185-245.*

16. *Baumgart, T., et al., Large-scale fluid/fluid phase separation of proteins and lipids in giant plasma membrane vesicles. Proc Natl Acad Sci U S A, 2007.* ***104****(9): p. 3165-70.*

17. *Andrews, N.L., et al., Actin restricts FcepsilonRI diffusion and facilitates antigen-induced receptor immobilization. Nat Cell Biol, 2008.* ***10****(8): p. 955-63.*

18. *Torres, A.J., et al., Focal adhesion proteins connect IgE receptors to the cytoskeleton as revealed by micropatterned ligand arrays. Proc Natl Acad Sci U S A, 2008.* ***105****(45): p. 17238-44.*

APPENDIX A

Cytoskeletal Interactions During IgE-Mediated Signaling

A.1 INTRODUCTION

Actin polymerization and reorganization of the cytoskeleton is a well known consequence of IgE receptor aggregation. In RBL cells, perturbations to the cytoskeleton (using cytochalasin D or latrunculin A) can induce enhanced phosphorylation of IgE-FcεRI and Syk, as well as enhanced calcium and secretion responses, suggesting a negative role for actin polymerization in IgE-mediated signaling [1-4]. Additionally, the cytoskeleton has been implicated in raft-mediated signaling processes. For example, fluorescence microscopy studies have shown that microdomains rich in raft components (i.e., crosslinking of CD59 or IgE-FcεRI) co-localize with actin and Src family tyrosine kinases [5, 6]. In the same vein, recruitment of Lyn to IgE-FcεRI clusters after receptor crosslinking is reduced when cells are stimulated after cytoskeletal perturbations [6]. Recently, analyses of phospholipid composition in DRMs before and after FcεRI stimulation, as well as in the presence of cytochalasin D, have indicated that cytoskeletal perturbations alter DRM composition in a manner that implicates actin polymerization in the regulation of lipid raft compositions [7].

More generally, ultra fast single particle tracking (SPT) experiments by Kusumi and colleagues have suggested that the plasma membrane is compartmentalized into domains that are several hundred nanometers in size.

At short time-scales, lipids and proteins freely diffuse within individual compartments, while undergoing hop diffusion between compartments at long time-scales; thus, the cytoskeleton effectively confines the lateral diffusion of membrane components [8-11]. Of particular interest is a proposed 'oligomerized-induced trapping' mechanism, in which the crosslinking of proteins slows the rate of hop diffusion and allows stable signaling complexes to form via cytoskeleton tethers [12].

In agreement with such a model, recent work has suggested that the actin cytoskeleton can restrict the diffusion of cell surface IgE-FcεRI, as well as influence long-range receptor diffusion and receptor-ligand binding [13]. In this work, we monitored the nano-scale distribution of actin and IgE-FcεRI before and after stimulation with multivalent antigen to study cytoskeletal contributions to stimulation-dependent protein reorganization. We also investigated the effects of cytoskeletal perturbations on the redistribution of IgE-FcεRI, Lyn, Syk, and LAT into large clusters immediately following stimulation.

A.2 MATERIALS AND METHODS

Latrunculin A, jasplakinolide, and FITC-phalloidin were purchased from Invitrogen, and anti-actin mAb and cytochalasin D were purchased from Sigma. All other materials were purchased and/or acquired as described in previous chapters. In single label experiments, actin was labeled with anti-actin mAb (or FITC-phalloidin and anti-FITC mAb) followed by 10 nm gold-conjugated species-specific antibodies. In double label experiments, A488-IgE-

FcεRI and actin were labeled simultaneously with anti-A488 pAb and anti-actin mAb, followed by sequential immuno-gold labeling with 10 nm (anti-actin) and 5 nm (anti-A488-IgE) gold-antibody conjugates. All immuno-gold labeling was done in the presence of 0.1% TX-100. Cell sample preparation, SED and BSD-SEM imaging of gold-labeled proteins, corrections for clustering artifacts, and quantification of particle distributions using pair auto- and cross-correlation functions were performed as described in previous Chapters.

A.3 RESULTS and DISCUSSION

In single label experiments, we find that 10 nm gold-labeled actin rapidly redistributes into large clusters after 1 min of stimulation with multivalent antigen at 37˚ C, as illustrated in representative BSD-SEM images shown in Figure A.1A. Gold particle distributions were quantified using pair correlation functions in Figure A.1B. In resting cells, actin has a random, unclustered distribution. However, after stimulation with multivalent antigen (+Ag), actin forms large clusters (ξ~75 nm) that are correlated at long length-scales ($r<250$ nm). In double label experiments, IgE-FcεRI and actin co-redistribute into large clusters after 1 min of stimulation with multivalent antigen at 37˚ C, shown by representative reconstructed BSD-SEM images in Figure A.2A.

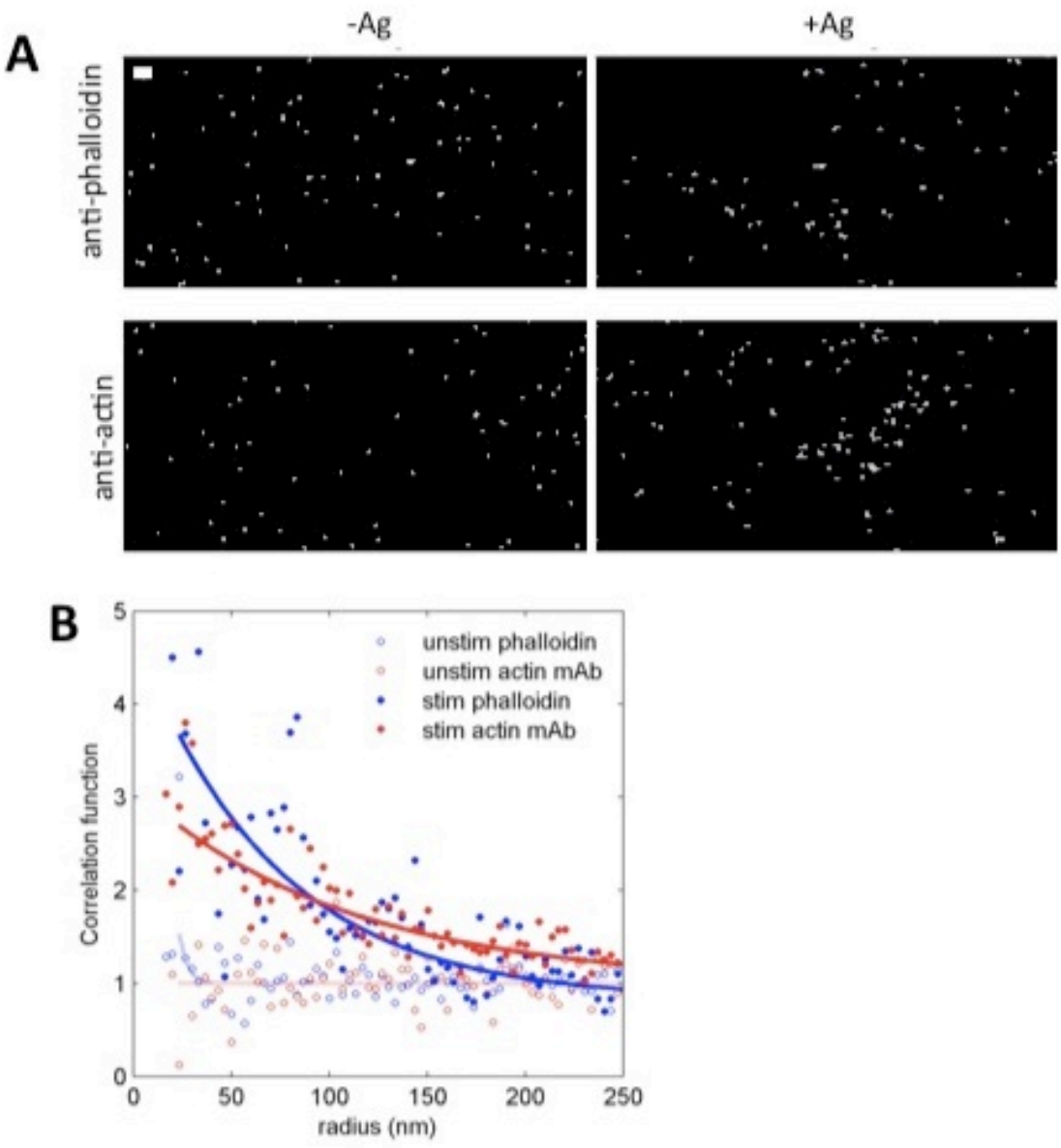

Figure A.1: Actin redistributes into large clusters after 1 min stimulation at 37° C. A) Representative BSD-SEM images of actin labeled with either anti-FITC-phalloidi.n mAb or anti-actin mAb followed by 10 nm gold-antibody conjugates. Scale bar is 100 μm. B) Gold particle distributions were quantified using pair correlation functions that are well fit to single filtered exponentials. Actin has a random distribution in resting cells (open circles), but forms large clusters that are correlated at long length-scales (r<250 nm) after stimulation (closed circles).

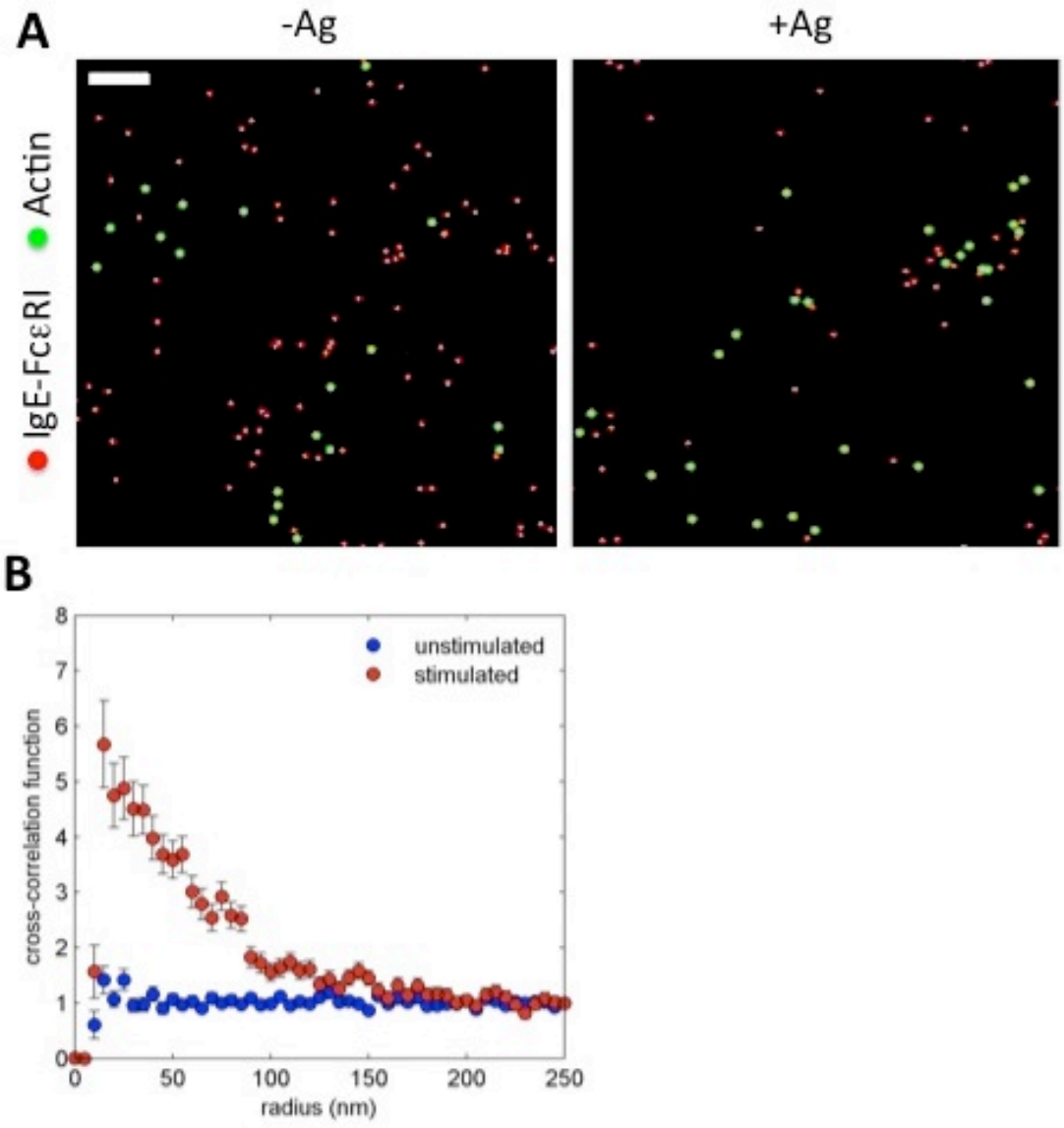

Figure A.2: IgE-FcεRI and actin co-redistribute into the same large clusters after 1 min stimulation at 37° C. A) Representative reconstructed BSD-SEM images of double labeled A488-IgE-FcεRI (5 nm gold) and actin (10 nm gold) before and after stimulation with multivalent antigen. Scale bar is 100 nm. B) Cross-correlation functions indicate that IgE-FcεRI and actin become highly cross-correlated at long length-scales (r<200 nm) after stimulation, consistent with visual observations of co-clustering seen in (A).

The gold particle distributions shown in Figure A.2A were quantified with cross-correlation functions displayed in Figure A.2B. In resting cells, IgE-FcεRI and actin are pre-associated with one another at very short length-scales, as indicated by $c(r)=1$ for r< ~20 nm. However, after 1 min of stimulation, IgE-FcεRI and actin become highly cross-correlated, indicating that they are co-clustered within the same domains, with cross-correlation lengths (ξ_c) of approximately 75 nm. This is consistent with visible observations of IgE-FcεRI and actin co-clustering visualized in A.2A.

Observations of actin enrichment within crosslinked IgE-FcεRI clusters led us to investigate the effects of cytoskeletal perturbations on the stimulation-dependent reorganization of IgE-FcεRI, Lyn, Syk, and LAT. In these experiments, cells were pre-treated with 2 μM cytochalasin D (5 min), 2 μM latrunculin A (5 min), or 3 μM jasplakinolide (1 hr) at 37° C prior to 1 min stimulation with multivalent antigen. Proteins were immuno-gold labeled as described in previous Chapters, and gold particle distributions for each protein were quantified over many images using pair correlation functions that are well fit to single filtered exponentials. Extracted fit parameters, shown in Figure A.3, from these curves describe protein cluster size (ξ; A.3A) and average number of proteins in clusters (N_{cl}; A.3B).

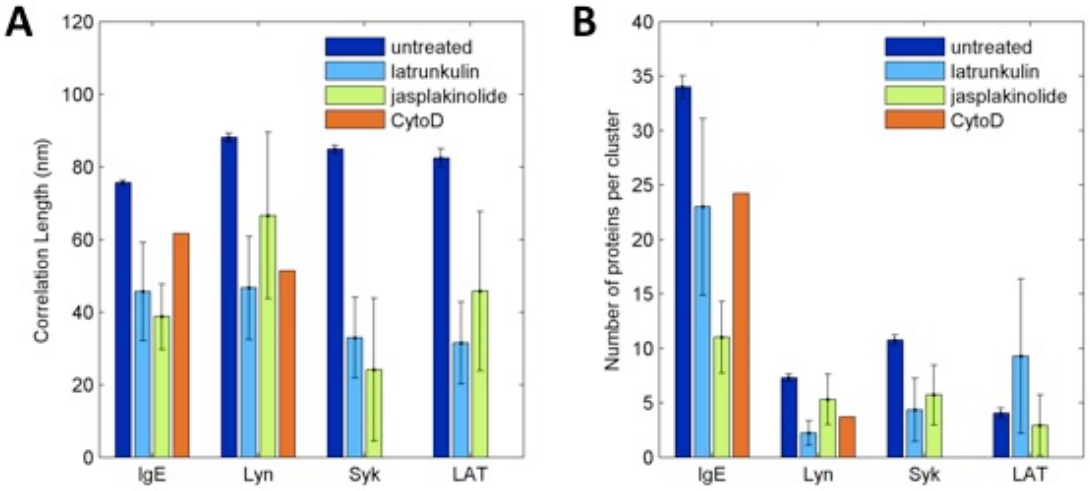

Figure A.3: Cytoskeletal perturbations reduce the size of protein clusters and the number of proteins per cluster. Cells were pre-treated with latrunculin A, jasplakinolide, or cytochalasin D prior to 1 min stimulation with multivalent antigen at 37° C. IgE-FcεRI, Lyn, Syk, and LAT were labeled with 10 nm gold particles in single label experiments, and protein distributions were quantified with pair correlation functions that are well fit to single filtered exponentials. Extracted fit parameters from these curves describe protein cluster size (A) and the number of proteins in clusters (B) for each of the experimental conditions described in the text.

We find that cytoskeletal perturbations significant affect the stimulation-dependent redistribution of signaling proteins, both in terms of the size of protein clusters, as well as the number of proteins found in clusters. Latrunculin treatment reduces the size of stimulated IgE-FcεRI, Lyn, Syk, and LAT clusters by ~40-60% and cytochalasin D treatment has similar effects on stimulated IgE-FcεRI (~20%) and Lyn clusters (~40%). Jasplakinolide treatment reduces the size of stimulated IgE-FcεRI, Syk, and LAT clusters by ~40-70%, while Lyn remains unaffected. We also find that Latrunculin treatment reduces the number of Lyn and Syk proteins in clusters by ~70% and ~50%, respectfully, while IgE-FcεRI and LAT are not significantly affected. Jasplakinolide treatment reduces the number of IgE-FcεRI (~65%) and Syk (~50%) proteins in clusters, but does not affect Lyn and LAT clusters. Cytochalasin D reduces the number of IgE-FcεRI (~30%) and Lyn (~40%) proteins in clusters.

The observation that jasplakinolide reduces the size of LAT clusters but not the number of proteins in clusters suggests that sustained actin polymerization may be required to stabilize large LAT clusters, thereby regulating LAT density within crosslinked IgE-FcεRI domains. Jasplakinolide reduces the size of protein clusters and the number of proteins in clusters for both IgE-FcεRI and Syk. Under these conditions, stabilization of actin filaments may impair IgE-FcεRI crosslinking, as well as Syk recruitment to crosslinked receptor clusters. In contrast, jasplakinolide does not affect Lyn cluster size or composition, suggesting 1) IgE-FcεRI and Lyn interactions may

be more strongly mediated by membrane physical state or protein-protein interactions (described in Chapter Three and Four) and 2) stabilized actin filaments may provide a fence-like meshwork that keeps Lyn proteins resident within crosslinked receptor domains.

While latrunculin treatment reduces the number of Lyn and Syk proteins in clusters after stimulation, IgE-FcεRI and LAT clusters are unaffected. One interpretation is that actin filaments are primarily involved in stabilizing large crosslinked receptor clusters, rather than recruiting and forming large crosslinked clusters. Consistent with the jasplakinolide findings, disassembly of an actin fence that promotes sustained interactions between IgE-FcεRI and Lyn would reduce the number of Lyn present in crosslinked receptor clusters. Similar to jasplakinolide, the number of LAT proteins in stimulated clusters seems to be unaffected by latrunculin treatment.

The observation that cytochalasin D reduces the size and composition of stimulated IgE-FcεRI and Lyn clusters indicates that actin polymerization plays an essential role in initiating and stabilizing stimulated clusters containing IgE-FcεRI and Lyn. We have not yet investigated stimulated Syk and LAT distributions in cells treated with cytochalasin D. Based on the findings of this study, it is reasonable to predict that the size of stimulated Syk clusters, as well as the number of Syk proteins in clusters, will be reduced. It is also reasonable to predict LAT clusters will be reduced in size, but the number of LAT proteins in clusters will be unaffected.

Further studies are required to better understand the role of the cytoskeleton in stimulation-dependent protein reorganization. Current interpretation of this data is complicated by limited data sets and a wide range of observed experimental phenotypes. It is possible, and perhaps likely, that cytoskeletal perturbations induce non-linear effects on protein distributions. For example, stabilizing actin filaments for extended amounts of time (~1 hr) may not only change protein-protein interactions, which contribute to protein organization, but also the topographical and biophysical landscape of the plasma membrane. Structural changes in the underlying cytoskeleton, which can destabilize lipid-based interactions, may also yield protein distributions that current models cannot describe. Double label experiments monitoring the distributions of actin, as well as additional proteins such as Lyn, Syk, and LAT, are also likely to provide additional insight to describe cytoskeletal contributions to plasma membrane and protein heterogeneity.

REFERENCES

1. Pfeiffer, J.R., et al., *Membrane and cytoskeletal changes associated with IgE-mediated serotonin release from rat basophilic leukemia cells.* J Cell Biol, 1985. **101**(6): p. 2145-55.
2. Frigeri, L. and J.R. Apgar, *The role of actin microfilaments in the down-regulation of the degranulation response in RBL-2H3 mast cells.* J Immunol, 1999. **162**(4): p. 2243-50.
3. Holowka, D., E.D. Sheets, and B. Baird, *Interactions between Fc(epsilon)RI and lipid raft components are regulated by the actin cytoskeleton.* J Cell Sci, 2000. **113 (Pt 6)**: p. 1009-19.
4. Pierini, L., et al., *Evidence supporting a role for microfilaments in regulating the coupling between poorly dissociable IgE-Fc epsilonRI aggregates downstream signaling pathways.* Biochemistry, 1997. **36**(24): p. 7447-56.
5. Harder, T. and K. Simons, *Clusters of glycolipid and glycosylphosphatidylinositol-anchored proteins in lymphoid cells: accumulation of actin regulated by local tyrosine phosphorylation.* Eur J Immunol, 1999. **29**(2): p. 556-62.
6. Wu, M., et al., *Visualization of plasma membrane compartmentalization with patterned lipid bilayers.* Proc Natl Acad Sci U S A, 2004. **101**(38): p. 13798-803.
7. Han, X., et al., *IgE receptor-mediated alteration of membrane-cytoskeleton interactions revealed by mass spectrometric analysis of detergent-resistant membranes.* Biochemistry, 2009. **48**(27): p. 6540-50.

8. Dietrich, C., et al., *Relationship of lipid rafts to transient confinement zones detected by single particle tracking.* Biophys J, 2002. **82**(1 Pt 1): p. 274-84.
9. Fujiwara, T., et al., *Phospholipids undergo hop diffusion in compartmentalized cell membrane.* J Cell Biol, 2002. **157**(6): p. 1071-81.
10. Sako, Y. and A. Kusumi, *Compartmentalized structure of the plasma membrane for receptor movements as revealed by a nanometer-level motion analysis.* J Cell Biol, 1994. **125**(6): p. 1251-64.
11. Sako, Y. and A. Kusumi, *Barriers for lateral diffusion of transferrin receptor in the plasma membrane as characterized by receptor dragging by laser tweezers: fence versus tether.* J Cell Biol, 1995. **129**(6): p. 1559-74.
12. Kusumi, A., et al., *Paradigm shift of the plasma membrane concept from the two-dimensional continuum fluid to the partitioned fluid: high-speed single-molecule tracking of membrane molecules.* Annu Rev Biophys Biomol Struct, 2005. **34**: p. 351-78.
13. Andrews, N.L., et al., *Actin restricts FcepsilonRI diffusion and facilitates antigen-induced receptor immobilization.* Nat Cell Biol, 2008. **10**(8): p. 955-63.

APPENDIX B

Trivalent Y-shaped DNA Ligands Reveal Nano-scale IgE-FcεRI Heterogeneity

B.1 INTRODUCTION

In Chapter Four, we showed that IgE-FcεRI redistributes into large nano-scale clusters (ξ~80 nm) after 1 min stimulation with multivalent antigen at 37˚ C. By fluorescence microscopy, this reorganization is visualized as a micron-scale patchy distribution of fluorescently labeled IgE-FcεRI at the plasma membrane after a few minutes of stimulation. While multivalent crosslinking ligands are useful for generating robust mast cell signaling responses, it is difficult to gain quantitative information about the minimum size and composition of receptor aggregates required for initiating signaling responses.

Despite the general observation that multivalent antigen stimulation induces micron-scale receptor aggregation at the plasma membrane, the mechanism that drives the formation of these structures, as well as their physiological basis, has not been fully elucidated. Early studies have addressed these questions by evaluating the capacity of differently sized IgE oligomers to elicit mast cell response. While IgE dimers are capable of triggering degranulation, IgE trimers and larger oligomers were shown to be better at stimulating signaling responses [1, 2].

Interestingly, Menon et al. demonstrated that IgE tetramers are fully capable of inducing micron-scale IgE-FcεRI clustering [3], suggesting that large-scale receptor aggregation is not wholly due to passive ligand-mediated crosslinking. This is consistent with our previous findings in Chapter Four that the formation of large, dense crosslinked IgE-FcεRI clusters is sensitive to both cholesterol depletion (MβCD) and Src kinase inhibition (PP1). Additionally, we demonstrated that actin is enriched in crosslinked IgE-FcεRI clusters, and perturbations to the actin cytoskeleton reduce the size and density of these (and other proteins like Lyn, Syk, and LAT) clusters (Appendix A), indicating that many cellular responses contribute to large-scale receptor clustering.

Recent studies have demonstrated that structurally constrained receptor crosslinking significantly affects receptor phosphorylation and tyrosine kinase mobilization during early signaling events [4]. Using rigid Y-shaped trivalent DNP-DNA ligands with spacings of different lengths between the DNP groups (4.5 nm spacing for Y16-DNP_3-DNA and 13.5 nm spacing for Y46-DNP_3-DNA) Sil et al. demonstrate that shorter ligands are more efficient at triggering calcium and degranulation responses [4]. Additionally, they demonstrated a similar length-dependence on stimulated tyrosine phosphorylation of IgE-FcεRI and LAT, in which there was a 4-10 fold response difference between the shortest and longest length ligands.

Given this specific length-dependence, we investigated the micron-scale distribution of IgE-FcεRI before and after stimulation with Y16-DNP_3-

DNA (4.5 nm) and Y46-DNP_3-DNA (13.5 nm) using confocal fluorescence microscopy. Using the same methodology and analytical tools described in Chapter Four, we also explored the nano-scale organization of IgE-FcεRI after stimulation with trivalent DNP-DNA ligands to determine the role of spatial crosslinking constraints on IgE-FcεRI heterogeneity at the plasma membrane.

B.2 MATERIALS and METHODS

Trivalent DNA ligands (Y16-DNP_3-DNA and Y46-DNP_3-DNA) were prepared as previously described [4]. Cell culture, sample preparation, labeling of A488-IgE-FcεRI with 10 nm gold-antibody conjugates, SED and BSD-SEM imaging, particle quantification, and corrections for artifactual clustering were performed as described in previous Chapters. Cells were stimulated either with 1ug/mL DNP-BSA (15 nM), 30 nM Y16-DNP_3-DNA, or 30 nM Y46-DNP_3-DNA for 1, 5, or 10 min at either 37˚ C or room temperature.

B.3 RESULTS and DISCUSSION

Using fluorescence microscopy, we monitored the distribution of A488-IgE-FcεRI before and after stimulation with DNP-BSA, Y16-DNP_3-DNA, or Y46-DNP_3-DNA for 10 min at room temperature, as shown in representative images in Figure B.1. In unstimulated cells, IgE-FcεRI uniformly labels the plasma membrane (B.1A). After stimulation with DNP-BSA (B.1B), IgE-FcεRI redistributes with a micron-scale patchy distribution at the plasma membrane. Interestingly, stimulation with either Y16-DNP_3-DNA (B.1C) or Y46-DNP_3-DNA (B.1D) causes the same patchy distribution.

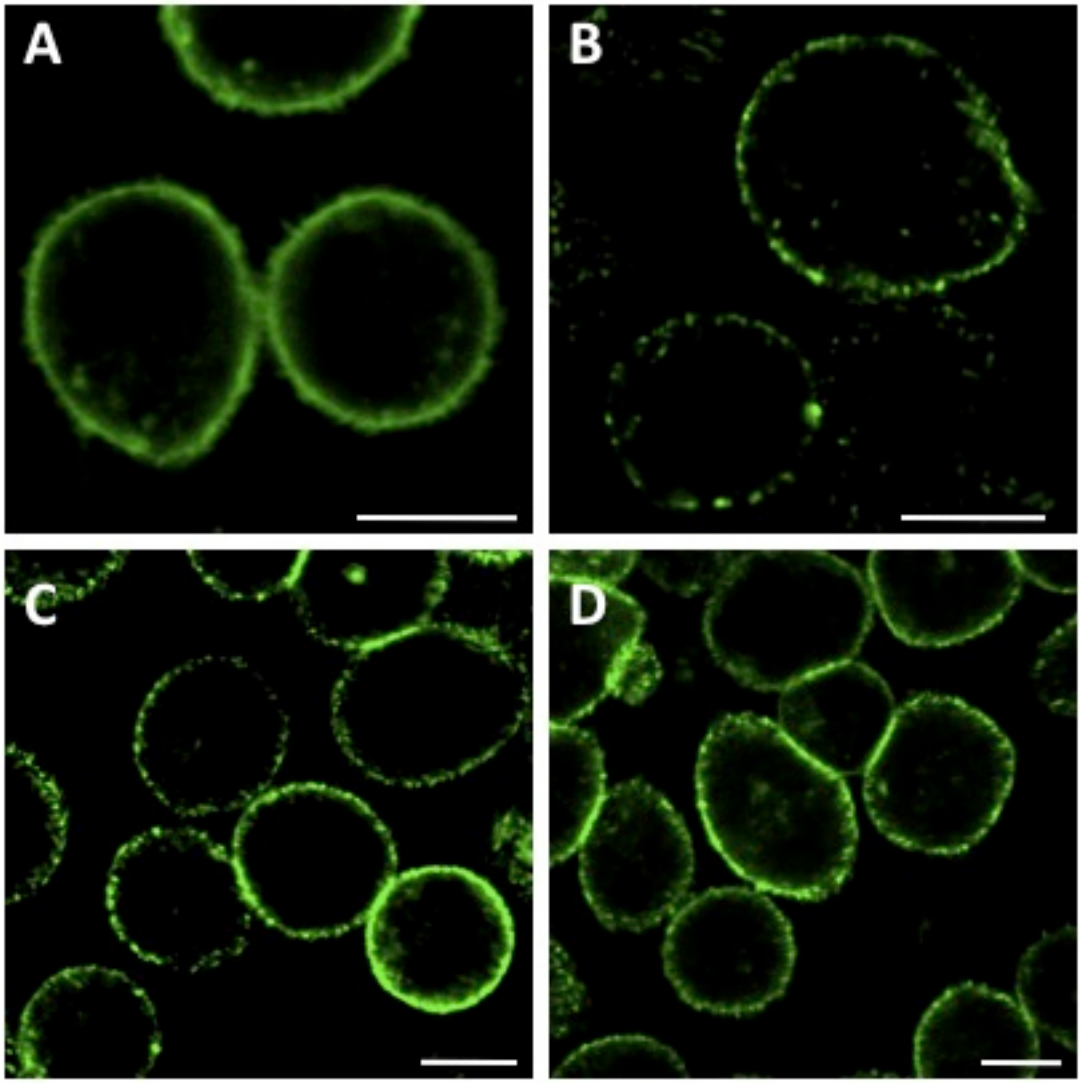

Figure B.1: Receptor crosslinking with trivalent Y-shaped DNA ligands induces the same micron-scale plasma membrane redistribution of IgE-FcεRI as DNP-BSA. A488-IgE bound to FcεRI on mast cells is visualized using confocal fluorescence microscopy before (A) and after (B-D) stimulation. IgE-FcεRI, which uniformly labels the plasma membrane in resting cells (A), exhibits a patchy fluorescence redistribution at the plasma membrane after 10 min stimulation at room temperature with DNP-BSA (B), Y16-DNP_3-DNA (C), or Y46-DNP_3-DNA (D). Scale bar is 10 μm.

We then used BSD-SEM to monitor the nano-scale distribution of 10 nm immuno-gold labeled IgE-FcεRI under the same experimental conditions described for Figure B.1. Figure B.2A-C illustrates representative reconstructed BSD images of IgE-FcεRI after 10 min stimulation with DNP-BSA (B.2A), Y16-DNP_3-DNA (B.2B), and Y46-DNP_3-DNA (B.2C). Gold particle distributions from many images were quantified using pair correlation functions (B.2D) that are well fit to single filtered exponentials. Fit parameters extracted from these curves reveal information about the size and density of receptor clusters (B.2E).

In resting cells, IgE-FcεRI has a random, uncorrelated distribution. After 10 min of stimulation with either DNP-BSA or Y16-DNP_3-DNA, crosslinked IgE-FcεRI clusters become correlated at long length-scales ($r<150$ nm, $\xi\approx50$ nm), compared to stimulation with Y46-DNP_3-DNA ($r<75$ nm, $\xi\approx10$ nm). DNP-BSA causes the highest degree of receptor clustering, indicated by higher $g(r)$ values in Figure B.2D and by the densely packed clusters visualized in B.2A. While DNP-BSA and Y16-DNP_3-DNA stimulated clusters of IgE-FcεRI are similar in size, Y16-DNP_3-DNA stimulated clusters contain ~40% less receptors per cluster (N_{cl}=10). IgE-FcεRI density within crosslinked receptor clusters is even more significantly reduced (~60%) after stimulation with Y46-DNP_3-DNA, as indicated in Figure B.2E.

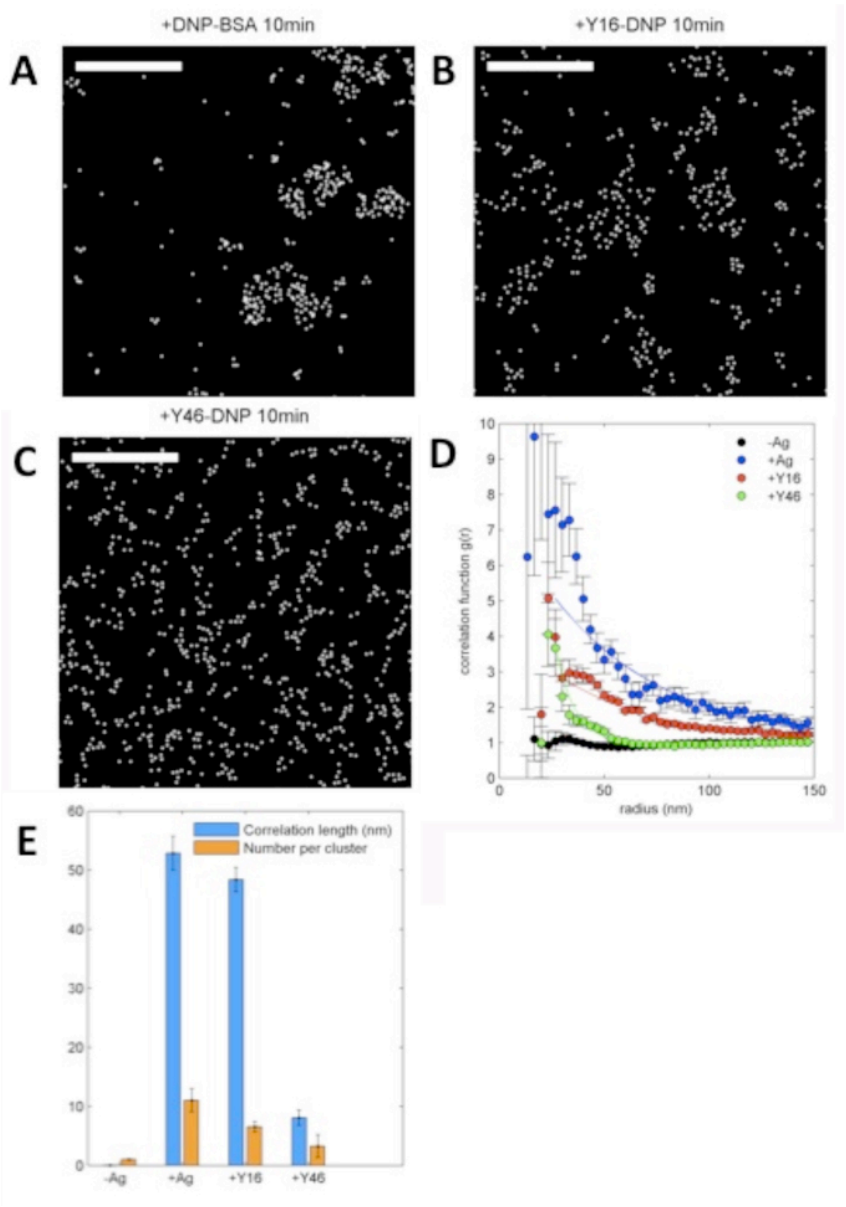

Figure B.2: IgE-FcεRI redistributes into clusters of various sizes and densities after 10 min of stimulation with Y-shaped DNA ligands at room temperature. A488-IgE-FcεRI was immuno-gold labeled (10 nm particles) in cells stimulated for 10 min at room temperature with (A) DNP-BSA, (B) Y16-DNP_3-DNA or (C) Y46-DNP_3-DNA, as visualized by the reconstructed BSD images. Scale bar is 500 nm. Gold particle distributions are quantified over many images (n>10) using pair-correlation functions (D) and extracted fit parameters (ξ, cluster size; N_{cl}, number of proteins per cluster) are shown in (E). IgE-FcεRI is randomly distributed in resting cells and redistributes into large clusters correlated at long length-scales (r<150 nm, ξ≈50 nm) after stimulation with DNP-BSA or Y16-DNP_3-DNA, compared to Y46-DNP_3-DNA (r<75 nm; ξ≈10 nm).

Due to the strong clustering response of IgE-FcεRI to Y16-DNP_3-DNA, we compared the distribution of 10 nm gold labeled IgE-FcεRI after 1 min stimulation at 37˚ C with Y16-DNP_3-DNA or DNP-BSA. Representative BSD images are shown in Figure B.3A-B. Gold particles were quantified over many images using pair correlation functions (B.3C). After 1 min of stimulation with DNP-BSA, crosslinked IgE-FcεRI clusters redistribute into large domains (r<200 nm), while clusters stimulated by Y16-DNP_3-DNA are correlated at shorter length-scales (r<100 nm). Additionally, Y16-DNP_3-DNA stimulated clusters are ~70% reduced in size (ξ≈25 nm) and ~80% reduced in the number of receptors per clusters (N_{cl}=5), compared with DNP-BSA stimulation (Figure B.3D).

We also visualized distributions of 10 nm gold labeled IgE-FcεRI at longer stimulation times with Y16-DNP_3-BSA at 37˚ C and quantified gold particle distributions with pair correlation functions. Correlation curves for 1, 5, and 10 min stimulation with Y16-DNP_3-DNA are plotted together in Figure B.4A, and protein cluster sizes and densities are reported in Figure B.4B. In resting cells, IgE-FcεRI is unclustered. After 1 min stimulation, IgE-FcεRI redistributes into large domains (r<100 nm) that become larger (r<150 nm) after 10 min of stimulation. Between 1-5 min of Y16-DNP_3-DNA stimulation, IgE-FcεRI cluster size (ξ≈25 nm) and the number of proteins per cluster (N_{cl}≈5) remains relatively constant. After 10 min, clusters nearly double both in size and in the number of proteins per cluster (ξ≈50 nm; N_{cl}≈10).

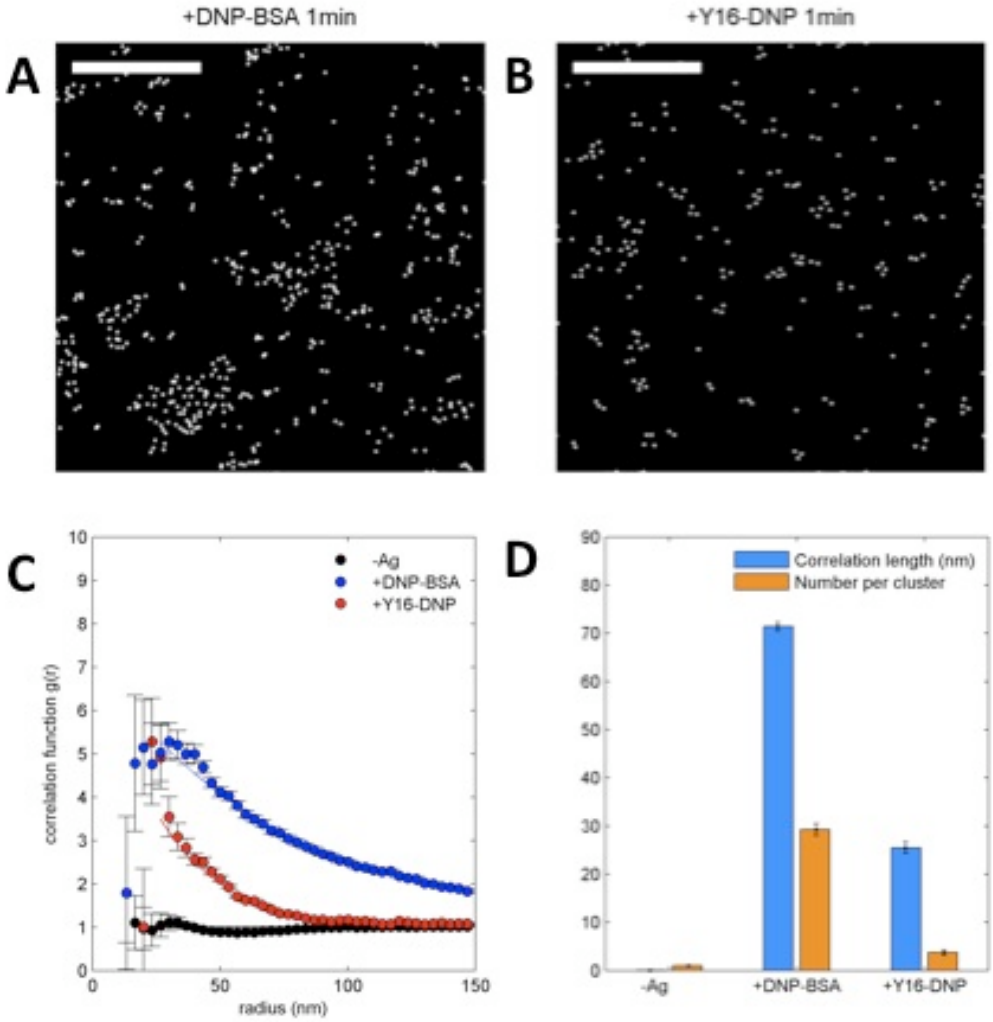

Figure B.3: Crosslinked IgE-FcεRI clusters are smaller after 1 min of stimulation with Y16-DNP$_3$-DNA compared to DNP-BSA. A488-IgE-FcεRI was immuno-gold labeled (10 nm particles), and protein distributions were visualized after 1 min of stimulation at 37˚ C with either (A) DNP-BSA or (B) Y16-DNP$_3$-DNA. Gold particles were quantified using pair correlation functions (C), and extracted fit parameters (ξ, cluster size; N_{cl}, number of proteins in clusters) from these curves are shown in (D). Stimulation with DNP-BSA causes IgE-FcεRI to redistribute from a random distribution (black curve) to large clusters that are correlated at long length-scales (blue curve, r<200 nm), compared to Y16-DNP$_3$-DNA stimulated clusters (red curve, r<100 nm). Compared to DNP-BSA, stimulation with Y16-DNP$_3$-DNA reduces cluster size (ξ) by ~65% and the number of proteins in clusters (N_{cl}) by ~80%. Scale bar is 500 nm.

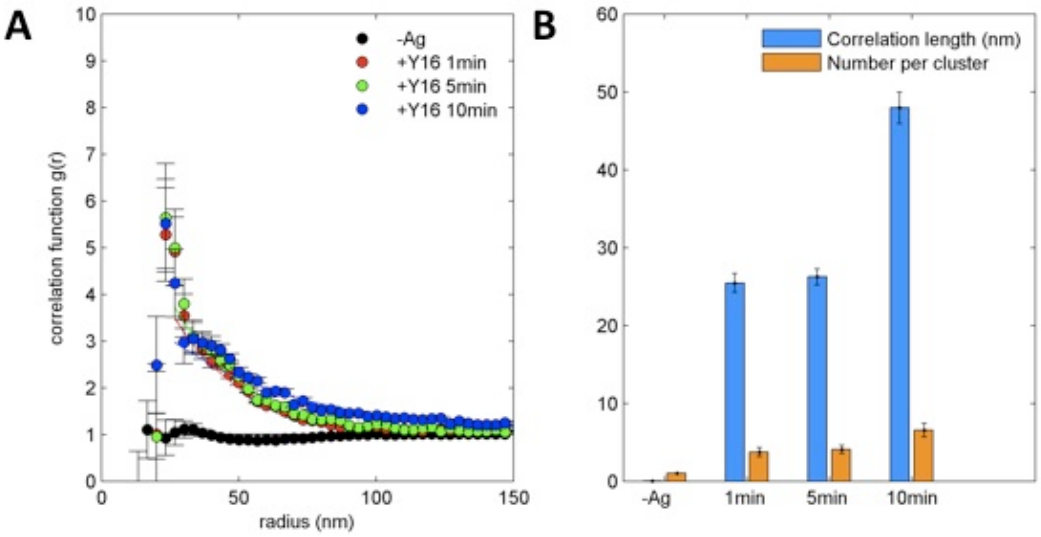

Figure B.4: IgE-FcεRI clusters increase in size during a 10 min stimulation time-course with Y16-DNP$_3$-DNA. Immuno-gold labeled IgE-FcεRI (10 nm) distributions were visualized before and after a 37° C stimulation time-course (1, 5, and 10 min) with Y16-DNP$_3$-DNA. A) Gold particle distributions over many images (N>10) were quantified using pair correlation functions that are well fit to single filtered exponentials. B) Fit parameters extracted from these curves describe cluster size (ξ) and the number of proteins per cluster (N_{cl}).

The ability to crosslink IgE-FcεRI with ligands that are structurally well defined provides unique information about the mechanisms that drive nano-scale protein reorganization during cell signaling. Despite fluorescence microscopy experiments that suggest DNP-BSA and Y-shaped DNP-DNA ligands crosslink receptors similarly on the micron-scale, our SEM findings reveal distinct structural differences in protein cluster size and the number of proteins per cluster at the nano-scale. Further, we demonstrate that receptor crosslinking is sensitive to DNP-DNA ligand length, and that receptor clusters are ~80% reduced in size and composition after stimulation with Y46-DNP_3-DNA, compared to Y16-DNP_3-DNA.

Given these and our previous findings, further studies are required to determine whether there is a ligand length-dependence to Lyn, Syk, and LAT clustering, as well as co-redistribution of IgE-FcεRI and Lyn. Our findings in Appendix A also suggest that the actin cytoskeleton may play a critical role in facilitating receptor crosslinking and the subsequent recruitment of signaling proteins to receptor clusters. Lastly, X-shaped DNA ligands functionalized with three DNP groups and one gold particle may provide a useful strategy to directly label crosslinked receptors without using primary or secondary gold-conjugated antibodies. Continued work using these tools will provide useful insight to better understand the molecular mechanisms drive protein organization during cell signaling events.

REFERENCES

1. Segal, D.M. and E. Hurwitz, *Binding of affinity cross-linked oligomers of IgG to cells bearing Fc receptors.* J Immunol, 1977. **118**(4): p. 1338-7.
2. Fewtrell, C. and H. Metzger, *Larger oligomers of IgE are more effective than dimers in stimulating rat basophilic leukemia cells.* J Immunol, 1980. **125**(2): p. 701-10.
3. Menon, A.K., D. Holowka, and B. Baird, *Small oligomers of immunoglobulin E (IgE) cause large-scale clustering of IgE receptors on the surface of rat basophilic leukemia cells.* J Cell Biol, 1984. **98**(2): p. 577-83.
4. Sil, D., et al., *Trivalent ligands with rigid DNA spacers reveal structural requirements for IgE receptor signaling in RBL mast cells.* ACS Chem Biol, 2007. **2**(10): p. 674-84.